Hochschule Karlsruhe – Technik und Wirtschaft
Fakultät für Maschinenbau und Mechatronik

Thermische Effizienzanalyse des ALPHA-g Kryostates Berechnung und Wärmesimulation

*** V E R T R A U L I C H ***

Bachelorarbeit (B.Eng.)
Nr. 21/035

von
Philipp Kuhn
geb. am 23.09.1998
in Freiburg im Breisgau
Matrikel-Nr.: 61514

Betreuer der Europäischen Organisation für Kernforschung CERN
Herr Dr. Pierre Grandemange

Betreuer der Hochschule Karlsruhe
Herr Prof. Dr.-Ing. Michael Arnemann

Genf, 01.05.2021 bis 31.08.2021

Declaration

I hereby certify on oath that I have prepared the report independently, that I have fully and accurately indicated all resources used and that I have individually identified everything that has been taken unchanged or with modification from the work of others.

Karlsruhe, 08.09.2021

Philipp Kuhn

Acknowledgements

I would like to express special thanks to my supervisor Dr. Pierre Guy Michel Grandemange from whom I had the opportunity to acquire a great deal of knowledge during the past 12 months at CERN. I would also like to thank the entire ALPHA collaboration. In particular, I am pleased to have been able to work with Dr. Chris Ørum Rasmussen, Prof. Niels Madsen and Prof. Jeffrey Scott Hangst. The expressed appreciation of my work gave me a lot of motivation for my future academic career.

Finally, I would also like to thank Prof. Michael Arnemann for his professional supervision, as well as the Deutschlandstipendium and the Valerius-Füner-Stiftung for their financial support with a scholarship during my studies in Karlsruhe.

Kurzfassung

Thermische Effizienzanalyse des ALPHA-g Kryostates - Berechnung und Wärmesimulation

Die vorliegende Bachelorthesis präsentiert eine thermische Analyse des ALPHA-g Kryostates am CERN zur Charakterisierung der thermischen Effizienz und Identifizierung möglicher Schwachstellen. Die Ergebnisse wurden erzielt durch analytische Berechnungen, C++ Algorithmen und thermisch-stationäre Simulationen, durchgeführt mit ANSYS workbench 2020 R2. Diese Modelle bestimmen Wärmeströme und Temperaturverteilungen in mechanischen Bauteilen und dem 2-Phasen-System aus flüssigem und gasförmigem Helium.

Im Allgemeinen dienen die Wärmeströme zu einer Abschätzung des Verbrauchs an flüssigem Helium (LHe) durch Verdampfung. Ein Vergleich zum Zielwert von $20\ \mathrm{L\,h^{-1}}$ wird herangezogen. Zusätzlich kann der Bedarf an gasförmigem Helium (GHe) für interne Kühlsysteme von Strahlungsschutzschildern und Hochstromleitungen evaluiert werden.

Das ALPHA-g Experiment untersucht die Baryonenasymmetrie von Antimaterie und Materie durch Messung der atomaren Antiwasserstoff-Masse. Der ALPHA-g Kryostat stellt dabei ein Bad aus LHe bei $4\ \mathrm{K}$ bereit um supraleitende Magneten sowie Elektroden zu kühlen. LHe tritt mit einer äußerst geringen Verdampfungsenthalpie von $\sim 21\ \mathrm{kJ\,kg^{-1}}$ bei Normdruck auf. Dies erfordert eine mehrschichtige Struktur des Kryostates zur Reduktion eingehender Wärmeströme. Die thermische Isolation des LHe ist dabei mithilfe einer umschließenden Vakuumkammer sichergestellt. Zusätzlich unterstützen interne Strahlungsschutzschirme und -folien sowie geeignete Bauteilstrukturen und -materialien die Isolation. Trotz dieser Maßnahmen, das LHe zu bewahren, ist der Kryostat diatherm; ein Teil verdampft, füllt den oberen Anlagenbereich mit GHe und kreiert ein 2-Phasen-System aus Flüssigkeit und Gas im Helium-Raum. Ein Großteil des GHe befindet sich in den rohrartigen Bauteilen *chimneys* und *service tubes* im oberen Bereich des Kryostates.

Eine Bewertung der thermischen Effizienz wird qualitativ im Kontext der eingehenden Wärmelast und des resultierenden Verbrauchs an LHe evaluiert. Die gesamte in den Helium-Raum eintretende Wärmelast beträgt $\sim 27\ \mathrm{W}$. Durch die komplexen konvektiven Zustände konnte nicht quantifiziert werden, welchen Anteil die Verdampfung an LHe und welchen die Erhöhung der GHe Enthalpie ausmacht. Ein Vergleich dieser theoretischen Werte mit Messungen während eines Kältetests erlaubt jedoch eine Abschätzung: Etwa $18\ \mathrm{W}$ verdampfen $\sim 25\ \mathrm{L\,h^{-1}}$ an LHe.

Simulationen zeigen eine thermische Schwachstelle der *chimneys* auf mit einer maßgeblichen Wärmeleitung von $\sim 8\ \mathrm{W}$. Die Faltenbälge sind dabei als wichtige Wärmeleitwiderstände identifiziert. Die Temperatur der äußeren *chimney* Wände beträgt größtenteils $> 50\ \mathrm{K}$. Mit einer angestrebten Temperatur der Strahlungsschutzschilde von $50\ \mathrm{K}$ wird die netto Strahlungsrichtung der Wärmestrahlung somit umgekehrt (im Vergleich zur vorgesehenen Richtung laut Konstruktion). Analytische Berechnungen zeigen, dass die gasgekühlten Stromleiter der Magnete einen Kühlgasmassenstrom von $\sim 0.655\ \mathrm{g\,s^{-1}}$ benötigen. Dies entspricht einem verdampfenden Volumenstrom von $\sim 18.9\ \mathrm{L\,h^{-1}}$ an LHe, welcher ohne zusätzliche Verdampfung bereitstehen kann. Im Vergleich dazu beträgt der benötigte Volumenstrom zur Kühlung der Strahlungsschutzschilde nur rund $\sim 1.3\ \mathrm{L\,h^{-1}}$ an LHe. Die angestrebte Temperatur dieser Schilde von $50\ \mathrm{K}$ kann als realisierbar evaluiert werden. Sie ist jedoch im Hinblick auf die thermische Effizienz nicht erforderlich. Demzufolge kann, bei Mangel an verfügbarem kalten GHe, eine Erhöhung bis zu $\leq 100\ \mathrm{K}$ empfohlen werden. Weitere Analysen zeigen eine geringfügige freie Konvektion im oberen Bereich der *chimneys*. In den *service tubes* könnte hingegen eine maßgebliche freie Konvektion auftreten. Es wird deshalb ein Einfügen von Trennwänden geraten.

Abstract

Thermal efficiency study of the ALPHA-g cryostat – an analysis and heat simulation

This thesis presents a thermal study of the ALPHA-g cryostat at CERN. The thermal efficiency is characterised and thermal week points are identified. The results were obtained through analytic calculations, C++ script of programs and thermal steady-state simulations performed with ANSYS workbench 2020 R2. These models estimate heat flows and temperature distributions in components and the 2-phase systems of liquid and gaseous helium.

In general, the heat loads are used to estimate the liquid helium (LHe) consumption by vaporisation. It is compared to a target consumption of $20\ \mathrm{L\,h^{-1}}$. Further, the gaseous helium (GHe) demand for internal cooling systems of radiation shields and vapour cooled leads (VCL) is determined.

The ALPHA-g experiment studies the Baryon asymmetry of antimatter and matter by measuring the antihydrogen atomic mass. The ALPHA-g cryostat is only one subsystem of the experiment; its main purpose is to provide a cold LHe bath at $4\ \mathrm{K}$ to cool superconducting magnets and electrodes, in addition to cryopump an ultra-high vacuum chamber. Since LHe is present at cryogenic temperatures with a relatively low enthalpy of vaporisation ($\sim 21\ \mathrm{kJ\,kg^{-1}}$ at norm pressure), the cryostat contains a complex multi-layered structure to lower the incoming heat load. The thermal insulation of the LHe is achieved with an enclosing vacuum chamber with internal radiation shields and foils, as well as suitable component structures and material selection. Despite these measures to preserve the LHe, the apparatus is diathermic; some of the LHe evaporates and fills the upper section of the vessel with GHe. This creates a 2-phase system of liquid and gas in the helium-space. Most of the GHe is located in the tubular components ‘chimneys’ and ‘service tubes’ in the upper section of the cryostat.

An evaluation of the thermal efficiency is carried out qualitatively in the context of ingoing heat loads and a resulting estimated LHe consumption. The total heat load entering helium-space is approximately $27\ \mathrm{W}$. Due to the complex convective conditions, it could not be quantified how much of this heat load evaporates LHe and to what extend it increases the GHe enthalpy. However, a comparison of the theoretical values with measurements during a cold test allows an estimation. Approximately $18\ \mathrm{W}$ evaporate $\sim 25\ \mathrm{L\,h^{-1}}$ of LHe.

Simulations showed a thermal weak point at the chimneys with relevant heat conduction of $\sim 8\ \mathrm{W}$. The flexible bellows are identified as important thermal resistors. The temperature at the outer chimney wall is $> 50\ \mathrm{K}$ for the most part. With a target radiation shield temperature of $50\ \mathrm{K}$, the net direction of heat radiation is reversed as compared to the intended direction by design. The VCL influence this temperature the most. Analytical calculations determine that the VCL require a cooling gas mass flow of $\sim 0.655\ \mathrm{g\,s^{-1}}$. This corresponds to an evaporating LHe volume flow of $\sim 18.9\ \mathrm{L\,h^{-1}}$. It can be provided without additional boil-off. In comparison, the required evaporating LHe volume flow to cool the radiation shields is only $\sim 1.3\ \mathrm{L\,h^{-1}}$. It corresponds to a net heat load onto the radiation shields of $\sim 11\ \mathrm{W}$. The target radiation shield temperature of $50\ \mathrm{K}$ can be evaluated as feasible but not necessary regarding the thermal efficiency of the cryostat. An increase up to $\leq 100\ \mathrm{K}$ is therefore recommended in case of cooling gas shortage. All determined heat flows take static gas inside the chimneys and service tubes into account. Analysis of this assumption showed little free convection in the upper chimney sections. In the service tubes, free convection might be relevant. It could be advised adding baffles here.

Nomenclature

Latin formula symbols

a_i	-	Coefficient for MLI temperature
A	$\mathrm{m^2}$	Surface area
b_i	-	Coefficient for MLI temperature
c_p	$\mathrm{J\ kg^{-1}\ K^{-1}}$	Heat capacity at constant pressure
c_v	$\mathrm{J\ kg^{-1}\ K^{-1}}$	Heat capacity at constant volume
$\mathrm{C_c}$	$8.95 \cdot 10^{-5}\ \mathrm{mW\ m^{-2}\ K^{-2}}$	Constant for MLI conduction
C_{ij}	-	Combined radiation exchange coefficient
d	m	Diameter
D	m	Material thickness
e	-	Function for emissive coefficient dependent on temperature
E	J	Energy
g_c	$1\ \mathrm{kg\ m\ N^{-1}\ s^{-2}}$	Conversion factor in Newton’s Second Law of Motion
G	m	Geometry factor of heat conduction
h	m	Height
Δh^v	$\mathrm{J\ kg^{-1}}$	Specific enthalpy of vaporisation
$\Delta h^\mathrm{g}_{4\,\mathrm{K}\rightarrow 300\mathrm{K}}$	$\mathrm{J\ kg^{-1}}$	Specific enthalpy difference of gas from 4 K to 300 K
i	-	Control variable
I	A	Current
j	-	Control variable
k	$\mathrm{W\ m^{-1}\ K^{-1}}$	Thermal conductivity
k	-	Iteration step
k'	$\mathrm{W\ m^{-1}\ K^{-1}}$	Pseudo-thermal conductivity
l	m	Length
l_gas	m	Mean free path
L	m	Length
m	kg	Mass
M	$\mathrm{kg\ mol^{-1}}$	Molar mass
n	-	Number of MLI layers
N	$\mathrm{cm^{-1}}$	MLI layer density
p	Pa	Pressure
P	W	Power
P	Pa	Mechanical pressure
$\dot{q}$	$\mathrm{W\ m^{-2}}$	Heat flux
$\dot{Q}$	W	Heat flow
r	m	Radius

r'	m	Reduced radius
R	$\mathrm{J\ K^{-1}\ kg^{-1}}$	Individual gas constant
R_k	$\mathrm{K\ W^{-1}}$	Thermal resistivity
R_U	$8.3145\ \mathrm{J\ K^{-1}\ mol^{-1}}$	Universal gas constant
s	m	Thickness
s_in	$\mathrm{J\ kg^{-1}\ K^{-1}}$	Specific ingoing entropy
s_out	$\mathrm{J\ kg^{-1}\ K^{-1}}$	Specific outgoing entropy
S	$\mathrm{J\ K^{-1}}$	Entropy
T	K	Temperature
U	J	Internal Energy
U	V	Voltage
v	$\mathrm{m\ s^{-1}}$	Velocity
V	$\mathrm{m^3}$	Volume
W	J	Work
x	m	Length variable in dimension 1
y	m	Length variable in dimension 2
z	m	Length variable in dimension 3

Greek formula symbols

α	-	Absorptivity
α	$\mathrm{W\ m^{-2}\ K^{-1}}$	Heat transfer coefficient (also called film coefficient)
β	$\mathrm{K^{-1}}$	Isobaric coefficient of thermal expansion
γ	-	Specific heat ratio
δ	m	Representative physical length
ε	-	Emissivity
Θ	$\mathrm{W\ m^{-1}}$	Thermal conductivity integral
κ	-	MLI conductance factor
κ	$\mathrm{m^2\ s^{-1}}$	Thermal diffusivity
μ	Pa s	Dynamic viscosity
ν	$\mathrm{m^2\ s^{-1}}$	Kinematic viscosity
ξ	-	Ratio of the hot temperature to the cold one for TAOs
ρ	$\mathrm{kg\ m^{-3}}$	Density
σ	$8.6704 \cdot 10^{-8}\ \mathrm{W\ m^{-2}\ K^{-4}}$	Stefan-Boltzmann constant
τ	-	Transmissivity
φ	-	Ratio of warm tube length to cold tube length for TAOs
χ	-	Exponent of the temperature dependence of the total MLI heat transfer
ψ	-	Accommodation coefficient

$\dot{\omega}$	$\mathrm{W\,m^{-3}}$	Heat source density

Special symbols

d	Total differential
∂	Partial differential operator
Δ	Difference
$f(T)$	Function of T
$\approx$	Approximately
$\sim$	Approximately
$\propto$	Proportional
$\dot{m}$	Flow of m
(1.1)	Equation number

Special indexes

arithm	Arithmetic
chim	Chimney
cond	Conduction
crit	Critical
cryo-s	Cryo-support
CV	Control volume
Dew	Dewar
down	Downstream
g	Gaseous
gas	Gas
in	Ingoing
irr	Irreversible
iter	Iteration
kin	Kinetic
line	Gas line
liq	Liquid
m	Mean value
max	Maximum value
min	Minimum value
out	Outgoing
pot	Potential
rad	Radiation
rec	Recovery

serv	Service tube
tot	Total
up	Upstream

Dimensionless quantities

COP	Coefficient of performance
Kn	Knudsen number
Nu	Nusselt number
Ra	Rayleigh number
Re	Reynolds number
RRR	Residual-resistance ratio

Abbreviations

ALPHA	Antihydrogen Laser Physics Apparatus
AMI	American Magnetics Inc.
AT	Atom trap
Cryo	Cryogenic
CV	Control volume
GHe	Gaseous helium
HKA	Hochschule Karlsruhe University of Applied Sciences
HTS	High-temperature superconductor
LHe	Liquid helium
MLI	Multi-layer insulation
MSE	Microsoft Excel
OFHC	Oxygen-free high thermal conductivity
SM	Superconducting magnet
TAO	Thermo acoustic oscillations
VCL/VCCL	Vapour cooled (current) lead

List of contents

1 The ALPHA-g experiment – an introduction

The Baryon asymmetry of antimatter and matter is a major outstanding problem in the standard model. Experimental confirmation of the gravitational mass of antimatter is crucial for several important questions in fundamental physics [1]. The ALPHA (Antihydrogen Laser PHysics Apparatus) collaboration located at CERN, the European Organization for Nuclear Research in Geneva, aims to precisely measure the antihydrogen mass by confining these antimatter atoms in a magnetic trap in the ALPHA-g experiment [1]. The ALPHA-g cryostat is a central system for achieving the desired experimental data.

This thesis will include an analysis of heat flows within the cryostat and across its system boundary with the objectives of examining the thermal efficiency and identify possible thermal weak points. Initially, individual thermal subsystems are considered independently of each other in order to estimate the influence of the different heat flows. This includes free-molecular heat transfer in vacuum, heat radiation and conduction through multi-layer insulation foils (MLI), heat conduction in solid components as well as heat conduction and convection in helium. Subsequently, the influence of each subsystem is compared and evaluated. This leads to a more detailed thermal simulation of a possible thermal weak point in components in the upper section of the cryostat; the chimneys. These enclose high-temperature superconductors (HTS), which supply high electric current to the atom trap (AT). The simulation was focused on energy dissipation into static and flowing GHe due to internal resistive heating in the HTS system. Another focus of the thermal study in the thesis is the iterative determination of heat radiation through MLI with the help of C++ script of programs.

It must be mentioned that the candidate of the thesis had already been working on site for ALPHA at CERN since September 2020, before starting the bachelor thesis. In the winter semester 2020, the module *Projektarbeit* was enrolled in the same project at the Hochschule Karlsruhe University of Applied Sciences (HKA). It covered a technical description of the assembly process, the problems encountered in the sealing technology and the cold tests carried out during this period. Explicit reference is made to this technical description [2], which was conducted by Prof. Dr.-Ing. Martin Jäckle at the HKA as the examiner. The background of the experiment, such as the structure of the beamline or the creation of antihydrogen will therefore not be discussed further in this thesis.

1.1 Definition of thermal efficiency

The ALPHA-g cryostat is an evaporator, not a classic refrigeration system. The remaining three key components of the classic refrigeration cycle (compressor, condenser and expansion unit) are not part of the system. In this case, CERN has a separate department for the supply of liquid helium (LHe), and the recovery and liquefaction of gaseous helium (GHe). In this thesis, the thermal efficiency is therefore not evaluated with a quantitative parameter such as the coefficient of performance COP, but in the context of the ingoing heat loads and the resulting estimated consumption of LHe.

1.2 The ALPHA-g cryostat and its history

The ALPHA-g cryostat is about 5 m tall, 2 m wide and 2 m long. The multi-layered structure of the apparatus will be discussed in chapter 3.1. A more detailed description can also be found in the before mentioned *Projektarbeit* from February 2021 [2].

The main design of the ALPHA-g cryostat was performed at the Rutherford Appleton Laboratory (RAL) in Oxfordshire, UK. Its assembly was completed in 2018. Unfortunately, the collaboration faced various thermal and sealing difficulties and operated the cryostat without radiation shields, resulting in unacceptably high thermal loads. During CERN's "long shutdown two" the antiproton beam, that ALPHA relies on for experimental results, was not operating. The collaboration modified and improved the ALPHA-g cryostat during this time. With launch of the antiproton beam from the new Extra Low Energy Antiproton ring (ELENA) at the end of August 2021, the collaboration is currently in the final assembly stage and aims to run the full apparatus in the coming months. Before incorporating the main superconducting magnet's structure, a partial assembly of ALPHA-g cryostat was performed in order to check its performance. This led to five cold tests in December 2020 and January, April, July and August 2021.

1.3 Work methods and guideline of the thesis

Many of the results are obtained through simple models that yield analytic results. The geometric data used was taken from CAD models and technical drawings. Material properties were derived from NIST data. Further results were achieved using C++ script of programs as well as thermal simulations performed by ANSYS workbench.

The reader will first be directed to fundamentals of heat transfer with a focus on non-trivial heat transfer through multi-layer insulation (MLI) and will then be given an overview of the thermodynamic conditions of the cryostat. Following this, the results will be presented and analysed.

2 Theoretical background

The following chapter will discuss general theories about conductive, radiative and free-molecular heat transfer which are relevant for the thermal efficiency study of the ALPHA-g cryostat. Due to the non-trivial heat conduction in vacuum and through multilayer insulation foils (MLI), they are discussed in greater details in chapter 2.2 and 2.3.

2.1 Heat conduction in solids

The Fourier's law describes the vectorial conductive heat flux $\vec{q}$ with thermal conductivity k and temperature T for Cartesian coordinates as follows:

$$\vec{q} = -k \cdot \nabla T = -k \cdot \operatorname{grad} T = -k \cdot \left(\frac{\partial T}{\partial x}, \frac{\partial T}{\partial y}, \frac{\partial T}{\partial z}\right) \tag{2.1}$$

A power balance of an infinitesimal volume unit leads to the Fourier differential equation with density ρ, heat capacity at constant volume c_v and heat source $\dot{\omega}$ [3, p. 3.1]:

$$\rho\, c_\mathrm{v}\, \frac{\partial T}{\partial t} = \frac{\partial}{\partial x}\left(k \frac{\partial T}{\partial x}\right) + \frac{\partial}{\partial y}\left(k \frac{\partial T}{\partial y}\right) + \frac{\partial}{\partial z}\left(k \frac{\partial T}{\partial z}\right) + \dot{\omega} \tag{2.2}$$

Considering one-dimensional heat conduction along the direction x through a flat plate of the surface A from position 1 to 2 in steady state with $\dot{\omega} = 0$, the differential equation solves to

$$\dot{q}_{12} = \frac{\dot{Q}_{12}}{A} = \frac{k\,(T_1 - T_2)}{x}. \tag{2.3}$$

In practical applications, systems often occur with sequential sections of multiple materials or geometries. Here, an approach similar to electronics can be used, where ΔT acts as potential (cf. voltage), R_k as thermal resistivity (cf. electric resistance) and $\dot{Q}_{12}$ as resulting heat flow (cf. current):

$$\dot{Q}_{12} = \frac{\Delta T_{12}}{R_k} \tag{2.4}$$

The segments can be linked in series or parallel, which must be taken into account with regard to R_k:

$$R_{\mathrm{k\,serial}} = \sum_{i=1}^{n} R_{k\,i} = \sum_{i=1}^{n} \frac{l_i}{k_i \cdot A_i} \tag{2.5}$$

$$\frac{1}{R_{\mathrm{k\,parallel}}} = \sum_{i=1}^{n} \frac{1}{R_{k\,i}} = \sum_{i=1}^{n} \frac{k_i \cdot A_i}{l_i} \tag{2.6}$$

However, this calculation method is only valid when assuming a constant thermal conductivity; $k = \text{const}$. This depends on the material properties and the temperature range. In cryogenic applications with LHe, temperature ranges of about 300 K can occur. Furthermore, for some materials such as stainless steel, k decreases more than an order of magnitude when going from 100 K to 4 K [4, p. 7]. An optimised approach needs to be adopted by [4, p. 6]

$$\dot{Q}_{12} = -G\,(\Theta_1 - \Theta_2), \tag{2.7}$$

with a geometry factor G according to [4, p. 6]

$$G = \frac{1}{\int_{x_1}^{x_2} \frac{dx}{A(x)}} \tag{2.8}$$

and the thermal conductivity integral following [4, p. 7]

$$\Theta_i = \int_0^{T_i} k(T)\mathrm{d}T. \tag{2.9}$$

2.2 Heat conduction in gases

MLI are heat radiation foils with low emissive coefficients in the range $\lesssim 0.05$. They are used to lower the radiative heat flow between two surfaces at large temperature differences. More detailed explanations follow in chapter 2.3 and 3.9. Figure 2.1 displays the total heat flux over pressure through MLI. It is given by the sum of the radiative and conductive heat flow $\dot{q}_{\mathrm{MLI}}$ and the gas conduction $\dot{q}_{\mathrm{gas}}$:

$$\dot{q}_{\mathrm{tot}} = \dot{q}_{\mathrm{MLI}} + \dot{q}_{\mathrm{gas}}. \tag{2.10}$$

For high pressures, the thermal gas conductivity is independent of the pressure and for low pressures, $\dot{q}_{\mathrm{gas}}$ becomes negligible. As a result, the radiative and conductive heat flows dominate for pressures $\lesssim 10^{-3}$ mbar and $\dot{q}_{\mathrm{total}}$ reaches a stagnant level regarding the pressure variance.

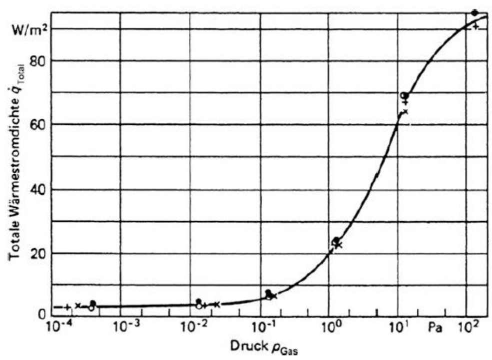

Figure 2.1. Total heat flux $\dot{q}_{\mathrm{tot}}$ through MLI as function of pressure [5, p. 1290].

The method to calculate heat transfer in gases depends on the Knudsen number [6, p. 35]

$$Kn = \frac{l_{\mathrm{gas}}}{\delta}, \tag{2.11}$$

where l_{gas} is the mean free path between the molecules or atoms and δ is the representative physical length. In a gas chamber with the enclosure volume V and the surface area A, the representative physical length may be determined according to [7, p. 253]

$$\delta = \frac{4\,V}{A}. \tag{2.12}$$

This physical quantity indicates a gap length in the system in which the gas conducts heat. In between two wall or foil surfaces with a small distance in relation to their length and width, δ would be two times the surface separation.

One has to separate continuum-type conduction ($Kn \ll 1$ resp. $Kn < 0.01$), free-molecular conduction ($Kn \gg 1$ resp. $Kn > 0.3$) and mixed conduction ($0.01 < Kn < 0.3$) [7, p. 244]. In the first type, high-energy molecules only travel distances at the order of 70 nm for air at ambient temperature and pressure before striking a low-energy molecule and transfer some of their energy to it [7, p. 248]. This distance is defined as the mean free path l_{gas} of a molecule according to Maxwell [8, p. 32]. In the free-molecular state, molecules travel much longer distances before they collide: The molecule density is so low, the "high-energy molecule travels across the space between the containing surfaces, strikes the lower-temperature surface, and transfers energy directly to the surface." [7, p. 249]. This fundamental difference in energy transfer leads to two different methods of calculation: continuum-type and free-molecular-type.

2.2.1 Continuum-type conduction

For continuum-type conduction, the temperature distribution inside the gas along the axis of the heat transfer is linear. The heat conduction through a non-moving gas is defined by Equation (2.1). The heat conductivity at atmospheric pressure k_0 in W m^{-1} K^{-1} can be found in tables from experimental data or calculated according to Kennard [9, p. 164]

$$k_0 = \frac{c_{\mathrm{v}}\,\rho_{\mathrm{gas}}\,l_{\mathrm{gas}}\,v}{3}. \tag{2.13}$$

In Equation (2.13) c_{v} denotes the specific heat capacity at constant volume, ρ_{gas} the gas density, l_{gas} the mean free path and v the velocity of the molecules or atoms. It is given by the isotropic Maxwell-Boltzmann distribution [10, p. 389] with $R = R_{\mathrm{U}} \cdot M^{-1}$ [7, p. 244]:

$$v = \sqrt{\frac{8\,k_{\mathrm{B}}\,T}{\pi\,m}} = \sqrt{\frac{8\,R\,T}{\pi}} \tag{2.14}$$

The mean free path l_{gas} in Equation (2.13), first described by Maxwell [8, p. 32] and clarified by Chapman and Cowling [7, p. 244]

$$l_{\text{gas}} = \frac{\mu}{p}\sqrt{\frac{\pi\, R_{\text{u}}\, T}{2\, g_{\text{c}}\, M}} = \frac{\mu}{p}\sqrt{\frac{\pi\, R\, T}{2\, g_{\text{c}}}}, \tag{2.15}$$

reveals that the heat conductivity k_0 is independent of the gas density and pressure at constant temperature for ideal gases. In equation (2.15) μ denotes the viscosity and g_c is a conversion factor in Newton's second law of motion of 1 kg m N^{-1} s^{-2}. For gases at high temperatures and for gases with small and light molecules, k_0 becomes large. The independence of k_0 of pressure stops for gases at low pressures in the range of medium vacuum [5, p. 1273]. For nitrogen at 1 mbar Kn is ~ 0.07, which does not indicate a free-molecular state. Nevertheless, the gas already has a lower thermal conductivity. This is the transition area to a pressure dependence.

2.2.2 Free-molecular heat transfer

Free molecular states ($Kn \gg 1$) usually occur at fine or medium vacuum (10^{-3} mbar to 1 mbar), high vacuum (10^{-7} mbar to 10^{-3} mbar) and ultra-high vacuum (UHV) (10^{-12} mbar to 10^{-8} mbar) [11, pp. 875-876]. The kinetic gas theory uses a simplified model in which the molecules of an ideal gas are rigid spheres that collide elastically. For $Kn \gg 1$ the molecules rarely collide and Equation (2.1) no longer applies. In contrast, the free-molecular heat transfer may be determined by [7, p. 251]

$$\dot{q} = \frac{K}{\frac{1}{\psi_1} + \frac{A_1}{A_2}\left(\frac{1}{\psi_2} - 1\right)}\, p\,(T_2 - T_1) \tag{2.16}$$

with the property-dependent parameter

$$K = \frac{\gamma + 1}{\gamma - 1}\sqrt{\frac{g_{\text{c}}\, R_{\text{u}}}{8\,\pi\, T\, M}}. \tag{2.17}$$

In equation (2.17), γ denotes the specific heat ratio c_p/c_v which is 1.40 for air at 300 K [12, p. 367].

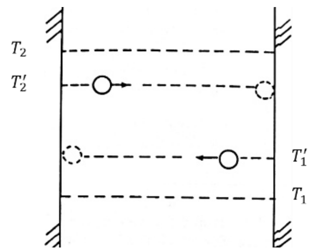

Figure 2.2. Free molecular conduction between a hot surface and a cold surface [7, p. 249].

As shown in Figure 2.2, the high-energy molecules collide directly with the cold wall surface, but they remain too shortly on the surface to reach thermal equilibrium [7, p. 250]. The accommodation coefficient ψ_1 in Equation (2.16) denotes how much energy the high-energy molecules can transfer to the cold solid compared to the energy they would transfer in an equilibrium state (ψ_2 referred to warm surface). Alternatively: The "actual energy transfer divided by the maximum possible energy transfer." [7, p. 250]. As a result, the molecules leave the cold wall surface with an energy corresponding to a temperature bigger than the surface temperature $T_1' > T_1$:

$$\psi_1 = \frac{T_2' - T_1'}{T_2' - T_1} \tag{2.18}$$

Values for ψ depend on the individual gas and its temperature. It reminds of the emissive coefficient for heat radiation, which is also a function of temperature.

Table 2.1. Accommodation coefficients of relevant gases at different temperatures [7, p. 250].

Temperature		Gas			
K	°R	Helium	Hydrogen	Neon	Air
300	540	0.29	0.29	0.66	0.8–0.9
78	140	0.42	0.53	0.83	1.00
20	36	0.59	0.97	1.00	1.00

2.3 Heat transfer through multi-layer insulation foils

Multi-layer insulation foils reduce heat radiation. If considering only heat radiation, the greater the number of layers in between two heat-exchanging surfaces, the lower the transferred heat flow. However, in practical terms, too many layers also increase the solid heat conduction through a dense MLI blanket. The full heat flow transferred by MLI from Equation (2.10)

$$\dot{Q}_{\mathrm{MLI}} = \dot{Q}_{\mathrm{MLI\,rad}} + \dot{Q}_{\mathrm{MLI\,cond}} \tag{2.19}$$

is given as the sum of the radiative and conductive heat flow [13]. As the radiative heat flow is proportional to the fourth power of the temperature, see equation (2.20), it drops to a minimum in any case between two cold surfaces. In contrast, conductive heat flow is linearly proportional to the temperature difference. For cryogenic applications of MLI, this second element of heat flow through the MLI is not negligible anymore. As a result, there is an optimum number of layers per gap length in the apparatus [5, p. 1276].

2.3.1 Heat radiation through multi-layer insulation foils

Heat radiation is non-linear to the temperature difference as it is the case for heat conduction. Therefore, radiation is less important for low temperatures and can even be negligible for cryogenic temperatures in some cases. The exchanged heat radiation $\dot{Q}_{12}$ resp. radiative heat flux $\dot{q}_{12}$ from a surface with index '1' to a surface with index '2' is given with [14, pp. 33-34]

$$\dot{Q}_{12} = A_1\, C_{12}\, (T_1^4 - T_2^4) = A_1\, \dot{q}_{12}\ . \tag{2.20}$$

The combined radiation exchange coefficient [14, p. 33]

$$C_{12} = \frac{\sigma}{\frac{1}{\varepsilon_1} + \left(\frac{1}{\varepsilon_2} - 1\right)\frac{A_1}{A_2}} \tag{2.21}$$

describes the radiative exchange of the surface 1 to the surface 2 with each their own emissive coefficients ε_1 resp. ε_2 and their surface areas A_1 resp. A_2. The Stefan-Boltzmann constant σ is given with $5.6704 \cdot 10^{-8}$ W m^{-2} K^{-4} [5, p. 1288].

Radiation that hits a surface of a body can be reflected, absorbed or transmitted. Due to the conservation of energy

$$\dot{Q} = \dot{Q}_\varrho + \dot{Q}_\alpha + \dot{Q}_\tau. \tag{2.22}$$

The sum of reflectivity ϱ, absorptivity α and transmissivity τ equals 1:

$$1 = \frac{\dot{Q}_\varrho}{\dot{Q}} + \frac{\dot{Q}_\alpha}{\dot{Q}} + \frac{\dot{Q}_\tau}{\dot{Q}} = \varrho + \alpha + \tau. \tag{2.23}$$

For the analysis discussed in this thesis, the assumption of a Lambert radiator, which is an ideal diffuse radiator, is legitimate. Therefore, the emissivity is independent of direction. Furthermore, the radiator can be seen as a grey radiator with an emissivity independent of the emitted wavelength. As a result of these two assumptions, emissivity equals the absorptivity according to the Kirchhoff law [15, p. 1190]

$$\varepsilon(T) = \alpha(T)\ . \tag{2.24}$$

To reduce the heat radiation of two surfaces, there are two basic design options: On the one hand, layers in between the two surfaces can be added. On the other hand, the emissive coefficient can be lowered. In cryogenic systems, both methods are combined by using superinsulation, also called multi-layer insulation foils. These foils are added between the radiation exchanging surfaces. For $\varepsilon_\mathrm{a} = \varepsilon_\mathrm{b} = \varepsilon_\mathrm{MLI}$ and $A_\mathrm{a} = A_\mathrm{b}$, the MLI reduces the heat radiation by the factor of $(n+1)^{-1}$ with n as number of layers, as shown in [3, p. 6.3]

$$\dot{q}_{12,\mathrm{MLI}} = \frac{\sigma\,(T_1^4 - T_2^4)}{\left(\frac{2}{\varepsilon} - 1\right)(1+n)}. \tag{2.25}$$

Or expressed more detailed for $\varepsilon_a \neq \varepsilon_b \neq \varepsilon_\mathrm{MLI}$ with [15, p. 1195]

$$\dot{q}_{12,\mathrm{MLI}} = \frac{\sigma\,(T_1^4 - T_2^4)}{\frac{1}{\varepsilon_1} + \frac{1}{\varepsilon_2} - 1 + n\left(\frac{2}{\varepsilon_\mathrm{MLI}} - 1\right)}. \tag{2.26}$$

2.3.1.1 Emissive coefficient as a function of temperature

One has to take into account the important assumption in Equation (2.25) and (2.26), that the analytical solutions use a temperature independent emissive coefficient of the MLI. In reality, the emissive coefficient [15, p. 1187]

$$\varepsilon = f(T) \tag{2.27}$$

is a function of temperature. Due to the unknown foil temperatures, this can be respected in an iteration, which will be discussed in chapter 4.2.2.

To determine an accurate radiative heat flux through the MLI, a detailed knowledge of the emissive coefficient is mandatory. However, this accuracy is difficult to achieve. First, the temperature distribution along the layers must be known. Second, the actual emissive coefficient depends on several tough-diagnosable parameters, such as the surface state, the treatment during the assembly regarding crumpled foils, the degree of pollution or the pore amount and size. In addition, data from literature should be interpreted with caution. Measurements from different papers vary in certain temperature ranges, such as [13], [16] or [17]. Most certainly, this is caused by the mentioned tough-diagnosable parameters. A selection of experimental results to show the influence of degradation on quality and lifetime of MLI by Lehmann can be found in [18].

A common material used as MLI are aluminized Mylar or polyester foils. Their properties are different to solid aluminium. In general, "the emissivity […] of the solid aluminium […] [does] not automatically apply to the properties of thin Al films, in particular especially for aluminised thin polymer films." [5, p. 1346]. A key reason is that the mean free path of the electrons in the aluminium (Al) coating is of a similar order as the coating thickness. At room temperature, the mean free path is about 40 nm. Coating thicknesses below 40 nm can transmit infrared radiation [5, p. 1347].

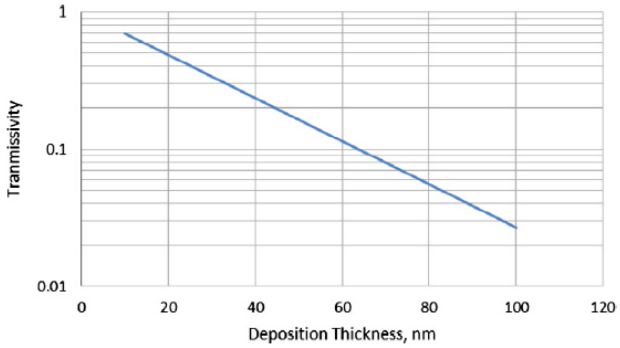

Figure 2.3. Influence of deposition thickness on transmissivity at 290 µm wavelength (peak wavelength at 10 K) for a surface with an electrical resistivity of 5 µΩ cm [19].

Figure 2.3 shows the transmissivity τ as function of deposition thickness. Thin coatings can transmit a significant amount of the radiation and fail their purpose of reflection according to Equation (2.23). Therefore, one must separate data about the emissivity from solid Al to aluminised polyester foils, as the one of Al-coated foils are always lower than the ones of solid metals [16].

A functional correlation between temperature and MLI emissivity was found by Lockheed and described by Ross [13] with

$$\varepsilon(T) = 6.8 \cdot 10^{-4}\, T^{0.67}. \tag{2.28}$$

Combining Equation (2.28) and (2.25) gives a relation of $\dot{q}_{12,\mathrm{MLI}} \propto T^{4.67}$. In contrast, more detailed information is given by experimental measurements from Musilova et. al [16] for

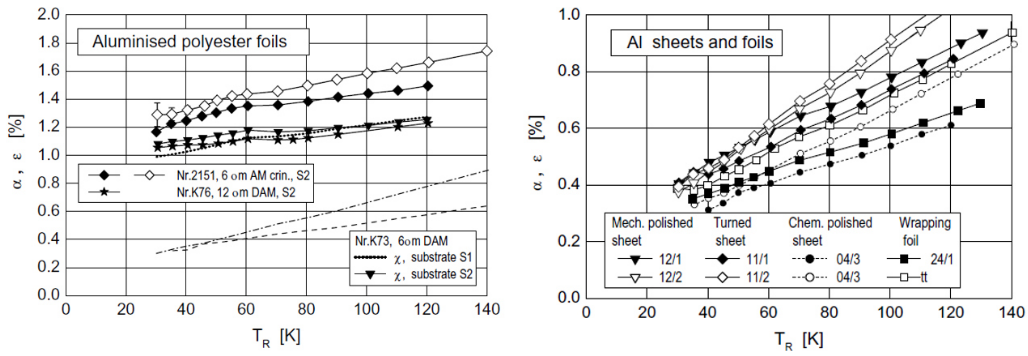

Figure 2.4. Total absorptivity (solid symbols) and emissivity (open symbols) as function of temperature from 30 K to 140 K. (a) Aluminised polyester foils (b) Al wrapping foil in comparison with mechanically and chemically treated Al 99.5 sheet [16].

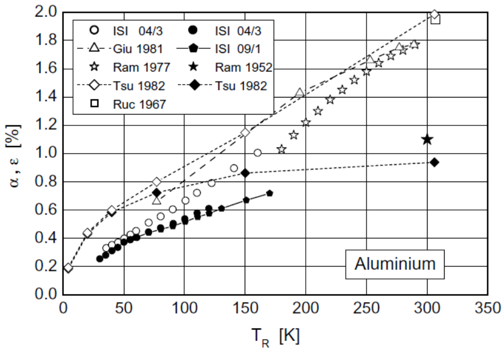

Figure 2.5. Total hemispherical absorptivity (solid symbols) and emissivity (open symbols) of solid Al as function of temperature from 4.2 K to 300 K [16].

several materials at various temperatures. The data approves that the assumption of the Kirchhoff law in Equation (2.24) is legitimate: “Emissivity of all measured samples approximately equalled absorptivity for [a] radiation temperature lower than 50 K. Above this temperature a difference between absorptivity and emissivity was observed only for surfaces of Al and Cu.” [16].

Figure 2.4 and Figure 2.5 confirm that the emissivity of aluminised polyester foil is lower at any temperature than the one of solid Al. For aluminised polyester foil at 50 K ε is 1.40 % and at 140 K about 1.75 %. Figure 2.5 indicates a strong drop for temperatures below 40 K for solid aluminium. As the data in Figure 2.4 ends for $T < 30$ K, this might also be the case for aluminised polyester foil.

2.3.2 Heat conduction through multi-layer insulation foils

MLI is used to reduce radiative heat flow depending on the number of layers and their emissive coefficient. An ideal MLI blanket would have foils without any touching points in between them. To avoid these touching points, polymer spacers are used to separate the foils. Even though these nets have a low thermal conductivity and a thread diameter of only about 50 µm [5, p. 1276], the MLI does still conduct heat: “However, as the hot-side temperature decreases from room temperature to cryogenic temperatures, the level of radiant heat transfer drops as the fourth power of the temperature, while the heat transfer by conduction only falls off linearly. This results in cryogenic MLI being dominated by conduction, a quantity that is extremely sensitive to MLI blanket construction and very poorly quantified in the literature.” [13].

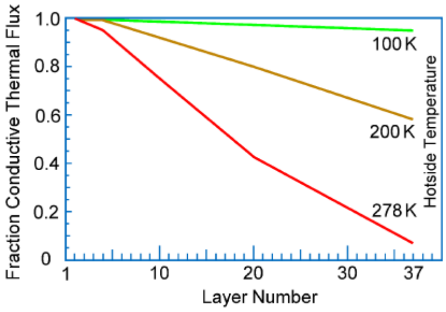

Figure 2.6. Radiant and conductive heat flow through 37-layer MLI for 3 different hot side temperatures [13].

The fraction of conductive heat flow in MLI applications to $\dot{q}_{\text{tot}}$ is shown by Figure 2.6. The lower the hot side temperature, the less import the radiative heat flow. “Below 100 K the 37-layer MLI is fully dominated by conduction.” [13]. “By 70 K the blanket crosses over to being worse than bare low-emittance surfaces (no blanket), and by 40 K the blanket has nearly four times the heat flux of bare low-emittance surfaces.” [13].

Undesirable heat conduction is linearly proportional to the mechanical pressure on the blankets, as shown in Figure 2.8. If no mechanical compression load crushes the blankets, the ratio of the conductive heat flow to total heat flow can be low. Evacuation, deformation of the surrounding walls or the dead load of the blankets themselves increase the compression load [5, p. 1276]. The last option can be decreased by using lightweight polymer foils such as Mylar instead of more heavy solid aluminium foils.

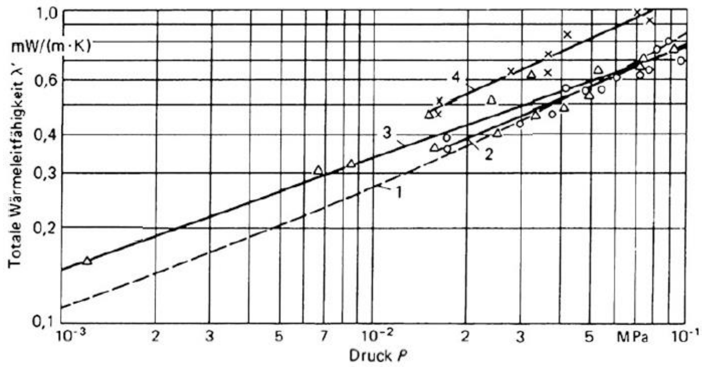

Figure 2.7. Pseudo-thermal conductivity (here: $k' = \lambda'$) (y-axis) as function of mechanical pressure P (x-axis) for different spacer types and thicknesses [5, p. 1279]. Axis titles in German.

To describe thermal conductivity of superinsulation, Reiss [5, p. 1279] uses the term pseudo-thermal conductivity. It describes a thermal conductivity, that has been derived with $k' = D\ \dot{q}\ /\ \Delta T$ and is dependent on the material thickness D instead of being an independent material constant [5, p. 1340]. The relative values of k' have the same expressiveness as of k, meaning that a high k' correlate with a high heat flux.

There is no general approach to quantify conductive heat flow through MLI [5, p. 1276]. However, for unperforated double-aluminised Mylar with single silk-net spacers for near-room-temperature it may be determined by the Lockheed equation [13]

$$\dot{q}_{\mathrm{MLI\,cond}} = \frac{\mathrm{C_c}\, N^{2.56}\, T_{\mathrm{m}}}{n}\,(T_{\mathrm{h}} - T_{\mathrm{c}}). \tag{2.29}$$

Here, $\mathrm{C_c}$ denotes a conduction constant $8.95 \cdot 10^{-5}$ mW m^{-2} K^{-2}, N denotes the MLI layer density in layers per cm and n the number of MLI layers. T_{m} represents the mean MLI temperature which is typically estimated with [13]

$$T_{\mathrm{m}} = \frac{(T_{\mathrm{h}} + T_{\mathrm{c}})}{2}. \tag{2.30}$$

The heat flux in Equation (2.29) is strongly dependent on the MLI layer density and reduces linearly with the number of layers. Besides, the number of layers typically increases the MLI layer density itself again for geometrically narrow chambers. Equation (2.29) is only useful for the described case due to the conduction constant. In contrast, Ross [13] describes the conductive heat flow for different temperature ranges down to ultra-low temperatures including consideration of different spacer materials or construction differences with

$$\dot{q}_{\mathrm{MLI\,cond}} = k_{\mathrm{o}}\,\kappa(T)\,\frac{(T_{\mathrm{h}} - T_{\mathrm{c}})}{n}. \tag{2.31}$$

His determination uses an MLI conductance $k_{\mathrm{o}}\,\kappa(T)$ which is given graphically in Figure 2.8.

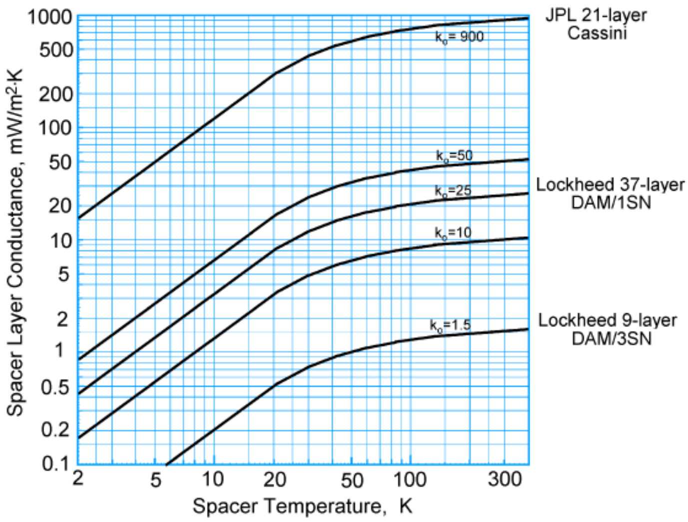

Figure 2.8. MLI conductance as function of temperature for different MLI blankets according to Ross [13].

The scale factor k_{o} now contains the blanket compression term $N^{2.56}$ from Equation (2.29) [13]. Ross gives a value of $k_{\mathrm{o}} = 25$ mW m^{-2} K^{-1} for a 37-layer double-aluminised Mylar with single silk-net spacers as an iterative result of his study.

As demonstrated, the conductive heat flow is strongly dependent on the MLI layer density and the radiative heat flow is inversely proportional to the number of layers, meaning that above a certain N, the radiative heat flow rarely decreases anymore but the conductive one increases. The consequence is an optimum number of layers [5, p. 1276].

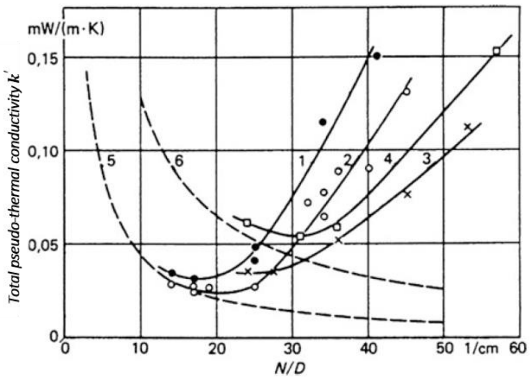

Figure 2.9. Total pseudo-thermal conductivity k' as function of MLI layer density with and without considering the conductive heat flow [5, p. 1279].

The graph in Figure 2.9 illustrates the influence of N on k': Graph 5 ($\varepsilon = 0.04$) and 6 ($\varepsilon = 0.12$) indicate theoretical values not considering $\dot{q}_{\mathrm{c}}$ (only radiation). The total pseudo-thermal conductivity decreases continuously with a higher MLI layer density. In contrast, graph 1, 2 and 3 represent measurements of Al-foils with glass fibre spacers of different thicknesses. Their pseudo-thermal conductivity has a minimum for $17 \lesssim N \lesssim 25$ layers per cm in this application [5, p. 1279].

To summarise the conductive heat flow through MLI, one can say that the "[…] MLI emittance is found to play a secondary role to spacer conductance in establishing MLI thermal effectiveness. Thus, MLI performance is critically dependent on the achieved MLI conductance." [13]. As the conductive heat flow is linear to the temperature difference according to Equation (2.29) and (2.31), the total heat flow $\dot{q}_{\mathrm{total}}$ seems to be $\propto T^2$, instead of $\dot{q}_{\mathrm{total}} \propto T^4$ for a domination of radiation. [13]

2.4 Thermo acoustic oscillations

Thermo acoustic oscillations (TAO) occur in systems with cold gas in a tube, that is closed at the warm end and open at the cold end with a large axial temperature gradient. "TAOs begin when the temperature gradient causes cold gas in the tube to warm and expand, thus increasing in pressure. This increased pressure then pushes the gas into the colder end of the tube, causing the pressure in the warmer end to fall. The gas then moves back to the warmer end to occupy this now lower pressure space. Under the proper conditions of tube size and temperature gradient, sustained pressure oscillations can be set up" [4, p. 40]. TAOs cannot only endanger the system with mechanical vibrations and damage components or gauges of a cryostat, it might also bring significant amounts of heat loads into a cryogenic system and needs to be avoided as much as possible in terms of a good thermal efficiency.

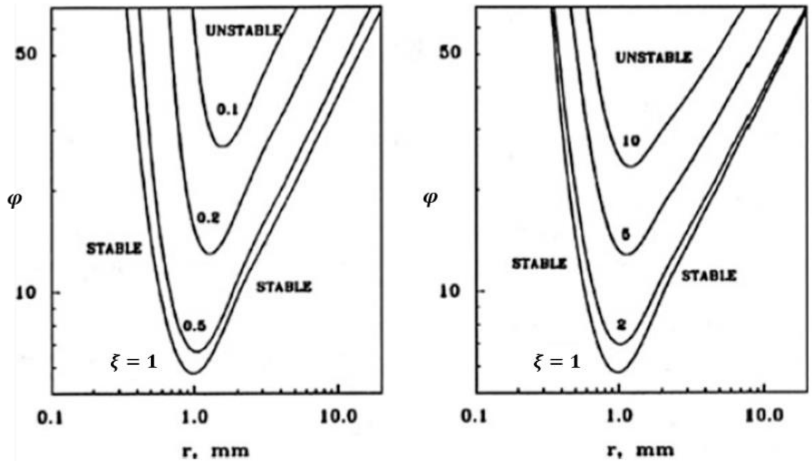

Figure 2.10. Stability maps of TAO for linear temperature gradient [4, p. 41]. The y-axis denotes φ and the x-axis r resp. r'. The stability fields are shown for different values of ξ.

The ratio of the hot temperature T_h to the cold temperature T_c [4, p. 40]

$$\varphi = \frac{T_\mathrm{h}}{T_\mathrm{c}} \tag{2.32}$$

and the ratio of warm tube length L_h to cold tube length L_c [4, p. 40]

$$\xi = \frac{L_\mathrm{h}}{L_\mathrm{c}} \tag{2.33}$$

define the stability map in Figure 2.10 for TAOs in a 1 m long tube with linear temperature gradient. A limit between L_h and L_c can be defined at the point with a temperature $T = (T_\mathrm{h} + T_\mathrm{c})/2$ [4, p. 40]. Besides, for a total tube length $L = L_\mathrm{h} + L_\mathrm{c} \neq 1$ m, the tube radius r has to be reduced to r' with L in m [4, p. 41]:

$$r' = \frac{r}{\sqrt{L}}. \tag{2.34}$$

The (un-) stable regions in Figure 2.10 show that the gas to wall friction damps the oscillation if the tube radius is small [4, p. 40]. If the tube radius is much larger, the gas inertia prevents the effect [4, p. 40]. The correlation depends on parameters such as the gas type or the thermal conductance of the tube and its ingoing heat flow [20, p. 2].

3 Thermodynamics of the ALPHA-g cryostat

The thermal conditions of the ALPHA-g cryostat can be seen as a steady state after a completed cool down. All incoming and outgoing powers are then in equilibrium condition. The following chapter will discuss the existing powers, mass flows and entropy flows that have to be considered for the thermal study.

3.1 Thermodynamic structure of the ALPHA-g cryostat

The ALPHA-g cryostat can be divided in three main shells or layers regarding the thermal study. Figure 3.1 on p.16 presents the outer-vacuum-chamber (OVC) shell (OVC box, base plate and OVC tail) in black with (a). The copper radiation shields are shown in orange with (b). The helium-space (He-space) is shown in blue with (c). Each shell is in constant energy exchange and either transfers or receives heat. The component names not mentioned in Figure 3.1 can be found in the referred *Projektarbeit* [2] and are not listed again here.

The boundary conditions are the stationary wall temperatures of the three main layers: 300 K at the OVC shell, 50 K at the copper radiation shields and 4 K at the helium-box (He-box). To calculate heat transfer from ambient through the thermodynamic system border, as well as inside the cryostat, the boundary conditions determine the results. They contain uncertainties and prohibit an exact result. To simplify the procedure, all calculations and simulations rely on the central assumption, that each single shell has a constant three-dimensional temperature distribution in steady state. In the real application this might not be the case. On the one hand, the shells have an inhomogeneous temperature distribution along the dimension of the wall thickness according to Equation (2.3). On the other hand, the temperatures vary along the surfaces. The legitimation of the mentioned assumption depends on the material and geometrical properties. This can be best explained on the example of heat radiation: For radiative heat transfer, the two surface temperatures of a single shell are considered as equal and homogenous. This assumption is justifiable for the copper shell. Copper is a great thermal conductor with $k(50\ \mathrm{K}) = 1005\ \mathrm{W\,m^{-1}\,K^{-1}}$ (oxygen free high-thermal conductivity (OFHC) copper, residual resistance ratio $RRR = 100$) [21]. Additionally, its shell thickness is only 1.6 mm. One could assume a total heat flux onto the radiation shields of $\sim 2\ \mathrm{W\,m^{-2}}$. The differential temperature in steady state of the outer wall surface T_{bo} and the inner of T_{bi} would be relatively low with

$$T_{\mathrm{bo}} = T_{\mathrm{bi}} = \Delta T_{\mathrm{bc}} = \frac{\dot{q}_{\mathrm{tot\,bc}}\ s_{\mathrm{b}}}{k_{\mathrm{b}}} = \frac{2\ \mathrm{W\,m^{-2}} \cdot\ 0.0016\ \mathrm{m}}{1005\ \mathrm{W\,m^{-1}\,K^{-1}}} \approx 3 \cdot 10^{-6}\ \mathrm{K}. \tag{3.1}$$

However, this is not the case for stainless steel. Stainless steel is a bad thermal conductor with $k(300\ \mathrm{K}) = 15.31\ \mathrm{W\,m^{-1}\,K^{-1}}$ (for steel type 316) [21]. Additionally, the shell thickness of the OVC box s_{a} and the He-box s_{c} is both 25 mm:

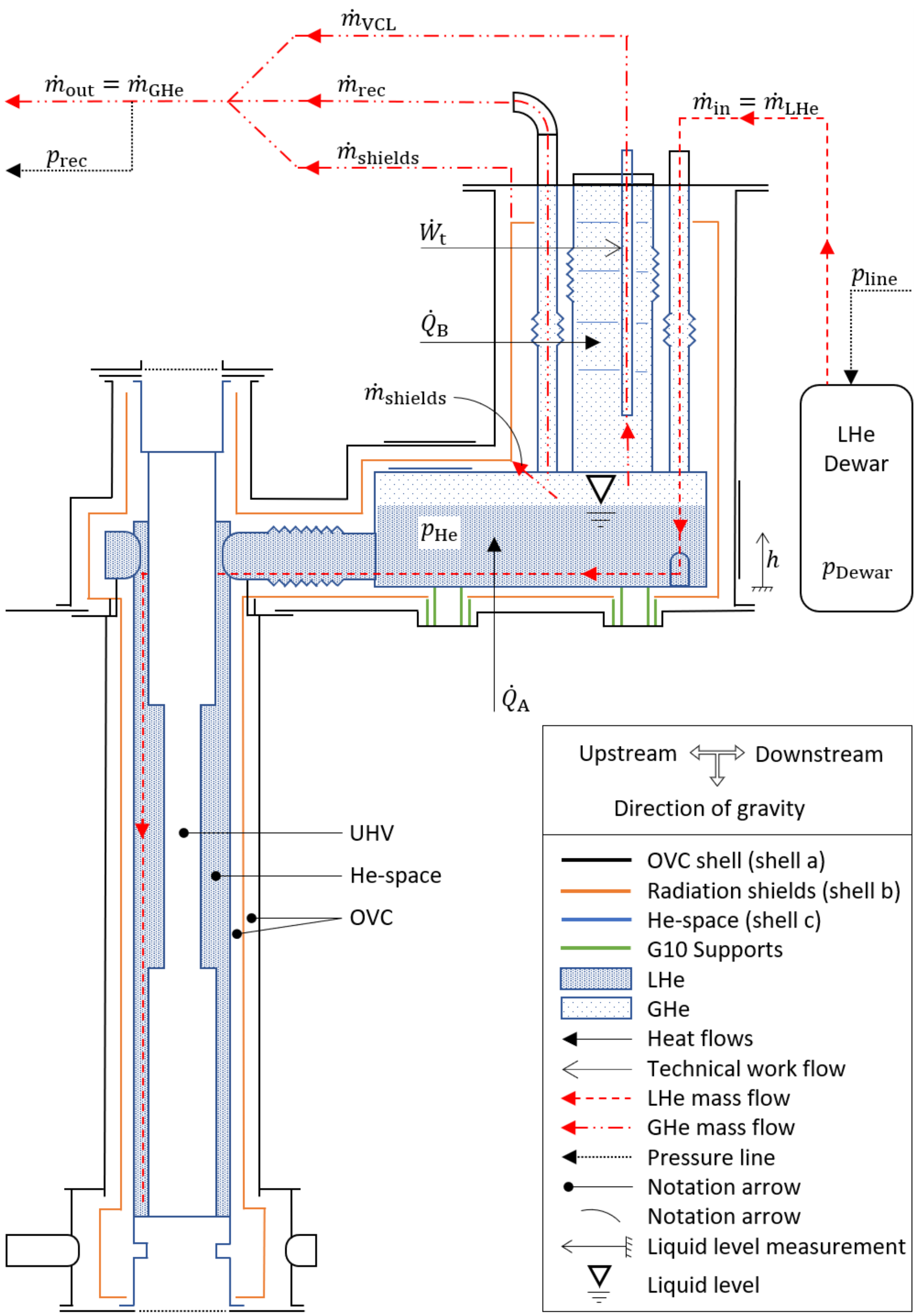

Figure 3.1. Schematic illustration of the ALPHA-g cryostat in half-section view. The three main shells ‘a’, ‘b’ and ‘c’ are shown with colour coding according to the legend. In addition to the physical apparatus, flows of heat, technical work and masses are marked, as well as the pressures in the different sections of the cryostat. The liquid level corresponds approx. to the operational level. The total height of the cryostat is ~5 m. The dimensions are not to scale. Physical quantities are described in chapters 3.2 (p.17), 3.4 (p.18), 3.5 (p.21) and 3.8 (p.25).

$$T_{\mathrm{ao}} - T_{\mathrm{ai}} = \Delta T_{\mathrm{wa}} = \frac{\dot{q}_{\mathrm{tot\,air-a}}\ s_{\mathrm{a}}}{k_{\mathrm{a}}} = \frac{2\ \mathrm{W\,m^{-2}} \cdot\ 0.025\ \mathrm{m}}{15.31\ \mathrm{W\,m^{-1}\,K^{-1}}} \approx 0.003\ \mathrm{K}. \tag{3.2}$$

In shell c the thermal conductivity is much lower due to the low temperatures with $k(4.2\ \mathrm{K}) = 0.2724\ \mathrm{W\,m^{-1}\,K^{-1}}$ [21]. Also here, it leads to a small differential temperature of

$$T_{\mathrm{co}} = T_{\mathrm{ci}} = \Delta T_{\mathrm{wc}} = \frac{\dot{q}_{\mathrm{tot\,bc}}\ s_{\mathrm{c}}}{k_{\mathrm{c}}} = \frac{2\ \mathrm{W\,m^{-2}} \cdot\ 0.025\ \mathrm{m}}{0.2724\ \mathrm{W\,m^{-1}\,K^{-1}}} \approx 0.18\ \mathrm{K}. \tag{3.3}$$

Due to the small differential temperatures on the shells and the complex thermal conditions inside the cryostat with dependencies of all separate thermal systems, the mentioned assumptions will be carried out in all following calculations.

3.2 Challenges of a cryostat with liquid helium

The main of the cryostat is to provide a cold LHe bath at 4 K to cool superconducting magnets as well as electrodes, in addition to cryopump an ultra-high vacuum chamber. Every incoming heat flow results in a lower thermal efficiency. However, as the cryostat contains a 2-phase system with liquid and gaseous helium He, one must differentiate between ‘A’ heat in-flows $\dot{Q}_{\mathrm{A}}$ and ‘B’ heat in-flows $\dot{Q}_{\mathrm{B}}$ as shown in Figure 3.1. The fluid has a certain liquid level inside the storage vessel. Whereas ‘A’ heat in-flows evaporate LHe, ‘B’ heat in-flows only increase the gaseous enthalpy [22, p. 42]. “With good design, the ‘B’ heat flows may not contribute to the evaporation at all, although they may rely on a minimum vapour mass flow generated by ‘A’ heat flows“ [22, p. 42].

LHe is an expensive fluid depending on its purity. It can cost up to $35 per litre [23]. Although CERN has its own liquifying and distribution system and ALPHA does not need to pay for LHe, the costs for CERN are still high and the production consumes much energy. As goal for the ALPHA-g cryostat, the maximum LHe consumption $\dot{V}_{\mathrm{max}}$ must not exceed ~20 litres per hour.

A central challenge of a LHe cryostat is the extremely low enthalpy of vaporization Δh^{v} of 20.72 kJ kg^{-1} when boiling at norm pressure [22, p. 43] and 19.54 kJ kg^{-1} at 1.20 bar [24, p. 36]. The Δh^{v} at norm pressure of other cryogenic fluids such as nitrogen N_2 or oxygen O_2 is about an order of magnitude higher. A different but not very fair comparison would be the one to water, which has an Δh^{v} of 2260 kJ kg^{-1} [25, p. 703]. As a result, little ‘A’ heat-in flows evaporate large amounts of LHe. One can imagine, that this fundamental fluid property dictates the complexity of the LHe cryostat design.

In comparison to the extraordinary small Δh^{v} of LHe, the enthalpy difference $\Delta h^{\mathrm{g}}_{4\,\mathrm{K}\rightarrow 300\,\mathrm{K}}$ of gaseous helium (GHe) from 4 K to 300 K is with 1543 kJ kg^{-1} about 75 times higher [24, p. 34]. The enthalpy of GHe for cryogenic temperatures increases about linearly with temperature at from 6 K to 300 K at 1 bar [26, p. 17]. For higher pressure, the enthalpy drifts stronger from the ideal gas linearity. More thermodynamic properties of liquid and gaseous helium by NIST can be found in [24, p. 34] for norm pressure and in [24, p. 36] for 1.20 bar.

3.3 Copper radiation shield unit

The ALPHA-g cryostat uses cooling power of evaporated helium gas mentioned in chapter 3.8.4 to improve the thermal efficiency, by cooling a radiation shield unit: Some of the evaporated LHe inside the He-space flows through the flute into a gas distribution system. It connects the helium vessel with 7 copper radiation shields. On these shields, there are copper tubes brazed to with a high large contact surface for good thermal conduction. The exit of the gas tubing system is connected with 6 individual valves that regulate the gas flow and maintain a constant temperature of 50 K. Thermal sensors on the shields monitor the resulting temperature.

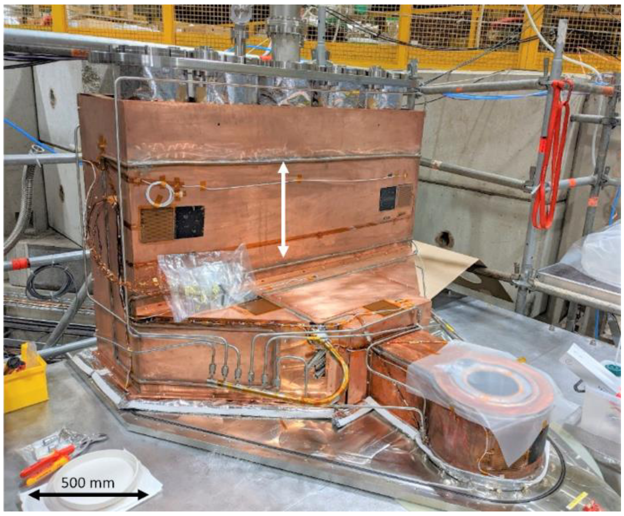

Figure 3.2. Copper shields of the upper part of ALPHA-g before the installation of the OVC box in May 2021. The gas distribution system from the shield tubes to the copper shiels are visible.

As mentioned in section 3.1, the assumption that that each single shell has a constant three-dimensional temperature distribution in steady state is made. It is important to mention this again, because the gas tubes on the copper shields have large distances in between each other. The white arrow in Figure 3.2 indicates the distance of the tubes on one shield to highlight a possible inhomogeneous temperature distribution. However, the original design took this into account and chose appropriate tubing distances. A more detailed investigation of the temperature distribution in the shields will therefore not be carried out in this thesis.

3.4 Liquid and gaseous helium mass flows in the cryostat

Due to a 2-phase system, discussed in chapter 3.2, liquid as well as gaseous helium is located in the He-space of the ALPHA-g cryostat. Figure 3.1 indicates the incoming and outgoing helium mass flows of the cryostat and pressures in the helium system. The general flow direction is from right to left. A storage volume 'LHe Dewar' transfers LHe into the cryostat, where some of it evaporates due to heat leaks. The evaporated GHe has three options to exit the cryostat:

- It enters the copper shields for cooling and exits into the recovery line (indicated by $\dot{m}_{\text{shields}}$ with an inlet inside the He-space and an outlet outside the cryostat).
- It enters the vapour-cooled leads (VCL) for cooling (indicated by $\dot{m}_{\text{VCL}}$).
- It flows directly through a service tube into the recovery line (indicated by $\dot{m}_{\text{rec}}$).

To push out the GHe through the mentioned gas systems, it is mandatory to run a slight overpressure inside the cryostat. A He-space pressure of ~100 to 150 mbar higher than ambient pressure was used during several cold tests in 2021. The gaseous enthalpy $\Delta h^{g}_{4\,\mathrm{K}\rightarrow 300\,\mathrm{K}}$, also discussed in chapter 3.1, is 1543 kJ kg^{-1} at norm pressure [24, p. 34] as well as at 1.20 bar [24, p. 36].

3.5 Liquid helium inside the helium space

Liquid is located inside the tail, the horizontal bellow and the He-box. As a key component, its thermodynamic influence on the ALPHA-g cryostat will be considered in the following chapter.

3.5.1 Transfer of LHe into the cryostat

The LHe gets transferred from a storage Dewar into the cryostat. The connecting transfer system consists of a transfer line and a stinger. The stinger is inserted into the He-space of the ALPHA-g cryostat and directs the LHe into a cup on the bottom of the He-box, as presented in Figure 3.1. At this position, the LHe gets guided into upstream direction, through the horizontal bellow and downwards to the bottom of the tail. Here, it finally exits the transfer tube and fills the cryostat from the bottom to the top.

3.5.2 Transfer line

Transfer lines provide liquid cryogenic fluids for cryostat vessels. They can be seen as a small cryostat themselves. For ALPHA-g, a flexible type of transfer line is used. Especially for temporary tests the flexibility is convenient. Common flexible transfer lines have a two-shell structure with an evacuated chamber in between to lower residual gas convection and conduction to a minimum. While the outer tube provides the vacuum and protection, the inner tube transfers the actual liquid fluid. Typical outer diameters are around 34 mm and inner diameters around 6 or 8 mm [27]. The vacuum chamber can usually be connected to a pump and has a typical pressure of 10^{-5} mbar. Just as on the main ALPHA-g cryostat, superinsulation inside the transfer line reduces heat radiation. In general, it is aimed for a one-phase transfer of only liquid. A vaporisation of small amounts of LHe already fills a large volume of the transfer line due do the volume ratio of 738 [22, p. 8] for GHe to LHe. Two-phase transfer becomes highly inefficient in terms of LHe supply.

3.5.3 LHe level inside the He-space

The following chapter discusses the liquid level and gives a function of the LHe volume.

As explained in chapter 3.5.1, the ALPHA-g cryostat gets filled with LHe from the bottom of the tail to the top. In this first section, there is no level measuring device implemented. Only when the liquid reaches the He-box, an actual liquid level h gets measured. This is shown in Figure 3.1 between cryostat and Dewar. The LHe level is read out by a special LHe probe that is located inside a service tube and touches the bottom of the He-box. The level probe is manufactured by American Magnetics Inc. and its output is in % liquid level. A correlation of this liquid level in %, actual liquid height and a resulting LHe volume can be obtained by comparing the probe length with the He-box geometry. With a total probe length of 250 mm and 100 % as maximum output, 1 cm corresponds to 4 % of liquid level. The resulting LHe volume $V(h)$ is a non-linear function of the liquid level h due to sudden changes in geometry. To determine a complete correlation of $V(h)$, one has to respect three main sections: (1) He-box, (2) horizontal pipe section that connects the He-box to the tail including the horizontal bellow and (3) vertical tail including the magnet. A summation of the individual volumes $V_i(h)$ leads to $V(h) = V_1(h) + V_2(h) + V_3(h)$.

For section '1', the horizontal surface area inside the He-box A_1 is 64.8 dm^2 without taking into account objects in the liquid. It leads to a linear influence on the volume of $V_1(h) = h \cdot A_1$ and has the largest ratio of $V(h)$. The additional volume of the liquid inside section '2' is a nonlinear function of h. Considering a trigonometric description of a circular segment area $A_{\ominus}$ with the length $L_2 = 566$ mm and radius $r = 51$ mm, the volume in this section is given with [28, p. 21]

$$V_2(h) = L_2 \cdot A_{\ominus}(h) = L_2 \cdot r^2 \cdot \arccos\left(1 - \frac{h}{r}\right) - (r-h) \cdot \sqrt{r^2 - (r-h)^2}. \tag{3.4}$$

The section '2' is completely filled at $h_{2\,\mathrm{max}} = 2 \cdot r = 10.3$ cm with $V_{2\,\mathrm{max}} \approx 4.7$ L.

In section '3', the amount of liquid that is located in the lower tail section is constant and not a function of h, because the level measuring starts only at $h = 0$ as shown in Figure 3.1. It is enclosed by the inner tail wall and surrounds the atom trap which is bathing in it. The height of this constant volume in the lower section $V_{\mathrm{lower\ tail}}$ reaches from the bottom of the He-space up to at $h = 0$. To estimate $V_{\mathrm{lower\ tail}}$, one can subtract the displacement volume of the atom trap of 8.2 L from the inner volume of the tail of 14.2 L. The remaining constant LHe volume is given with $V_{\mathrm{tail}} = 6.0$ L. In contrast, the upper tail section has a little volume linear to h when reaching the level probe. With an annular cross section-area $A_3 = 0.23\ \mathrm{dm}^2$ around the atom trap, the liquid volume in the tail can be obtained with $V_3(h) = V_{\mathrm{lower\ tail}} + h \cdot A_3$. The tail is entirely filled at $h_{3\,\mathrm{max}} = 16.0$ cm, whereas the upper section is negligible with only 0.4 L.

The complete function to describe the liquid volume measured by the level probe adds up to

$$V(h) = \begin{cases} V_1(h) + V_2(h) + V_3(h), & 0 < h \leq 10.3 \text{ cm} \\ V_1(h) + V_{2\,\mathrm{max}} + V_3(h), & 10.3 \text{ cm} < h \leq 16 \text{ cm} \\ V_1(h) + V_{2\,\mathrm{max}} + V_{3\,\mathrm{max}}, & 16 \text{ cm} < h \leq 17.5 \text{ cm}. \end{cases} \tag{3.5}$$

The corresponding individual volumes and surface areas can be found in Table 3.1.

Table 3.1. Geometric data used for the determination of the LHe volume V as function of LHe level h.

Physical property	Section 1: He-box	Section 2: horizontal bellow and adjacent sections	Section 3: vertical tail
$V_i(h)$	$h \cdot A_1$	$L_2 \cdot A_{\ominus}(h) = 56.6\ \mathrm{cm} \cdot A_{\ominus}(h)$	$V_{\mathrm{lower\ tail}} + h \cdot A_3 = 6.0\ \mathrm{L} + h \cdot A_3$
$V_{i\,\mathrm{max}}$	113.4 L	4.7 L	6.4 L
A_i	64.8 dm^2	$A_{\ominus}(h)$	0.23 dm^2
$h_{i\,\mathrm{max}}$	17.5 cm	10.3 cm	16.0 cm

In the experiment it is aimed for a constant operational liquid level of $h = 150$ mm, which corresponds to 60 %. The liquid volume $V(h)$ at this level would be 101 L, not considering objects inside the He-box. The distance between the bottom and ceiling of the He-box is 175 mm which corresponds to 70 %.

3.5.4 Regulation of LHe level

A safe regulation of the LHe level is mandatory to allow safe and functional conditions. Several parameters such as pressures, flow rates or temperatures need to be taken into account, to maintain a certain operational level and avoid deficits of LHe which would result in an inadvertent magnet warm up in worst case. In contrast, an overfill could change essential temperature distributions, might cool down upper sections of the cryostat, freeze large amounts of air moisture or open up leaks into the OVC.

In general, the amount of vaporised LHe in steady state due to 'A' heat-in flows needs to be continuously refilled: $\dot{m}_{\mathrm{in}}^{\mathrm{LHe}} = \dot{m}_{\mathrm{vaporised}}^{\mathrm{LHe}} = \dot{m}_{\mathrm{out}}^{\mathrm{GHe}}$. During a cool down or warm up, $\dot{m}_{\mathrm{in}}^{\mathrm{LHe}}$ is higher resp. lower and needs to be regulated in a controlled way. To adjust the transfer rate, the right proportions between four pressures are mandatory, indicated in Figure 3.1: the Dewar pressure p_{Dew}, the He-space pressure p_{He}, the recovery pressure p_{rec} and the gas line pressure p_{line}. While p_{line} and p_{rec} can be seen as dominating, p_{Dew} and p_{He} adjust itself to these two pressures. The result is a mass balance in He-space of $\sum \dot{m} = 0$ in steady state (see also chapter 3.8.1). On the filling side, the higher the ratio of p_{Dew} to p_{He} is, the bigger $\dot{m}_{\mathrm{in}}^{\mathrm{LHe}}$. The Dewar pressure depends on the gas line pressure that it is connected to and whether and how far an isochoric state changed happened due to heat leaks into the Dewar. On the emptying side, the higher the ratio of p_{He} to p_{rec} is, the bigger $\dot{m}_{\mathrm{out}}^{\mathrm{GHe}}$.

One has to take into account that the recovery pressure might suddenly change when other experiments in the AD hall (dis-)connects a large mass flow or pressure difference. Additionally, thermo acoustic oscillations in the recovery line could cause a backflow from recovery into He-space (see also chapter 4.8.1). The same principle needs to be considered when regulating the gas line pressure. (Dis-)connecting large systems inside the ALPHA experiment could change p_{line}.

3.6 GHe influence on the thermodynamic conditions inside the helium-space

When heat leaks enter a cryostat and evaporate liquid, the resulting gas ascends. Vapour convections form on the way to the outlet which can have a strong influence on the thermodynamic states inside the cryostat. The following chapter will highlight the importance of this convection and present a description and quantification of the general conditions in the gas phase.

3.6.1 General vapour convection in a 2-phase cryostat

When a liquid fluid gets transferred into a cryostat, some amount of it evaporates. The gas fills the accessible vapour space above the liquid with a commonly large temperature gradient from boiling temperature up to ambient temperature, which results in a certain density stratification of the vapour. However, "there is considerable convective motion of the vapour." [22, p. 44]. The general source of the convection is "heating of the vapour by the wall [which] generates a strong natural convective boundary layer flow up the wall. At the same time, there is a reverse flow in the centre of the vapour column which carries heat as an 'A' in-flow to the surface of the liquid." [22, p. 44]. This vapour motion is shown in Figure 3.3.

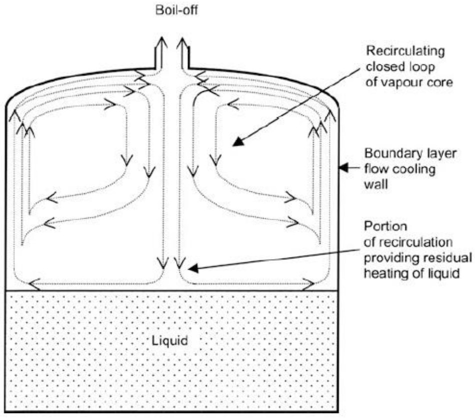

Figure 3.3. Schematic convection of vapour inside a 2-phase cryostat with recirculating loops in the gas phase [22, p. 45].

Convection mixes the vapour along the circulating loop direction. The mentioned density stratification is then no longer present or only present weakly. If the convection is strong enough - meaning that it has a high velocity and large amounts of vapour mass circulating - one might see a temperature gradient in the vapour as non-existent. In contrast, a homogenous vapour temperature establishes.

The flow conditions such as vapour velocity or Reynolds number depend on several parameters. These are e.g. the fluid temperature and pressure, the amount of vaporised liquid per time unit and the size of the liquid surface. Additional influence is caused by the size, temperature and roughness of the wall surface or the general vessel geometry.

Beside the heat input into the liquid, another effect of vapour convection is the cooling of the vessel walls, which "can be used to absorb, as 'B' heat in-flows, part or all of the conducted heat flows down the walls which would otherwise enter the liquid as 'A' heat in-flows." [22, p. 45]. A quantification of how much conductive heat flow in the vessel wall is absorbed in practice is difficult to determine and requires a more precise consideration of the vapour flow conditions.

3.6.2 GHe in the ALPHA-g cryostat

A relevant proportion of the He-space volume inside the ALPHA-g cryostat is filled with vapour. It is located inside the He-box above the liquid, completely fills the chimneys and service tubes, as well as radiation shield tubes and the VCL. The corresponding vapour volumes are shown in Table 3.2. An operational liquid level of $h = 15$ cm resp. 60 % is considered. The volumes refer to the entire unit in each section, i.e., to all five chimneys and seven service tubes. The volumes inside the shield tubes and VCL are not presented in Table 3.2, since they are not part of the convection considered here and are accounted for in a separate thermodynamic system. The radiation shield tube volume can be estimated to 0.6 L . The tubing system has a total length of ~ 31 m of copper tubes and ~ 11 m of feed tubes. The GHe volume inside the VCL is unknown as the manufacturer does not provide this technical detail. The data was acquired by using the CAD models in Autodesk Inventor. To compute displacement volumes, the function 'Shrinkwrap' was used to fill enclosed cavities.

Table 3.2. GHe volumes V_i in the ALPHA-g cryostat. The volumes in the VCL and shield tubes are not presented.

Physical property	Section 1: He-box	Section 2: Chimneys	Section 3: Service tubes
V_i	16.2 L	123.2 L	4.8 L
Number of components	1	5	7
Open towards the top?	yes	no	2 yes, 5 no
Baffles included	no	yes	no

The total vapour volume in He-space at $h = 15$ cm resp. 60 % is ~144 L, whereas the largest amount of vapour is located in the chimney with ~86 % (incl. consideration of the HTS). In the He-box, there are additional ~11 %, while the service tubes have a little ratio of only ~3 %.

To estimate the convective conditions in the He-space, the proportions of vapour volume have a strong influence. Besides, it is important to consider the geometry of the cryostat. Especially the location of gas outlets. In components that are only geometrically linked in one of 6 axial directions of space, convection might become negligible. The gas might stratify depending on its density. The helium box plays a central role for the convection. Although it does not have the largest share of the gas volume, it could control the convection conditions due to the liquid level it contains. It is partly open towards the top on its openings to the chimneys and service tubes. This proportion represents around 26 % of the liquid surface. In contrast, all five chimneys and five of the seven service tubes are closed in upwards direction. For the chimneys, the top is closed by the HTS. There is no actual GHe flow inside them. Furthermore, there are nine baffles located inside them that inhibit vertical convection. For five of the seven service tubes, the top is closed with components such as burst disks or cable feedthrough flanges. The remaining two service tubes are used as opening to the recovery line and have an actual gas flow inside them.

An approach to determine possible free convection in the chimneys and service tubes will be further discussed in chapter 4.6.5 and 4.6.6.

3.6.3 Demand of GHe for cooling cycles inside the cryostat and optimum shield temperature

When LHe evaporates inside the He-box it can exit in three ways, as discussed in chapter 3.4. It either enters the shield tubing system to cool the copper shields, enters the VCL or directly exits the cryostat through the recovery line. In the last option, the cooling power of the GHe is lost. Therefore, the ratio of these mass flows dictates the thermal efficiency of the apparatus. To achieve an appropriate thermal efficiency, as much cold GHe should be used to cool components as possible. The higher the output temperature resp. enthalpy of the vapour, the lower the cooling power loss.

Cold GHe is a precious cooling resource. Availability and demand exist in a delicate state of equilibrium. A complex interaction of single thermodynamic systems dictates this demand of GHe and therefore also of LHe. A first understanding can be obtained by looking at the copper radiation shield system more detailed.

In general, a lower shield temperature T_{b} demands a higher cooling power of the shields, meaning a higher GHe mass flow through the shield tubes. A lowered T_{b} reduces the total ‘A’ and ‘B’ heat-in flow from the shields (shell ‘b’) to the He-space (shell ‘c’) $\dot{Q}_{\mathrm{bc}}$. It results in a lower vaporisation and consumption of LHe. Although this is a positive effect in general, the GHe demand increases, which leads to a lower availability of GHe for the VCL cooling. It should be noted that a low shield temperature must be weighed against the 'cost' of a high GHe demand. Additionally, lower ‘A’ heat-in flows resp. lower LHe vaporisation reduce the availability of GHe and its cooling power. On some circumstances, one would need to boil off LHe with the help of heaters located inside the He-box. As part of $\dot{Q}_{\mathrm{bc}}$, the radiative heat flow is proportional to T^4 and drops strongly at cryogenic temperatures, whereas the conductive heat flow is linear to T. Lowering the shield temperature T_{b} close to 4 K might not be efficient at all. The GHe demand to reach this low T_{b} might not equal the additional benefit of the decreased heat flow $\dot{Q}_{\mathrm{bc}}$. Out of these two conflicting factors, an optimal shield temperature results that will be further investigated in chapter 4.7.14.7.

To sum up it can be said that a low shield temperature reduces $\dot{Q}_{\mathrm{bc}}$ with a positive effect on the LHe consumption. This requires large amounts of GHe which might be needed to cool the VCL instead. The result is an optimal T_{b}.

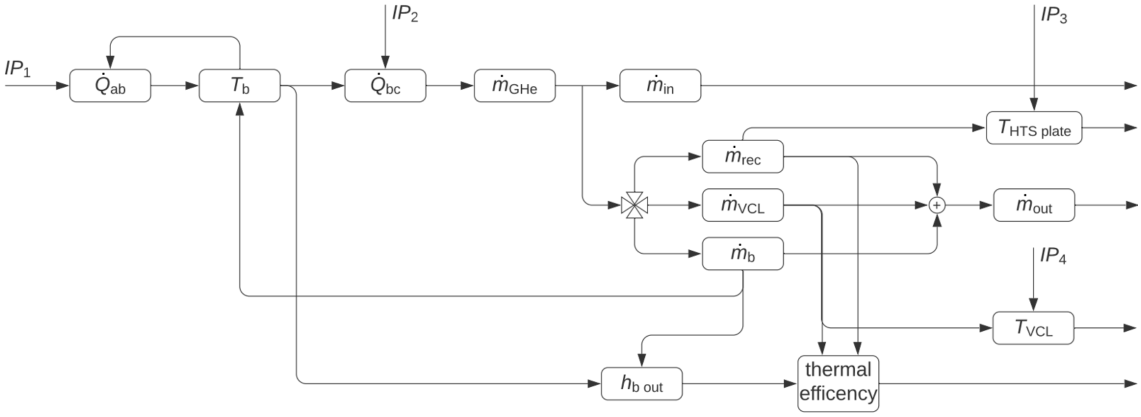

Figure 3.4. Schematic flow chart describing the GHe demand with mutual parameter dependencies.

The correlation of mass flow through the copper shield tubes $\dot{m}_{\mathrm{b}}$ and the shield temperature T_{b} is shown in Figure 3.4. Mutual dependencies of several individual parameters describe the GHe demand. Arrows in the flow chart represent direct influence of a variable to the indicated one.

Starting on the left side, certain input parameters IP_1 (such as the OVC pressure or the ambient air temperature) determine together with T_{b} the total heat flow from shell ‘a’ to ‘b’ $\dot{Q}_{\mathrm{ab}}$. This heat flow then acts on the radiation shield system. Together with $\dot{m}_{\mathrm{b}}$ and corresponding enthalpies it leads to a certain T_{b}. A low or high T_{b} results together with IP_2 (such as OVC pressure) in a low or high $\dot{Q}_{\mathrm{bc}}$. A corresponding mass flow $\dot{m}_{\mathrm{GHe}}$ gets vaporised. For a steady liquid level, $\dot{m}_{\mathrm{GHe}}$ must equal the incoming/transferred mass flow $\dot{m}_{\mathrm{in}}$ (see also chapter 3.8.1). Vaporised helium now ascends and gets distributed into the three gas systems. Depending on the valve positions, a proportion of $\dot{m}_{\mathrm{GHe}}$ flows into the shield system and cools shell ‘b’. One can see that a high $\dot{m}_{\mathrm{b}}$ also decreases the sum of the mass flows for the VCL and recovery $\dot{m}_{\mathrm{VCL}} + \dot{m}_{\mathrm{rec}}$. Following, $\dot{m}_{\mathrm{VCL}}$ has an influence on the VCL temperature T_{VCL} together with IP_3 (such as VCL current), while $\dot{m}_{\mathrm{rec}}$ acts on the HTS plate temperature $T_{\mathrm{HTS\,plate}}$ together with IP_3 (such as ambient air temperature, air convection and HTS plate heater power). Finally, the ratio of the different mass flows with the enthalpy of the shield system outlet $h_{\mathrm{b\,out}}$ has an influence on the thermal efficiency of the full cryostat. On the right side of the flow chart, one can see relevant outgoing parameters for the experiment: required incoming LHe mass flow, outgoing GHe mass flow, HTS plate and VCL temperature, as well as the general thermal efficiency.

3.7 Surface size of the individual shells

This chapter presents the surfaces sizes of the individual shells ‘a’, ‘b’ and ‘c’ (see Figure 3.1). They will be used in chapter 4 to determine heat flows.

The individual shells of the cryostat are closely spaced in many areas, with separation distances of less than 15 mm. In the upper area of the cryostat above the He-box, the shells are further apart with distances of up to 80 mm. This dense structure leads to similar surface sizes of the shells with a decrease in size towards the inside. Shell 'a' has a total inner surface area of about $A_{\mathrm{a,tot}} = 7.88\ \mathrm{m}^2$. Shell 'b' is close to this value at around $A_{\mathrm{b,tot}} = 7.42\ \mathrm{m}^2$. Shell 'c' has the smallest surface area of around $A_{\mathrm{c,tot}} = 6.83\ \mathrm{m}^2$. The surface sizes were derived from the Autodesk Inventor CAD models.

For the calculation of the heat flows, an additional separation of the surfaces into the area of 'A' heat-in flows and 'B' heat-in flows is necessary. This does not apply for shell ‘a’, as it transfers heat through MLI only to shell ‘b’ but not to ‘c’ directly. With an operational LHe level of $h = 15\ \mathrm{cm}$ as discussed in chapter 3.5.3, the surface sizes presented in Table 3.3 result:

Table 3.3. Surface area sizes of the individual shells considering an operational LHe level of $h = 15$ cm.

Surface area	Heat-in flow type	Shell ‘a’	Shell ‘b’	Shell ‘c’
$A_{i\mathrm{.tot}}$ in m²	A and B	7.88	7.42	6.83
$A_{i\mathrm{,LHe}}$ in m²	A	-	3.72	2.55
$A_{i\mathrm{,GHe}}$ in m²	B	-	3.17	4.28

It should be noted that in shell 'b' $A_{\mathrm{b,LHe}} + A_{\mathrm{b,GHe}} \neq A_{\mathrm{c,tot}}$ because parts of the shields are located outside the He-space (helmet and tail bottom shield).

3.8 Thermodynamic balances of the ALPHA-g cryostat

In this chapter, a thermodynamic investigation of the full ALPHA-g cryostat is carried out. The ALPHA-g cryostat can be seen as an open thermodynamic system in steady state after a completed cool down. A thermodynamic system in steady state has three balances that equal zero: The mass, energy and entropy balance. The control volume border of the open thermodynamic system of the ALPHA-g cryostat is indicated in Figure 3.1 as the OVC shell (shell ‘a’). Additionally, all relevant rates of energy and the mass are shown. Rates of entropy are not indicated.

3.8.1 Mass balance and helium-space pressure

The mass balance of a control volume (CV) [29, p. 223]

$$\frac{\mathrm{d}m^{\mathrm{CV}}}{\mathrm{d}t} = \sum \dot{m}_{\mathrm{in}} - \sum \dot{m}_{\mathrm{out}} \tag{3.6}$$

equals zero for steady states. For all incoming and outgoing mass flows of the ALPHA-g cryostat, the balance is given with

$$\frac{\mathrm{d}m^{\mathrm{CV}}}{\mathrm{d}t} = 0 = \dot{m}_{\mathrm{LHe}} - \dot{m}_{\mathrm{GHe}} + \dot{m}_{\mathrm{OVC\,leak}} - \dot{m}_{\mathrm{throughput}}. \tag{3.7}$$

Assuming the mass flow of leaks from air to OVC $\dot{m}_{\mathrm{OVC\,leak}}$ and the throughput of the turbo pump at high vacuum $\dot{m}_{\mathrm{throughput}}$ are negligible (≈ 0), the liquid and gaseous He mass flows indicated in Figure 3.1 on p.16 are equal:

$$\dot{m}_{\mathrm{LHe}} = \dot{m}_{\mathrm{GHe}} = \dot{m} \tag{3.8}$$

3.8.2 Power balance of the ALPHA-g cryostat

The rate of energy for an open thermodynamic system is given with [29, p. 228]

$$\begin{aligned} \frac{\mathrm{d}E_{\mathrm{total}}^{\mathrm{CV}}}{\mathrm{d}t} &= \underbrace{\frac{\mathrm{d}E_{\mathrm{kin}}^{\mathrm{CV}}}{\mathrm{d}t}}_{\approx 0} + \underbrace{\frac{\mathrm{d}E_{\mathrm{pot}}^{\mathrm{CV}}}{\mathrm{d}t}}_{\approx 0} + \underbrace{\frac{\mathrm{d}U^{\mathrm{CV}}}{\mathrm{d}t}}_{= 0} \\ &= \underbrace{\sum \dot{W}}_{\dot{W}_{\mathrm{t}} + \underbrace{\dot{W}_{\mathrm{V}}}_{= 0}} + \sum \dot{Q} + \dot{m}\left(h_{\mathrm{in}} + \frac{v_{\mathrm{in}}^2}{2} + \mathrm{g}\, z_{\mathrm{in}} - h_{\mathrm{out}} - \frac{v_{\mathrm{out}}^2}{2} - \mathrm{g}\, z_{\mathrm{out}}\right). \end{aligned} \tag{3.9}$$

The total rate of energy equals zero for a steady state. The isochoric conditions result in the rate of work of volume change $\dot{W}_{\mathrm{V}} = 0$. Furthermore, it is assumed that the difference of the kinetic power $\dot{m}\,\left(v_{\mathrm{in}}^2 - v_{\mathrm{out}}^2\right)/2$ and the potential power $\dot{m}\,\mathrm{g}\,(z_{\mathrm{in}} - z_{\mathrm{out}})$. Therefore, Equation (3.9) can be simplified for the ALPHA-g cryostat to

$$0 = \frac{\mathrm{d}E_{\mathrm{total}}^{\mathrm{CV}}}{\mathrm{d}t} = \sum \dot{W}_{\mathrm{t}} + \sum \dot{Q} + \dot{m}\left(\underbrace{h_{\mathrm{in}} - h_{\mathrm{out}}}_{\Delta h_{\mathrm{in,out}}}\right). \tag{3.10}$$

The rate of technical works $\dot{W}_{\mathrm{t}}$ combines all electrical and mechanical powers that cross the CV border. Hereby, the electric power for the VCL and the heating of level probe have the biggest influence. Powers introduced by the turbo pump throughput, sensors (temperature sensors, vacuum gauges), mechanical vibrations and inductive heating of (few) magnetic components from the magnetic field can be seen as negligible:

$$\sum \dot{W}_{\mathrm{t}} = \dot{W}_{\mathrm{VCL}} + \dot{W}_{\mathrm{level\,probe}} + \underbrace{\dot{W}_{\mathrm{throughput}} + \dot{W}_{\mathrm{sensors}} + \dot{W}_{\mathrm{vibr.}} + \dot{W}_{\mathrm{induct.}}}_{\approx 0}. \tag{3.11}$$

3.8.3 Entropy balance ALPHA-g cryostat

The second law of thermodynamics for an open control volume is given with [30, p. 4.6]

$$\frac{\mathrm{d}S^{\mathrm{CV}}}{\mathrm{d}t} = \sum_{i=1}^{nq} \dot{S}_{\mathrm{Q},i} + \sum_{j=1}^{nj} \dot{S}_j^{\mathrm{irr}} + \sum_{k=1}^{nm} \dot{S}_{\mathrm{m},k} \tag{3.12}$$

Here, S^{CV} denotes the entropy of the control volume, $\dot{S}_{\mathrm{Q},i}$ the entropy flow that transports heat Q, $\dot{S}_j^{\mathrm{irr}}$ the produced entropy flow by irreversibility and $\dot{S}_{\mathrm{m},k}$ the entropy flow transported with mass m. For a steady state in the ALPHA-g cryostat, $\mathrm{d}S^{\mathrm{CV}}/\mathrm{d}t = 0$, whereas the positive sum of $\dot{S}_{\mathrm{Q},i}$ and $\dot{S}_j^{\mathrm{irr}}$ must exit the CV with a negative sum of $\dot{S}_{\mathrm{m},k}$:

$$\dot{m}_{\mathrm{out}}\ s_{\mathrm{out}} = \sum_{i=1}^{nq} \dot{S}_{\mathrm{Q},i} + \sum_{j=1}^{nj} \dot{S}_j^{\mathrm{irr}} + \dot{m}_{\mathrm{in}} \cdot s_{\mathrm{in}} \tag{3.13}$$

The helium undergoes a nearly isobaric state change from liquid at the boiling limit, through the wet steam region to superheated gas. The entropy flow of the outgoing mass flow of GHe is higher than the entropy flow of the incoming LHe mass flow. In general, the mass flows have to be adjusted to a level that the resulting $\dot{S}_{\mathrm{m},k}$ are able to maintain a steady state. For a stationary mass balance as in Equation (3.8) with $\dot{m}_{\mathrm{out}} = \dot{m}_{\mathrm{in}} = \dot{m}$, the helium mass flow must be large enough to transport the incoming entropy out of the CV, depending on the corresponding individual mass flow entropies s_{out} and s_{in}.

3.8.4 Maximum allowed 'A' heat in-power regarding LHe vaporisation

The maximum vaporising LHe volume flow is targeted to $\dot{V}_{\mathrm{max}}^{\mathrm{liq}} \approx 20\ \mathrm{L\,h^{-1}}$. It leads to a simple consideration of the total maximum allowed 'A' heat in-flow. In the following section, when speaking of 'A' heat in-flows, other rates of energy such as the rate of technical work from Equation (3.10) are included as well.

With a LHe density at 4.2 K of $\rho_{\mathrm{liq}} = 125\ \mathrm{kg\,m^{-3}}$ [22, p. 43], the maximum evaporated LHe mass flow of

$$\dot{m}_{\mathrm{max}} = \dot{V}_{\mathrm{max}}^{\mathrm{liq}}\ \rho_{\mathrm{liq}} = 20\ \frac{\mathrm{L}}{\mathrm{h}} \cdot 125\ \frac{\mathrm{kg}}{\mathrm{m^3}} = 2.5 \frac{\mathrm{kg}}{\mathrm{h}} \approx 0.694\ \frac{\mathrm{g}}{\mathrm{s}} \tag{3.14}$$

results in a total maximum allowed 'A' heat in-flow into shell 'c' of

$$\dot{Q}_{\mathrm{c\,tot\,A\,max}} = \dot{m}_{\mathrm{max}}\ \Delta h^{\mathrm{v}} = 0.694\ \frac{\mathrm{g}}{\mathrm{s}} \cdot 20.72 \frac{\mathrm{J}}{\mathrm{g}} = 14.38\ \mathrm{W}. \tag{3.15}$$

Or, to express the result in a different way, the evaporated volume flow of LHe per 'A' heat in-flow Watt is given with

$$\dot{V}^{\text{liq}}_{\text{per W}} = \frac{\dot{Q}}{\rho_{\text{liq}}\,\Delta h^{\text{v}}} = \frac{1\,\text{W}}{125\,\text{kg}\,\text{m}^{-3} \cdot 20.72\,\text{J}\,\text{g}^{-1}} = 3.86 \cdot 10^{-4}\frac{\text{L}}{\text{s}} = 1.39\frac{\text{L}}{\text{h}} \tag{3.16}$$

With $\dot{V}^{\text{liq}}_{\text{max}} \approx 20\,\text{L}\,\text{h}^{-1}$, the total 'A' heat-in flow must be lower than 14.4 W. This is an extraordinarily low value. It emphases the importance of an appropriate thermal insulation of the cryostat. The values will be used to evaluate the results and their order of magnitude in chapter 4.

3.8.5 Power balance of the radiation shields

The GHe enters the shield tubes at about boiling temperature of 4.2 K and exits at about 50 K. The corresponding enthalpies at norm pressure according to NIST [12, p. 43] are $h^{\text{g}}_{4\,\text{K}}(p_{\text{n}}, T = 4.2\,\text{K}) = 30.7\,\text{kJ}\,\text{kg}^{-1}$ and $h^{\text{g}}_{50\,\text{K}}(p_{\text{n}}, T = 50\,\text{K}) = 275.0\,\text{kJ}\,\text{kg}^{-1}$. The resulting difference of enthalpy is $\Delta h^{\text{g}}_{4\,\text{K}\rightarrow 50\,\text{K}} = h_{\text{out}} - h_{\text{in}} = 244.3\,\text{kJ}\,\text{kg}^{-1}$.

Using $\Delta h^{\text{g}}_{4\,\text{K}\rightarrow 50\,\text{K}}$, the minimum GHe mass flow per incoming Watt is given with

$$\dot{m}^{\text{g}}_{\text{per W}} = \frac{\dot{Q}_{\text{shield}}}{\Delta h^{\text{g}}_{4\,\text{K}\rightarrow 50\,\text{K}}} = \frac{1\,\text{W}}{244.3\,\frac{\text{kJ}}{\text{kg}}} \approx 4.09 \cdot 10^{-3}\,\frac{\text{g}}{\text{s}} = 0.0147\,\frac{\text{kg}}{\text{h}}, \tag{3.17}$$

which corresponds to a liquid volume flow of

$$\dot{V}^{\text{liq}}_{\text{per W}} = \frac{\dot{m}^{\text{g}}_{1\,\text{W}}}{\rho_{\text{liq}}} = \frac{4.09 \cdot 10^{-6}\,\frac{\text{kg}}{\text{s}}}{125\,\frac{\text{kg}}{\text{m}^3}} \approx 3.28 \cdot 10^{-8}\,\frac{\text{m}^3}{\text{s}} = 0.118\,\frac{\text{L}}{\text{h}}. \tag{3.18}$$

The value of $0.118\,\text{L}\,\text{h}^{-1}$ LHe per incoming watt will be compared to the determined results in chapter 4. It will then be possible to estimate whether the available cooling gas is sufficient enough or whether a problem of GHe availability could arise that would require additional LHe boil off with heaters located inside the liquid. Finally, chapter 4.7 will discuss an optimal radiation shield temperature depending on the result of Equation (3.18).

3.9 Multi-layer insulation foils in the ALPHA-g cryostat

The ALPHA-g cryostat uses two sets of MLI inside the OVC. One set of 30 layers between the OVC box and the copper shield and one set of 20 layers between the copper shield and the helium space. The layers are 6 µm thin polyester foils (Mylar®) with both faces aluminized provided by the company Hutchinson®. The coating is only 40 nm thick and has a total hemispherical emissive coefficient of 0.043 at 20 °C (see Table A.1). This value corresponds well with the measured emissivity of 0.044 at room temperature of aluminized Mylar® by Domen from NIST in [31].

Figure 3.5. Multi-layer insulation foils of the ALPHA-g cryostat with 30 layers produced by HUTCHINSON®.

3.10 Critical conditions

Table 3.4 presents possible critical conditions of the ALPHA-g cryostat with the respective cause, result and avoiding strategy. They occur either due to thermal issues or affect the thermal efficiency of the system.

Table 3.4. Possible critical conditions of the ALPHA-g cryostat, section 1.

Problem	Cause	Possible result	Avoiding strategy
Sudden rise of OVC pressure	Leak from air to OVC or He-space to OVC opened up	Conductive heat flow of vacuum gas increases, vaporisation of LHe increases	Keep elastomer seals > 0 °C
Over pressurise He-space	Increasing vaporisation of LHe due to increasing 'A' heat-in flow, recovery pressure increases, recovery line blocked	Leak from He-space to OVC opens up, burst of components	Open bypass valve on recovery manifold
TAOs on recovery	Large temperature gradient along pipe, strong heat flow into pipe	He-space pressure increases, additional heat loads into He-space, damage of components due to pressure oscillations	Appropriate thermal insulation, adjust pipe diameter
Overfill of LHe	Wrong liquid level measurement, uncontrolled transfer	Temperature distribution of He-space and VCL changes	Ensure precise liquid level measurement, implement safety valve in transfer system
Lack of LHe	Transfer stopped: transfer line or stinger blocked, Dewar empty	Warm up of power supply or magnet	Ensure minimum Dewar volume
Blockage of the recovery line	Valves blocked, ice formation	Over pressurise He-space	Electrical NO safety valve, use large inner diameter of gas line
Blockage of VCL gas system	Valves defect, ice formation	Temperature and resistance of the VCL increases, magnet power supply breakdown	Run tests to prove gas flow in each single tubing, vent with N_2 instead of air to avoid moisture

Table 3.5. Possible critical conditions of the ALPHA-g cryostat, section 2.

Problem	**Cause**	**Possible result**	**Avoiding strategy**
Blockage of shield gas system	Valves defect, ice formation	Shield temperature increases	Run tests to prove gas flow in each single tubing, vent with N_2 instead of air to avoid moisture
Freezing of HTS plate	HTS plate heaters defect, $\dot{m}_{\mathrm{rec}}$ too high	Elastomers seals freeze and open up leaks from air to OVC and He-space to air	Use strong HTS plate heaters, implement regulating system for heaters

4 Results of thermal study

This chapter studies the thermal condition inside the ALPHA-g cryostat. It is split into three main processes that are considered as independent of each other: heat transfer in vacuum, heat transfer through multi-layer insulation foils and heat transfer in solid components. The results show a possible thermal weak point in the chimneys which will be further investigated in chapter 4.6. The structure of the individual systems and components can be seen in Figure 3.1 on p.16.

4.1 Heat conduction in vacuum

As discussed in chapter 2.2, the heat conduction in gases has no pressure dependence in the range norm pressure. For lower pressure in the range of vacuums, the thermal conductivity k of gases drops to values several orders of magnitude lower than at norm pressure. However, this can still cause a relevant amount of heat load into a thermodynamic system. An assumption of no conductive heat flow through the residual gas inside the OVC might not be justified in principle.

4.1.1 Estimation of the OVC pressure

A main goal of the ALPHA-g cryostat is to keep the OVC pressure as low as possible. It has a linear influence on the free-molecular gas conduction according to equation (2.16). In tests in 2020 and 2021, the OVC pressure went below 10^{-5} mbar in warm state. During the cool down, the surfaces of the He-space become cold. As the OVC is filled with air or N_2 from former venting procedures, the rest gas condensates on the surfaces and the pressure drops. This effect is called cryo-pumping. According to ISO 3529/1–3, "a cryopump is defined as a vacuum pump which captures the gas by surfaces cooled to temperatures below 120 K." [32, p. 242].

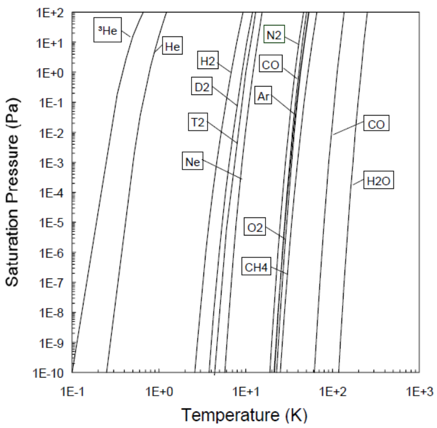

Figure 4.1: Saturation curves of common gases [32, p. 243].

The saturation curves in Figure 4.1 shows that "the 4 K level is sufficient to condense the hydrogen isotopes and neon. By further reduction of the temperature, the ultra-high vacuum range is fully accessible." [32, p. 243]. This corresponds well with the OVC pressure of $3 \cdot 10^{-7}$ mbar during a cold test in April 2021 (no steady state reached).

However, major leaks and outgassing increase the pressure, dependent on the throughput of the vacuum pumping system, resp. the turbo pump. Therefore, a conservative value of 10^{-5} mbar will be used to calculate the heat conduction in vacuum in the ALPHA-g cryostat.

Leaks can either occur from air to OVC or from He-space to OVC. Leaks from air to OVC mainly add N_2 and O_2 into the vacuum. These gases condensate on the cold surfaces and do not increase the pressure until the cold surfaces are saturated. In case of leaks of the second type, from He-space to OVC, the OVC gas mixture changes: The vacuum fills with He as the evaporated LHe escapes the He-space into the OVC. An unknown composition of the OVC gas is the result. He gas cannot condensate on the cold surfaces and increases the pressure directly.

The seals from air to OVC are all elastomer seals that usually work reliable at room temperature (see also [2]). Some of the evaporated LHe inside the cryostat exits the apparatus through a service tube into the recovery system. As this gas is still < 0 °C, cold tests in 2020/2021 showed a major problem: The HTS plate and its seals around the recovery system had frozen. The seals do not ensure a leak tight air to OVC connection anymore. To reduce this problem, a new top plate with strong heaters inside the plate had been implemented to ensure a temperature of the HTS plate > 0 °C.

Seals from He-space to OVC are much more fragile and susceptible. Many ConFlat (CF), Helicoflex® and Swagelok® seals are implemented. Leak checks in the past had highlighted that these seals can fail, although much care was taken in the assembly process [2]. One can assume that the final assembly will also contain little leaks from He-space to OVC (e.g. 10^{-9} mbar L s^{-1}).

It is necessary to mention that the measured pressure on the vacuum gauges does not equal the pressure relevant for vacuum heat transfer. Several factors would have to be considered to estimate a more detailed value for the pressure. On the one hand, the position of the vacuum gauge has an influence on the pressure measurement. In warm state, a gauge close to the turbo pump might read out a lower pressure than a gauge far away. On the other hand, the cryo cooling may create low temperature zones close to the cold surfaces. Because of the intricate apparatus geometry and the non-continuum-type gas, the different pressures do not balance entirely. Furthermore, the molecules trapped in the MLI have little options to escape. Venting holes inside the foils and pumping for a long period of time reduces this factor.

4.1.2 Determination of the Knudsen number

It is required to know the method of calculation described in section 2.2 to calculate the heat flux inside the vacuum. Due to the uncertainty of the representative physical length δ, the Knudsen number in Equation (2.11) is imprecise. The viscosity of nitrogen (N_2) at 300 K $\mu_{\mathrm{N2}}(T = 300\ \mathrm{K})$ is 17.9 µPa s (18.5 µPa s for air) [33]. For a pressure of $p = 10^{-5}$ mbar the mean free path l_{gas} in the annular space according to equation (2.15) is

$$l_{\mathrm{N2}} = \frac{17.9 \cdot 10^{-6}\ \mathrm{Pa\ s}}{10^{-5} \cdot 100\ \mathrm{Pa}} \cdot \sqrt{\frac{\pi \cdot 296.8\ \mathrm{J\ kg^{-1}\ K^{-1}} \cdot 300\ \mathrm{K}}{2\ \mathrm{kg\ m\ N^{-1}\ s^{-2}}}} \approx 6.69\ \mathrm{m}. \tag{4.1}$$

The gas volume in between the MLI can be seen as a very thin and long cuboid with a representative physical length $\delta = 4\ V\ A^{-1}$, where x and y are the short side lengths and z is the long side length. With $V = x\ y\ z$ and $A \approx 2\ x\ z$, the representative physical length is $\delta = 2\ y$ (rather than just y). The MLI in between the OVC box and the copper shields has 30 layers with 6 µm thickness and an estimated thickness of 15 mm if loose. The Knudsen number according to equation (2.11) may be determined with $\delta \approx 2 \cdot 0.5\ \mathrm{mm} = 1\ \mathrm{mm}$ and clearly indicates a free-molecular state:

$$Kn = \frac{6.69\ \mathrm{m}}{0.001\ \mathrm{m}} \gg 1. \tag{4.2}$$

4.1.3 Determination of heat conduction in vacuum

A reference pressure of 10^{-5} mbar will be used to demonstrate the results. The gas-conducting heat flux $\dot{q}_{\mathrm{gas\ cond\ ab}}$ in Equation (2.16) from the OVC box to the copper shields will first be determined without considering MLI. With K according to Equation (2.17)

$$K = \frac{1.40 + 1}{1.40 - 1} \cdot \sqrt{\frac{1\ \mathrm{kg\ m\ N^{-1}\ s^{-2}} \cdot 296.8\ \mathrm{J\ kg^{-1}K^{-1}}}{8 \cdot \pi \cdot 300\ \mathrm{K}}} \approx 1.19 \frac{\mathrm{m}}{\mathrm{s\ K}}, \tag{4.3}$$

it is given with

$$\dot{q}_{\mathrm{gas\ cond\ ab}} = \frac{1.19\ \mathrm{m\ s^{-1}\ K^{-1}}}{\frac{1}{0.8} + \left(\frac{1}{1.0} - 1\right)} \cdot 10^{-5} \cdot 100\ \mathrm{Pa} \cdot (300 - 50)\ \mathrm{K} \approx 0.238 \frac{\mathrm{W}}{\mathrm{m^2}}. \tag{4.4}$$

The accommodation coefficients are $\psi_{\mathrm{a}}(T_{\mathrm{a}} = 300\ \mathrm{K}) = 0.8$, $\psi_{\mathrm{b}}(T_{\mathrm{b}} = 50\ \mathrm{K}) = 1.0$ [17, p. 1354] and $A_{\mathrm{a}}/A_{\mathrm{b}} \approx 1$. In comparison, the heat flux from the copper shields to the He-space is $\dot{q}_{\mathrm{bc}} = 0.134\ \mathrm{W\ m^{-2}}$ with $K(T_{\mathrm{b}}) = 2.92\ \mathrm{m\ s^{-1}\ K^{-1}}$ and $\psi_{\mathrm{b}}(T_{\mathrm{b}}) = \psi_{\mathrm{c}}(T_{\mathrm{c}} = 50\ \mathrm{K}) = 1.0$. As discussed in section 4.1.1, the gas mixture in the vacuum depends on the leak rate from air to OVC and He-space to OVC. In case of a gas mixture of mainly helium, the heat flux changes to $\dot{q}_{\mathrm{ab}} = 0.119\ \mathrm{W\ m^{-2}}$ and $\dot{q}_{\mathrm{bc}} = 0.093\ \mathrm{W\ m^{-2}}$. Here, the accommodation coefficients of helium from Table 2.1 (linearly interpolated for missing values) and the same residual pressure are used.

However, as the number of MLI layers n has a crucial effect on the residual gas conduction, this result should only be used to understand the impact of the MLI. Considering MLI, the remaining molecules transfer heat from shell a to the first MLI layer. Following, the molecules in between the first and second MLI layer will transfer heat to the second layer and so on. In general, the more foils there are between the hot and cold wall, the lower becomes the temperature difference that thrives the process. Additionally, an accommodation coefficient of < 1 further decreases the heat flow. Due to the low thickness of the Mylar of 6 µm, equal temperatures will be assumed on both surfaces.

The temperature for the determination of K can now be reduced to a mean MLI temperature by Equation (2.30) to $T_{\mathrm{m}} = (T_{\mathrm{h}} - T_{\mathrm{c}})/2$. This leads to $T_{\mathrm{m,ab}} = 175\ \mathrm{K}$ with $K_{\mathrm{m,ab}} \approx 1.56\ \mathrm{m\ s^{-1}\ K^{-1}}$ and $T_{\mathrm{m,bc}} = 23\ \mathrm{K}$ with $K_{\mathrm{m,bc}} \approx 4.30\ \mathrm{m\ s^{-1}\ K^{-1}}$. Assuming a corresponding linear MLI temperature drop, $\dot{q}_{\mathrm{gas\ cond\ ab}}$ is reduced similar to the heat radiation in Equation (2.26):

$$\dot{q}_{\mathrm{gas\ cond\ MLI\ ab}} = \frac{K_{\mathrm{m}}\, p\, (T_{\mathrm{a}} - T_{\mathrm{b}})}{\frac{1}{\psi_{\mathrm{a}}} + \frac{1}{\psi_{\mathrm{b}}} - 1 + n\left(\frac{2}{\psi_{\mathrm{MLI}}} - 1\right)}. \tag{4.5}$$

With $\psi_{\mathrm{MLI,ab}} \approx (\psi_{\mathrm{a}} + \psi_{\mathrm{b}})/2 = 0.9$, $\psi_{\mathrm{MLI,bc}} \approx (\psi_{\mathrm{b}} + \psi_{\mathrm{c}})/2 = 1.0$, $n_{\mathrm{ab}} = 28$ and $n_{\mathrm{bc}} = 18$, $\dot{q}_{\mathrm{gas\ cond\ MLI\ ab}}$ and $\dot{q}_{\mathrm{gas\ cond\ MLI\ bc}}$ would both decrease to about $0.010\ \mathrm{W\ m^{-2}}$ for nitrogen.

Table 4.1. Results of heat conduction in vacuum for nitrogen.

p in mbar	Kn	$\dot{q}_{\text{gas cond ab}}$ in W m^{-2}	$\dot{q}_{\text{gas cond MLI ab}}$ in W m^{-2}	$\dot{Q}_{\text{gas cond MLI ab}}$ in W	$\dot{q}_{\text{gas cond bc}}$ in W m^{-2}	$\dot{q}_{\text{gas cond MLI bc}}$ in W m^{-2}	$\dot{Q}_{\text{gas cond MLI bc}}$ in W
10^{-4}	≈ 7	2.38	0.10	0.74	1.34	0.10	0.68
10^{-5}	≈ 7	$2.38 \cdot 10^{-1}$	$1.0 \cdot 10^{-2}$	$7.4 \cdot 10^{-2}$	$1.34 \cdot 10^{-1}$	$1.0 \cdot 10^{-2}$	$6.8 \cdot 10^{-2}$
10^{-6}	≈ 7	$2.38 \cdot 10^{-2}$	$1.0 \cdot 10^{-3}$	$7.4 \cdot 10^{-3}$	$1.34 \cdot 10^{-2}$	$1.0 \cdot 10^{-3}$	$6.8 \cdot 10^{-3}$
10^{-7}	≈ 7	$2.38 \cdot 10^{-3}$	$1.0 \cdot 10^{-4}$	$7.4 \cdot 10^{-4}$	$1.34 \cdot 10^{-3}$	$1.0 \cdot 10^{-4}$	$6.8 \cdot 10^{-4}$

The critical OVC pressure regarding the heat conduction in vacuum for nitrogen is $p_{\text{crit.}} > 10^{-4}$ mbar, considering a perfect evacuation of the gas within in MLI through the venting holes. “In some cases [$\cdots$], the pressure within the insulation may be two orders of magnitude higher than the pressure outside the insulation.” [7, p. 37].

The presented heat fluxes $\dot{q}_{\text{gas cond MLI ab}}$ and $\dot{q}_{\text{gas cond MLI bc}}$ lead to $\dot{Q}_{\text{gas cond MLI ab}} \approx \dot{Q}_{\text{gas cond MLI bc}} = 0.07$ W. The corresponding surface areas are $A_{\text{b,tot}} = 7.42\ \text{m}^2$ resp. $A_{\text{c,tot}} = 6.83\ \text{m}^2$ according to Table 3.3 on p.25.

4.2 Heat transfer through multi-layer insulation foils

The following chapter will discuss radiative and conductive heat transfer through MLI according to Equation (2.19) on p.7.

4.2.1 Heat radiation

The following section will show the heat flux inside the cryostat due to radiation. Equation (2.25) and (2.26) determine the radiative heat flow for MLI applications with n as number of foil layers. The emissive coefficient of the OVC box and the He-space $\varepsilon_{\text{a}} \approx \varepsilon_{\text{c}}$ is ~ 0.24 and the one of the copper shields ε_{b} is ~ 0.04, see also [15, p. 1188]. In the ALPHA-g cryostat, the space in between the three shells is little in most places. In some areas, the MLI is touching a surrounding shell. At the contact points, the foil temperature equals the shell temperature. The polyester foils have a low thermal conductivity with $0.155\ \text{W m}^{-1}\ \text{K}^{-1}$ [34] at room temperature and therefore not a uniform temperature perpendicular to the radiation direction. In the following results it is still assumed that due to the contact areas the 2 outer MLI foils have an evenly temperature equal to the corresponding shell. As a result, n in Equation (2.25) and (2.26) is replaced by $n - 2$. In this conservative model, the radiative heat flow is transferred from the outermost MLI foil with the corresponding shell temperature to the other outermost MLI foil with the other corresponding shell temperature. All emissive coefficients are equal in this model and Equation (2.25) applies.

4.2.1.1 Heat radiation from the OVC shell to the copper radiation shields

The emissive coefficient of the HUTCHINSON MLI at 300 K is $\varepsilon = 0.043$ (see appendix Table A.1). The temperature dependence $\varepsilon = f(T)$ will be discussed more detailed in section 4.2.2.2. Assuming $\varepsilon \neq f(T)$ and equal surface areas sizes of all MLI layers, the heat flux may be determined according to Equation (2.25) to

$$\dot{q}_{\mathrm{rad\ ab}} = \frac{5.6704 \cdot 10^{-8}\ \mathrm{W\,m^{-2}\,K^{-4}} \cdot (300^4 - 50^4)\ \mathrm{K}^4}{\left(\frac{2}{0.043} - 1\right)(1 + 30 - 2)} \approx 0.348 \frac{\mathrm{W}}{\mathrm{m}^2}. \quad (4.6)$$

This leads to $\dot{Q}_{\mathrm{rad\ ab}} \approx 2.742$ W, considering a surface area size of $A_{\mathrm{a,tot}} = 7.88\ \mathrm{m}^2$.

4.2.1.2 Heat radiation from the copper shields to the He-space

There are only 20 layers placed between the copper shield and the inner layer at 4.2 K. The emissive coefficient 50 K is about $\varepsilon = 0.020 \neq f(T)$. The resulting heat flux due to radiation from shell 'b' to 'c' with equal surface areas sizes of all MLI layers is

$$\dot{q}_{\mathrm{rad\ bc}} = \frac{5.6704 \cdot 10^{-8}\ \mathrm{W\,m^{-2}\,K^{-4}} \cdot (50^4 - 4.2^4)\ \mathrm{K}^4}{\left(\frac{2}{0.020} - 1\right)(1 + 20 - 2)} \approx 1.88 \cdot 10^{-4} \frac{\mathrm{W}}{\mathrm{m}^2}. \quad (4.7)$$

This leads to $\dot{Q}_{\mathrm{rad\ bc}} \approx 0.001$ W, considering a surface area size of $A_{\mathrm{b,tot}} = 7.42\ \mathrm{m}^2$. The low value encourages a check of the radiation in case the MLI would be removed completely. The copper shield would then radiate directly onto the He-space. With an emissive coefficient of $\varepsilon_{\mathrm{b}} = 0.04$ and $\varepsilon_{\mathrm{c}} = 0.24$, a heat flux would result of

$$\dot{q}_{\mathrm{rad\ bc\ without\ MLI}} = \frac{5.6704 \cdot 10^{-8}\ \mathrm{W\,m^{-2}\,K^{-4}} \cdot (50^4 - 4.2^4)\ \mathrm{K}^4}{\frac{1}{0.04} + \left(\frac{1}{0.24} - 1\right) \cdot \frac{7.42\ \mathrm{m}^2}{6.83\ \mathrm{m}^2}} \approx 0.012 \frac{\mathrm{W}}{\mathrm{m}^2}. \quad (4.8)$$

This would lead to $\dot{Q}_{\mathrm{rad\ bc\ without\ MLI}} \approx 0.089$ W. Even with strongly conservative values of the emissive coefficients at doubling to $\varepsilon_{\mathrm{b}} = 0.08$ resp. $\varepsilon_{\mathrm{c}} = 0.48$ and a shield temperature of 70 K instead of 50 K, the heat flow would still be acceptable with $\dot{Q}_{\mathrm{rad\ bc\ without\ MLI}} \approx 0.68$ W.

4.2.1.3 Comparison of the specific heat radiation between the shells

The result shows a proportion of the heat radiation discussed above. The specific heat radiation from the outer layer at ambient temperature to the copper shield at 50 K is about

$$\frac{\dot{q}_{\mathrm{rad\ ab}}}{\dot{q}_{\mathrm{rad\ bc}}} = \frac{0.348\ \mathrm{W\,m^{-2}}}{1.88 \cdot 10^{-4}\ \mathrm{W\,m^{-2}}} \approx 1851 \quad (4.9)$$

times higher than the one from the copper shield at 50 K to the inner layer at 4.2 K.

4.2.2 Iterative determination of radiative heat flux through MLI

As discussed, to analyse the heat radiation in the ALPHA-g cryostat, the knowledge of the emissive coefficient of the MLI, as well as the one of all three main layers is necessary. In an easy approximation ε can be seen as temperature independent $\varepsilon \neq f(T)$, which give the results in Equation (4.6) to (4.8). However, to analyse the real heat radiation, ε is a function of temperature.

In this case, only an iterative computation can give a result, in which initial values are required. The following section describes the procedure to determine the heat flux with $\varepsilon = f(T)$. In addition, it compares and analyses the results to the more trivial calculation from section 4.2.1.1 and 4.2.1.2. As Equation (4.7) and (4.9) show negligible results for $\dot{q}_{\mathrm{bc}}$, the iteration will be only carried out to determine $\dot{q}_{\mathrm{ab}}$.

4.2.2.1 Algorithm layout

The script program is written in C++ using Visual Studio 2019. It can be found in the appendix on p.90. The basic layout is defined by global variables and functions. These variables and functions are then called in the main program. Variables are defined as double-type and most of them are arrays of the same variable-type. This includes the MLI temperature, the emissive coefficient, the combined radiation exchange coefficient or the single heat flux in between the layers. In general, the algorithm prints out all arrays during the iteration to give the observer the opportunity to validate the calculations during the loop.

4.2.2.2 Emissive coefficient as function of temperature for HUTCHINSON MLI

First, the function $\varepsilon = f(T)$ must be determined. This is the basis for the iterative result. Literature data about the correlation of emissive coefficient and temperature for aluminised Polyester is discussed in chapter 2.3.1.1, resp. Equation (2.28) and Figure 2.4 to Figure 2.5. Comparing the different data in Figure 4.2, one can recognise a large deviation. Not only do experimental measurements vary, also a mathematical description by Lockheed differs from the given results. One must highlight that the given data from the ALPHA-g MLI provider HUTCHINSON is clearly the most accurate one. However, the company could not provide data for $T < 173.15$ K. As the LHe temperature goes down to 4.2 K, appropriate values must be chosen to proceed with the iteration.

On the one hand, one can definitely say that ε decreases with decreasing T. On the other hand, the exact correlation is unknown. For the computation here, the chosen $\varepsilon = f(T)$ uses a polynomial fit for the given data from HUTCHINSON in Table A.1. For $T < 173.15$ K, a function following the Lockheed equation with a positive shift is used. Because almost all MLI layers have a temperature $T \geq 173.15$ K, $\varepsilon = f(T < 173.15\ \mathrm{K})$ has little influence on the result in any case, as the following chapter will show. The emissive coefficient as function of temperature may be determined by

$$\varepsilon(T) = \begin{cases} 6.8 \cdot 10^{-4} \cdot T^{0.67} + 0.010509, & 4.2 \leq T < 173.15 \\ e(T), & 173.15 \leq T \leq 323.15 \end{cases} \tag{4.10}$$

with $\mathbb{D} = \{T \in \mathbb{Z} : 4.2 \leq T \leq 323.15\}$ and

$$\begin{aligned} e(T) = -1.43772521142286 \cdot 10^{-14} \cdot T^6 + 2.16649135570328 \cdot 10^{-11} \cdot T^5 \\ - 1.34748280488108 \cdot 10^{-8} \cdot T^4 + 4.42384514643472 \\ \cdot 10^{-6} \cdot T^3 - 8.078802135689 \cdot 10^{-4} \cdot T^2 \\ + 0.0778458893311746 \cdot T - 3.0635624272457 \end{aligned} \tag{4.11}$$

In Figure 4.2, $\varepsilon(T)$ is shown as the black dashed line.

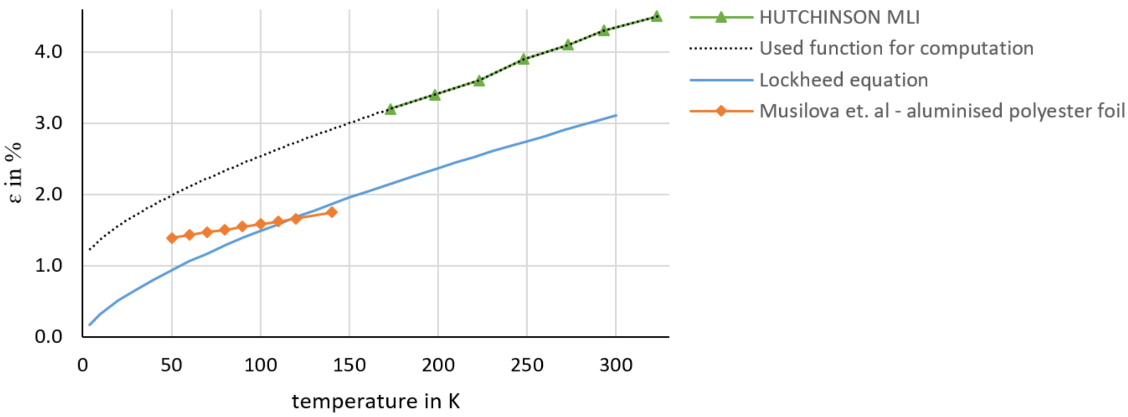

Figure 4.2. Comparison of different data for $\varepsilon = f(T)$ from Equation (2.28) and Figure 2.4.

4.2.2.3 Temperature trend inside the MLI

To calculate a precise result of the radiative heat flux through MLI, each layer emissivity must be known. To obtain these values, the layer temperatures have to be inserted into $\varepsilon = f(T)$.

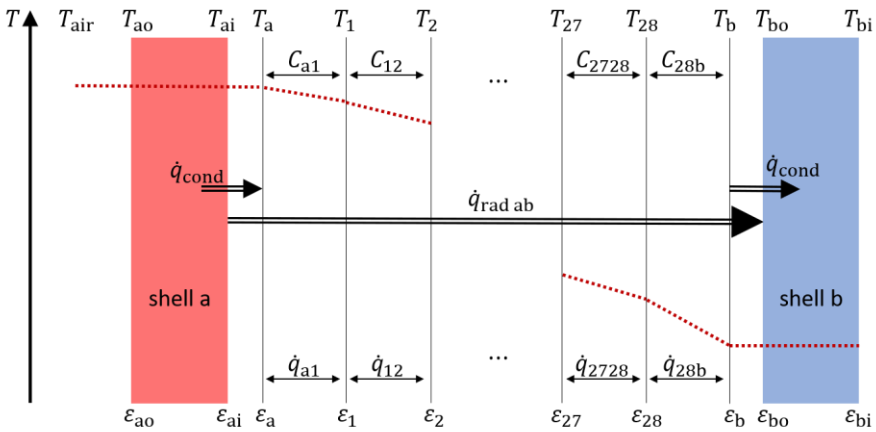

Figure 4.3. Schematic temperature trend in half section view of MLI between shell a and b with corresponding indexes. The illustration shows the boundary conditions as used for the calculations. Free-convective heat transfer, heat conduction in the shell walls and MLI conduction are therefore not shown. The temperature and geometrical dimensions are not true to scale.

A schematic temperature trend inside the MLI is given in Figure 4.3. It is focused on radiation only and shows the boundary conditions as used for the calculations. In reality, the ambient air has a free-convective heat transfer to the outer surface of shell a. Solid conduction inside the wall decreases the temperature further until the inner shell surface radiates to the first MLI layer, which radiates to the next MLI layer, etc. The last MLI layer radiates to the outer shell surface of b and the wall conducts heat to the inner shell surface. Here, the same procedure repeats, since MLI is also located between shell b and c. As highlighted in Equation (3.1) and (3.2) and chapter 4.2.1, three main assumptions are carried out. The differential temperatures of each two shell surfaces and the free-convective heat transfer from air to the outer surface of shell a can be seen as negligible. In addition, it is assumed that the two outermost MLI layers touch the shell surface. This is indicated by $\dot{q}_{\mathrm{cond}}$ in Figure 4.3. Following this, the iteration uses 28 MLI layers with $T_{\mathrm{air}} = T_{\mathrm{ao}} = T_{\mathrm{ai}}$ and $T_{\mathrm{b}} = T_{\mathrm{bo}} = T_{\mathrm{bi}}$. It is indicated by a horizontal temperature trend between the outer shell surface of a and the first MLI resp. the last MLI layer and the inner shell surface of b.

4.2.2.4 Procedure of iteration

The iterative algorithm uses two different methods to determine the MLI layer temperatures. However, the fundamental mathematical equations are the same. Equation (2.25) describes the radiative heat flux through MLI with constant emissive coefficients. The result from shell a to b in Equation (4.6) is used as initial start value of the iteration. Once the iteration has started, a do-while loop guides the number of iteration cycles with a termination condition.

The fundamental approach is the equality of the total radiative heat flux from shell a to shell b $\dot{q}_{\mathrm{rad\ ab}}$ with each single radiative heat flux in between the MLI layers in steady state

$$\dot{q}_{\mathrm{rad\ ab}} = \dot{q}_{\mathrm{a1}} = \dot{q}_{12} = \dot{q}_{23} = \cdots = \dot{q}_{2728} = \dot{q}_{\mathrm{28b}}. \tag{4.12}$$

Method 1: Using Equation (2.20) and (2.25) for the given case

$$\dot{q}_{\mathrm{rad\ ab}} = \dot{q}_{\mathrm{a1}} = \frac{C_{\mathrm{ab}}}{(1+n)} \left({T_{\mathrm{a}}}^4 - {T_{\mathrm{b}}}^4\right) = C_{\mathrm{a1}} \left({T_{\mathrm{a}}}^4 - {T_1}^4\right), \tag{4.13}$$

the MLI temperatures may be determined by

$$T_i = \sqrt[4]{{T_{i-1}}^4 - \frac{\dot{q}_{\mathrm{rad\ ab}}}{C_{(i-1)i}}}. \tag{4.14}$$

The combined radiation exchange coefficient by Equation (2.21) for equal surface areas $A_{(i-1)} = A_i$ is given with

$$C_{(i-1)i} = \frac{\sigma}{\frac{1}{\varepsilon_{(i-1)}} + \frac{1}{\varepsilon_i} - 1}. \tag{4.15}$$

Now, the MLI temperatures are known. The corresponding emissive coefficients can be calculated with Equation (4.10) and the corresponding combined radiation exchange coefficients with Equation (4.29). In the following step, each combined radiation exchange coefficient between the MLI layers is calculated by Equation (2.21) which gives each single heat flux in between each two MLI pairs. As mentioned above in Equation (4.12), these values have to be equal to fulfil a true temperature distribution. However, they deviate due to the actual true MLI temperature, which has yet to be determined. An arithmetic mean value of the heat fluxes can be deduced:

$$\dot{q}_{\mathrm{rad\ arithm.}} = \frac{\sum_{i=1}^{n-1} \dot{q}_{i(i+1)}}{(n-1)}. \tag{4.16}$$

This arithmetic mean value is then returned in the do-while loop and used to calculate more precise MLI temperatures according to Equation (4.14). If the difference of the arithmetic mean value of the heat fluxes $\dot{q}_{\mathrm{rad\ arithm.}}(k)$ in iteration step k to the one in the previous iteration step $\dot{q}_{\mathrm{rad\ arithm.}}(k-1)$ is less than 0.0001 W m^{-2}, the iteration stops.

Method 2: The second iteration method does not return a heat flux that is used to adjust the MLI temperatures. In contrast, formulas for the temperature determination in the following section are used that only contain the combined radiation exchange coefficient resp. the emissive coefficients. At the beginning of the iteration, the MLI layer temperatures are all unknown and a first iteration cycle must be performed with $\varepsilon_{\mathrm{MLI}} = \text{const.}$ which leads to $C_{\mathrm{ab}} = C_{(i-1)i}$. With the fundamental approach from Equation (4.12) and (4.13), the MLI layer temperature for constant emissive coefficients could be deduced with

$$T_i = \sqrt[4]{{T_{i-1}}^4 - \frac{\left({T_\mathrm{a}}^4 - {T_\mathrm{b}}^4\right)}{(1+n)}}. \tag{4.17}$$

Inserting Equation (4.17) into itself for T_1 and T_2 gave the general formula

$$T_i = \sqrt[4]{\frac{{T_\mathrm{a}}^4\,(n+1-i) + {T_\mathrm{b}}^4\,i}{n+1}}. \tag{4.18}$$

As the MLI temperatures are known now, the corresponding emissive coefficients can be calculated with Equation (4.10) and the corresponding combined radiation exchange coefficients with Equation (4.29). Following Equation (4.13) and (4.16), an arithmetic mean value of all single heat fluxes is used to guide the termination condition of the do-while loop. Subsequent to the computation of $\dot{q}_{\mathrm{rad\ arithm.}}$, the emissive coefficients are no longer constant and the simple Equation (4.18) is no longer valid. The MLI temperatures could be calculated for $\varepsilon = f(T)$ with

$$T_i = \sqrt[4]{\frac{1}{n+1}\,\left({T_\mathrm{a}}^4\,a_i + {T_\mathrm{b}}^4\,b_i\right)}. \tag{4.19}$$

The coefficients a_i and b_i could be determined by

$$a_i = (n+1) - \sum_{k=0}^{i} \frac{C_{\mathrm{ab}}}{C_{(i-1)i}} \tag{4.20}$$

and

$$b_i = \sum_{k=0}^{i} \frac{C_{\mathrm{ab}}}{C_{(i-1)i}}. \tag{4.21}$$

The iterative calculation now adjusts the $\varepsilon = f(T)$ again with its corresponding $C = f(T)$ and returns the combined radiation exchange coefficients to determine new coefficients of a_i and b_i for T_i.

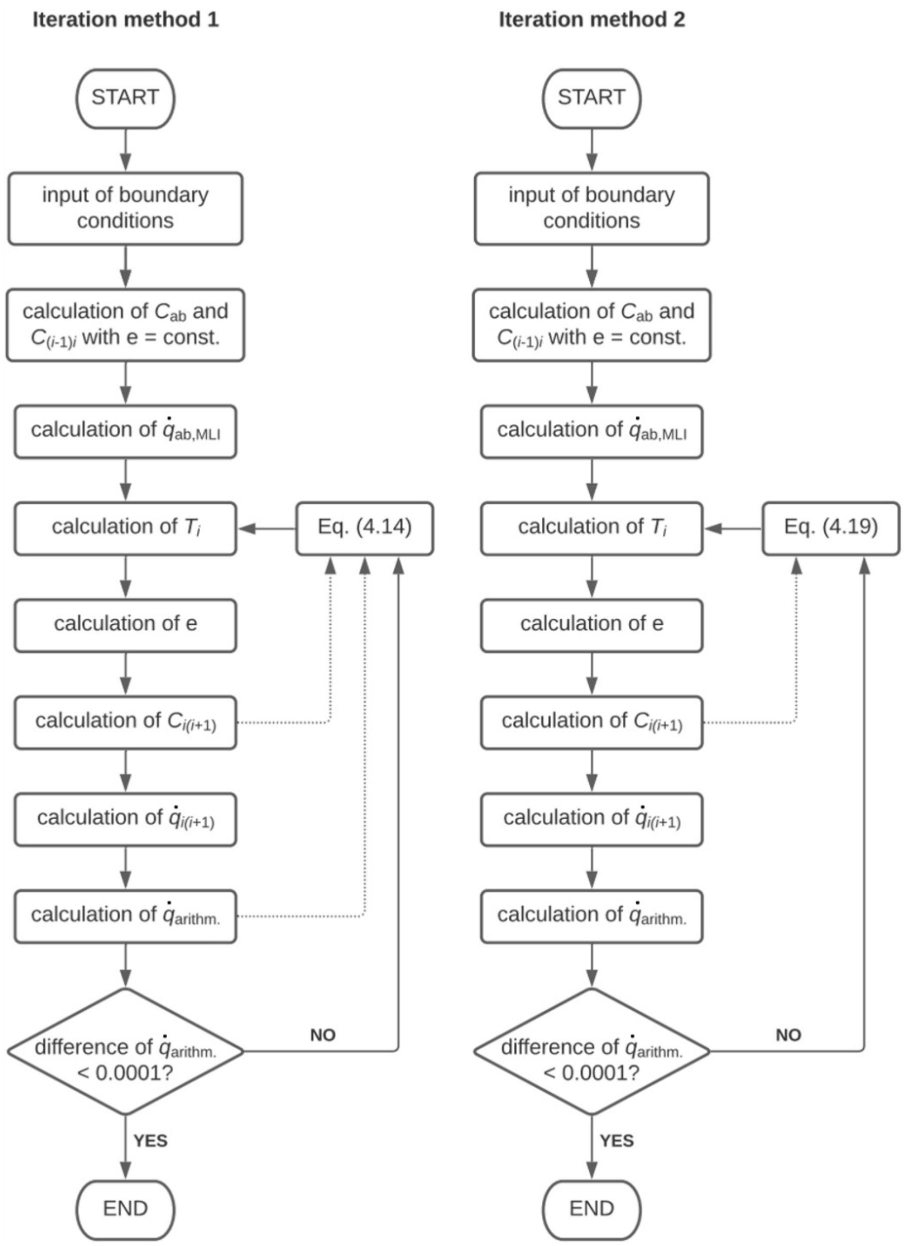

Figure 4.4. Flow chart of the iterative C++ script of prorgam for method 1 (left) and method 2 (right). Solid arrows indicate the algorithm calculation order. Dashed arrows indicate return values of the iteration.

4.2.2.5 Results and analysis of iteration

The most relevant result of the iteration is the actual radiative heat flux from shell a to shell b. Iteration method 1 determines $\dot{q}_{\text{rad ab,iter 1}} \approx 0.305\ \text{W m}^{-2}$, which leads to $\dot{Q}_{\text{rad ab}} = 2.40\ \text{W}$ with $A_{\text{a,tot}} = 7.88\ \text{m}^2$. This reduced the radiative heat transfer relative to $\dot{q}_{\text{rad ab}}$ in Equation (4.6) by

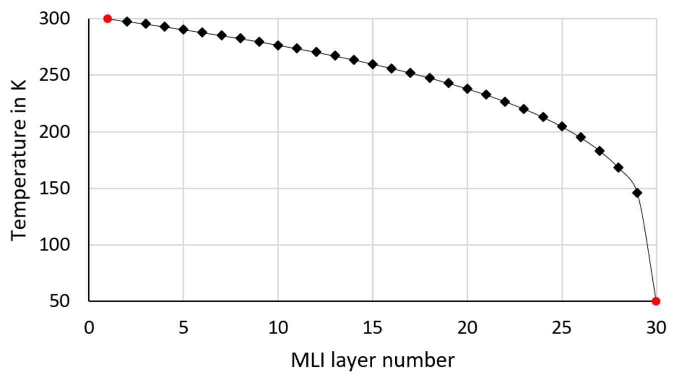

Figure 4.5. MLI temperature distribution calculated by iteration method 1.

$$\frac{\dot{q}_{\mathrm{rad\,ab}} - \dot{q}_{\mathrm{rad\,ab,iter\,1}}}{\dot{q}_{\mathrm{rad\,ab}}} = \frac{0.348\ \mathrm{W\,m^{-2}} - 0.305\ \mathrm{W\,m^{-2}}}{0.348\ \mathrm{W\,m^{-2}}} \approx 12.2\ \%. \tag{4.22}$$

Figure 4.5 shows the MLI temperature distribution due to radiation. The two red markers at position 0 and 29 of the MLI layer number indicate shell ‘a’ and ‘b’. In between there are 28 MLI layers, labelled from 1 to 28.

The temperature distribution follows the radiation law in Equation (2.20) proportional to T^4: The first MLI layers adjacent to shell ‘a’ have temperatures close to the shell temperature of 300 K, while the ones adjacent to shell ‘b’ behave differently. There is a distinctly larger temperature drop at the last MLI layers compared to the first. Comparing the MLI temperature with 175 K, the averaged shell temperature of ‘a’ and ‘b’, one can see that the mean MLI temperature is significantly higher. Only two MLI layers are colder than 175 K, while the remaining 26 are warmer. This leads to an arithmetic mean MLI temperature of 248 K. As a result, the influence of $\varepsilon(T < 173.15\ \mathrm{K})$ is low with respect to $\varepsilon(T \geq 173.15\ \mathrm{K})$. The missing data about the HUTCHINSON MLI emissive coefficient for $T < 173.15$ K can therefore be seen as uncritical.

During the development of the C++ script of program, one main problem has occurred that downgraded the results at first. The last temperature of the loop T_{28} was too high. The indicator for a true MLI temperature distribution is the difference of the maximum and minimum single radiative heat flux in between the MLI layers:

$$\Delta\dot{q}_{\mathrm{rad}\ i(i+1)} = \dot{q}_{\mathrm{rad}\ i(i+1),\mathrm{max}} - \dot{q}_{\mathrm{rad}\ i(i+1),\mathrm{min}}. \tag{4.23}$$

As mentioned above in Equation (4.12) and Figure 4.3, each $\dot{q}_{\mathrm{rad}\ i(i+1)}$ has to be equal in steady state. Whether this is true or not and in what order of magnitude $\Delta\dot{q}_{\mathrm{rad}\ i(i+1)}$ corresponds to, serves as an evaluation of the iteration to determine the utility of the results. It was found that the return value in the do-while loop is essential and different approaches were made. At first, the return value was $\varepsilon_{\mathrm{arithm.}}$, which was used to determine $\dot{q}_{\mathrm{rad\,ab}}$ by Equation (2.25). This resulted in all $\dot{q}_{\mathrm{rad}\ i(i+1)}$ being equal, except the last temperature of the loop, independent whether the iteration solved T_i from the hot to the cold or from cold to the hot surface. With $\Delta\dot{q}_{\mathrm{rad}\ i(i+1)} = 0.110\ \mathrm{W\,m^{-2}}$, a different approach was necessary. Changing the return value to $\dot{q}_{\mathrm{rad\ arithm.}}$ as in the flow chart (Figure 4.4), decreased $\Delta\dot{q}_{\mathrm{rad}\ i(i+1)}$ to only $0.003\ \mathrm{W\,m^{-2}}$. Overwriting all $\dot{q}_{\mathrm{rad}\ i(i+1)}$ with $\dot{q}_{\mathrm{rad\ arithm.}}$ And calculating T_i again, finally led to a negligible value of $\Delta\dot{q}_{\mathrm{rad}\ i(i+1)} \approx 5 \cdot 10^{-5}\ \mathrm{W\,m^{-2}}$.

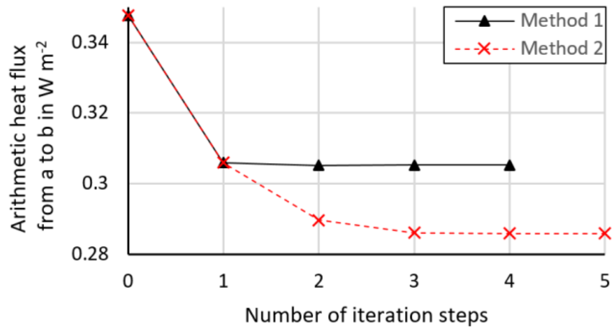

Figure 4.6. Decrease of $\dot{q}_{\text{rad arithm.}}$ over the number of iteration steps for method 1 and method 2

In contrast, method 2 was less successful. The iteration also worked in principle, but the last temperature of the loop was wrong. The deviation of $\dot{q}_{\text{rad 28b}} = 2.167\ \text{W m}^{-2}$ compared to $\dot{q}_{\text{rad arithm.}} = 0.286\ \text{W m}^{-2}$ and $\dot{q}_{\text{rad}\ i(i+1),\text{min}} = 0.219\ \text{W m}^{-2}$ is not utilisable.

Figure 4.6 shows $\dot{q}_{\text{rad arithm.}}$ as function of the number of iteration steps. The heat flux in method 1 converges to almost its final value after the first iteration step already. The one in method 2 matches the one in method 1 after the first iteration step, but continues decreasing relevantly for another 2 steps.

All results of iteration method 1 and 2 are summarised in Table 4.2. The exact MLI temperatures with its corresponding emissive coefficients and $\dot{q}_{\text{rad}\ i(i+1)}$ can be found in appendix Table B.1.

Table 4.2. Summarised results of the iteration method 1 and 2 for heat radiation through MLI.

Physical property	Value for method 1	Value for method 2
$\dot{q}_{\text{rad ab,iter}}$	$0.305\ \text{W m}^{-2}$	$0.286\ \text{W m}^{-2}$
$\dot{Q}_{\text{rad ab,iter}}$ with $A_{\text{a,tot}} = 7.88\ \text{m}^2$	2.40 W	2.25 W
$T_{\text{arithmetic}}$	248.3 K	270.1 K
$\varepsilon_{\text{arithmetic}}$	3.8 %	4.0 %
Reduction of $\dot{q}_{\text{rad ab,iter}}$	12.2 %	17.8 %
$\dot{q}_{\text{rad}\ i(i+1),\text{max}}$	0.305271	2.16718
$\dot{q}_{\text{rad}\ i(i+1),\text{min}}$	0.305217	0.218631
$\Delta\dot{q}_{\text{rad}\ i(i+1)}$	$5 \cdot 10^{-5}\ \text{W m}^{-2}$	$1.949\ \ \text{W m}^{-2}$
Number of total iteration steps	6	5

4.2.2.6 Evaluation of results

Due to the unacceptably high $\Delta\dot{q}_{\text{rad}\ i(i+1)}$ of iteration method 2, the results of this algorithm cannot be used for a thermal study of the ALPHA-cryostat. In contrast, as $\Delta\dot{q}_{\text{rad}\ i(i+1)}$ of iteration method 1 is almost zero. Here, the MLI temperature distribution according to radiation is true and helps understanding the thermal process inside the MLI.

Nevertheless, the influence of a low emissivity at low temperatures has been overestimated before the iteration was carried out. The arithmetic MLI temperature of 248 K according to method 1 results in a reduction of $\dot{q}_{\text{rad ab,iter}}$ relative to $\dot{q}_{\text{rad ab}}$ of 12.2 %. Comparing this decrease to the general uncertainty of the given circumstances, one might argue that the determination of $\dot{q}_{\text{rad ab}}$

with $\varepsilon \neq f(T)$ could be sufficient already. Precise knowledge about $\varepsilon = f(T)$ is inevitable for the applicability of $\dot{q}_{\text{rad ab,iter}}$. For the HUTCHINSON MLI at temperatures below 173.15 K, the accuracy of the results should be evaluated with caution. Furthermore, changes of ε due to crinkling or pollution of MLI might have a bigger influence than what the iterative deviation from the simplified result indicates. Finally, the heat conduction through MLI, which is poorly quantifiable [13], further calls the iterative results into question. MLI radiation and conduction cannot be separated in independent systems for a precise result of the transferred heat flux. It is strongly influenced by the MLI temperature distribution. MLI radiation is $\propto T^4$, while MLI conduction is $\propto T$. Consequent to this, the actual MLI temperature distribution is proportional to T^x with the exponent $1 < x < 4$.

Additionally, one has to mention the assumption of $T_{\text{air}} = T_{\text{ao}} = T_{\text{ai}}$ and $T_{\text{b}} = T_{\text{bo}} = T_{\text{bi}}$ for the iteration described in section 4.2.2.3. If the two outermost MLI layers do not touch the adjacent shell surface in reality, the computation of $\dot{q}_{\text{rad ab}}$ with 28 MLI layers is 6.67 % higher than it would be with 30 MLI layers. This positive deviation applies for $\dot{q}_{\text{rad ab}}$ as well as for $\dot{q}_{\text{rad ab,iter}}$. This would also apply if the heat conduction perpendicular to the direction of radiation is so low, that small contact points have no influence on the average MLI temperature.

The expenditure of time writing and optimising the script of program could be called into question in relation to the results achieved. Following chapters will show a higher relevance of different thermal systems, such as the heat conduction in solid components.

4.2.2.7 Final reflections on the iterative determination of MLI radiation

An approach to specify the MLI temperature distribution with a proportionality of T^χ with the exponent $1 < \chi < 4$ could be done by considering MLI radiation and conduction in two independent systems at first. Once the order of magnitude of both processes is known, one might estimate χ with

$$\chi \approx 4 \cdot \frac{\dot{q}_{\text{rad ab,iter}}}{\dot{q}_{\text{MLI tot}}} + \frac{\dot{q}_{\text{MLI cond ab}}}{\dot{q}_{\text{MLI tot}}}. \tag{4.24}$$

A resulting $\chi < 4$ leads to a lower arithmetic MLI temperature and a bigger influence of $\varepsilon = f(T)$. Therefore $\dot{q}_{\text{MLI rad ab}}$ would be lower considering this process than the radiation independently. The reduction of $\dot{q}_{\text{MLI rad ab,iter}}$ relative to $\dot{q}_{\text{MLI rad ab}}$ would therefore increase and the utility of the C++ script of program would eventually improve.

It is to mention that Equation (4.24) is only a coarse estimation defining the MLI temperature distribution as function of T^χ and has not yet been analytically or empirically been proven.

4.2.3 Heat conduction through MLI

Chapter 2.3.2 discusses the non-negligible influence of heat conduction through superinsulation at cryogenic temperatures. There is no general approach to quantify conductive heat flow through MLI [5, p. 1276]. The presented methods in chapter 2.3.2 will be used to estimate this ratio of the total heat flow.

The MLI layer density has a strong effect on $\dot{q}_{\text{MLI cond}}$ in Equation (2.29). It is crucial using a representative N to determine a realistic conductive heat flow due to its exponent of 2.56. In the

ALPHA-g cryostat N is not constant. In places where the space between the OVC box and copper shield is less than the MLI blanket thickness, the MLI is crushed together. This had been visible during the craning operations in 2021. Especially around the shield tubes, MLI might be squeezed to its minimum possible thickness. On other places, e.g., around the horizontal bellow and horse-shoe, the OVC box is several units of MLI thickness away from the copper shield. Here, the mechanical pressure in Figure 2.8 only comes from evacuation and dead load. A mean N is difficult to estimate, thus, the following calculation will use a minimum and maximum N. For N_{min}, a value of ~15 layers per cm and for N_{max} a value of ~35 layers per cm will be used. According to Figure 2.9, N_{min} would be in the range of the discussed optimum, whereas N_{max} is too dense from a thermal efficiency perspective.

4.2.3.1 Heat conduction through MLI from shell 'a' to 'b'

According to Ross [13] and Equation (2.30), the mean MLI temperature can be estimated with

$$T_{\mathrm{m}} = \frac{300\ \mathrm{K} + 50\ \mathrm{K}}{2} = 175\ \mathrm{K}. \tag{4.25}$$

However, results in chapter 4.2.2.5 respecting radiation independently found a different mean MLI temperature of about 248 K, which more follows a correlation similar to

$$T_{\mathrm{m}} = \sqrt[4]{\frac{T_{\mathrm{a}}{}^4 - T_{\mathrm{b}}{}^4}{2}} = \sqrt[4]{\frac{300^4 - 50^4}{2}\ \mathrm{K}^4} \approx 252\ \mathrm{K}\,. \tag{4.26}$$

As discussed in Equation (4.24), T_{m} would be in between the two suggested solutions: $175\ \mathrm{K} < T_{\mathrm{m}} < 248\ \mathrm{K}$. For $T_{\mathrm{m}} = 175\ \mathrm{K}$ and $N_{\mathrm{min}} = 15$, the conductive heat flux through MLI in compliance with Lockheed [13] in Equation (2.29) would be

$$\begin{aligned}\dot{q}_{\mathrm{MLI\ cond\ ab,min}} &= \frac{8.95 \cdot 10^{-5}\ \mathrm{mW\ m^{-2}\ K^{-2}} \cdot 15^{2.56} \cdot 175\ \mathrm{K}}{28} \cdot (300 - 50)\ \mathrm{K} \\ &\approx 0.143\ \mathrm{W\ m^{-2}},\end{aligned} \tag{4.27}$$

leading to $\dot{Q}_{\mathrm{MLI\ cond\ ab,min}} = 1.13\ \mathrm{W}$ with $A_{\mathrm{a,tot}} = 7.88\ \mathrm{m^2}$. For N_{max}, its results in

$$\begin{aligned}\dot{q}_{\mathrm{MLI\ cond\ ab,max}} &= \frac{8.95 \cdot 10^{-5}\ \mathrm{mW\ m^{-2}\ K^{-2}}\ 35^{2.56} \cdot 175\ \mathrm{K}}{28} \cdot (300 - 50)\ \mathrm{K} \\ &\approx 1.255\ \mathrm{W\ m^{-2}}.\end{aligned} \tag{4.28}$$

This would lead to $\dot{Q}_{\mathrm{MLI\ cond\ ab,max}} \approx 9.89\ \mathrm{W}$. One has to mention that the surface area in which $\dot{q}_{\mathrm{MLI\ cond,max}}$ applies is little compared to the general radiation surface. Considering an arithmetic mean MLI temperature of $T_{\mathrm{m}} = 248\ \mathrm{K}$ in agreement with the radiative C++ iteration, the conductive heat flux would increase to $\dot{q}_{\mathrm{MLI\ cond,min}} \approx 0.203\ \mathrm{W\ m^{-2}}$ or $\dot{q}_{\mathrm{MLI\ cond,max}} \approx 1.778\ \mathrm{W\ m^{-2}}$.

Using Equation (2.31) modelled by Ross [13] as second calculation method, the crucial value is now the spacer conductance k_{o}. For 37-layer double-aluminised Mylar and $T_{\mathrm{m}} > 150\ \mathrm{K}$, a value of $k_{\mathrm{o}} = 25\ \mathrm{mW\ m^{-2}\ K^{-1}}$ and $\kappa(T) \approx 1$ (see Figure 2.8) can be chosen. This results in

$$\dot{q}_{\mathrm{MLI\,cond\,ab}} = 25\,\frac{\mathrm{mW}}{\mathrm{m^2\,K}} \cdot 1 \cdot \frac{300\,\mathrm{K} - 50\,\mathrm{K}}{28} = 0.223\,\frac{\mathrm{W}}{\mathrm{m^2}}, \tag{4.29}$$

which would lead to $\dot{Q}_{\mathrm{MLI\,cond\,ab}} \approx 1.76\,\mathrm{W}$. In k_{o}, crushed MLI is not considered. The results from Equation (4.27) and (4.29) are of similar magnitude, whereas $\dot{q}_{\mathrm{MLI\,cond,max}}$ is about one order of magnitude higher. The two formulas from Lockheed and Ross give a more similar result when considering $T_{\mathrm{m}} = 248\,\mathrm{K}$. It should be noted that the high proportion of $\dot{q}_{\mathrm{MLI\,cond}}$ compared to $\dot{q}_{\mathrm{MLI\,total}}$ changes the temperature distribution inside the MLI. In general, the conductive heat transfer through MLI at the given circumstances is clearly not negligible and needs to be respected in the thermal efficiency study of the ALPHA-g cryostat.

4.2.3.2 Heat conduction through MLI from shell ‘b’ to ‘c’

The conductive heat flux through MLI in compliance with Lockheed in Equation (2.29) is a “fit to near-room-temperature experimental data […] and does not lend itself to changes in […] heat transfer differences at ultra low temperatures.” [13]. For the given temperature range, only the specifically for ultra low temperatures adjusted model by Ross can be used. With $k_{\mathrm{o}} = 25\,\mathrm{mW\,m^{-2}\,K^{-1}}$, $\kappa(T) \approx 9/25 \approx 0.36$ (see Figure 2.8) and $n = 18$, the conductive heat flux through MLI may be determined to

$$\dot{q}_{\mathrm{MLI\,cond\,bc}} = 25\,\frac{\mathrm{mW}}{\mathrm{m^2\,K}} \cdot \frac{9}{25} \cdot \frac{50\,\mathrm{K} - 4\,\mathrm{K}}{18} = 0.023\,\frac{\mathrm{W}}{\mathrm{m^2}}. \tag{4.30}$$

This would lead to $\dot{Q}_{\mathrm{MLI\,cond\,bc}} = 0.17\,\mathrm{W}$ with $A_{\mathrm{b,tot}} = 7.42\,\mathrm{m^2}$. The result shows a much smaller heat flux than between shell ‘a’ and ‘b’. As $\dot{q}_{\mathrm{rad\,bc}} < 10^{-3}\,\mathrm{W\,m^{-2}}$, the heat transfer through MLI from shell ‘b’ to ‘c’ is dominated by conduction, which leads to a linear character of the MLI temperature distribution.

4.2.4 Summary of heat transfer through MLI

The total transferred heat through MLI from shell ‘a’ to ‘b’ leads to $\dot{q}_{\mathrm{MLI\,tot\,ab}} = 0.305\,\mathrm{W\,m^{-2}}$ $+0.223\,\mathrm{W\,m^{-2}} = 0.528\,\mathrm{W\,m^{-2}}$. This considers the iterative result of radiation $\dot{q}_{\mathrm{rad\,ab,iter}}$ and the conductive heat flux $\dot{q}_{\mathrm{MLI\,cond\,ab}}$ according to Ross [13]. The total transferred heat flux through MLI from shell ‘b’ to ‘c’ is fully dominated by MLI conduction and results in $\dot{q}_{\mathrm{MLI\,tot\,bc}} = 0.023\,\mathrm{W\,m^{-2}}$.

Table 4.3. Summarised results of heat transfer through MLI from shell ‘a’ to ‘b’ and shell ‘b’ to ‘c’.

Physical property	$\dot{q}_{\mathrm{rad\,ab}}$	$\dot{q}_{\mathrm{rad\,ab,iter}}$	$\dot{q}_{\mathrm{rad\,bc}}$	T_{arithm} (radiation only)	$\dot{q}_{\mathrm{MLI\,cond\,ab}}$ according to Ross [13]	$\dot{q}_{\mathrm{MLI\,cond\,bc}}$ according to Ross [13]	$\dot{Q}_{\mathrm{MLI\,tot\,ab}}$ with $7.88\,\mathrm{m^2}$	$\dot{Q}_{\mathrm{MLI\,tot\,bc}}$ with $7.42\,\mathrm{m^2}$
Value	0.348	0.305	0.0002	248	0.223	0.023	4.16	0.17
Unit	$\mathrm{W\,m^{-2}}$	$\mathrm{W\,m^{-2}}$	$\mathrm{W\,m^{-2}}$	K	$\mathrm{W\,m^{-2}}$	$\mathrm{W\,m^{-2}}$	W	W

4.3 Heat conduction in solid components

An essential part of heat transfer in the ALPHA-g cryostat is caused by solid heat conduction. Some components have large temperature gradients from ambient temperature to almost evaporation temperature of LHe. In addition, the three main shells, He-space, shield-system and OVC-enclosure, have certain points of contact with each other to bear their mechanical loads and ensure spatial separation. Although these contact areas are minimised and material selection and thickness are adapted to the existing conditions of a thermal efficient apparatus, conductive heat transfer can dominate in cryostats.

The following chapter will discuss this conductive heat transfer in components from OVC-enclosure to He-space directly. Additionally, from OVC-enclosure to the shield-system and from the radiation shield-system to He-space. The majority of the investigation takes place from OVC-enclosure to He-space, with consideration of the chimneys, the service tubes and the cryo-supports. As for all heat loads inside ALPHA-g, a differentiation between 'A' heat-in and 'B' heat-in loads must be carried out.

Heat conduction in solid components is considered in independent systems. GHe located in some of these parts causing gas conduction and possible convection will be discussed in a separate contemplation in chapter 4.4 and 4.6. Finally, a combination of these independent systems will be carried out to represent the real thermodynamic conditions.

4.3.1 Heat conduction in the chimneys

On top of the He-box, there are five pipes connecting the He-box to the HTS plate (see also [2]). Each one of these chimneys contains a flexible bellow in between two pipe sections that allows lateral tolerance in the assembly. The main purpose of the chimneys is to provide a gas chamber for the high-temperature superconducting magnets. These are inserted inside the chimneys and allow a power supply of the superconducting magnets located in the atom trap. The chimneys can be divided into five main sections described in Figure 4.7.

The driving physical parameter of conductive heat transfer through the chimneys is the large temperature drop from about 300 K on the HTS plate to the temperature of the LHe-box ceiling. It is difficult to determine an exact temperature at this position. The GHe has the evaporation temperature of 4.2 K at first and then becomes superheated. A cold test of the ALPHA-g cryostat including the shield-system on 1st and 2nd of July 2021 allow an approximation. There are temperature sensors on the He-box ceiling, but they only read a minimum of 50 K and do not give any further information about the exact temperature (it is < 50 K). However, a temperature sensor on the outside of the flute, located between its He-box connection and the GHe outlet, read out a temperature of about 12 K on the evening of 2nd July 2021 in steady state. One can assume, that the He-box ceiling temperature is therefore 4.2 K $< T <$ 12 K. Data in [35] demonstrates a drop of the thermal conductivity of 304 stainless steel for cryogenic temperatures < 50 K. As k becomes low close to absolute zero, the thermal conductivity integral difference $\Theta_{300\,\mathrm{K}} - \Theta_{12\,\mathrm{K}}$ is only 0.2 % lower than $\Theta_{300\,\mathrm{K}} - \Theta_{4\,\mathrm{K}}$ [35]. For the thermal study carried out in the following chapters, a uniform temperature around the He-box of $T = 4.2$ K will be used as fixed value.

The conductive heat transfer for $k = f(T)$ according to Equation (2.7) on p.4 indicates that a large geometrical factor G results in a large heat flow. It is comparable to the reciprocal of the thermal conductivity and resistivity $k^{-1} \cdot R_{\mathrm{k}}^{-1}$ in Equation (2.5) and (2.6).

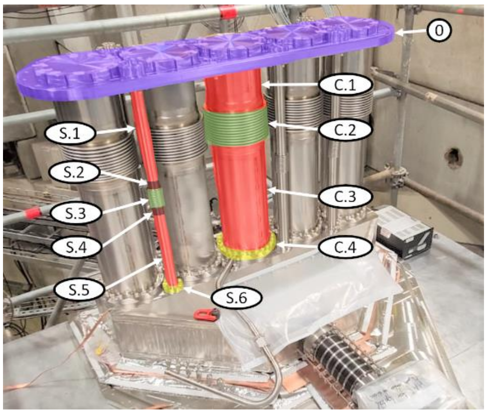

Figure 4.7. Five chimneys and three service tubes placed on the He-box. The picture was taken on 12th Oct 2020. The labelled numbers indicate the following parts with (C.) representing the chimney and (S.) representing the service tube described in chapter 4.3.2: (0) HTS plate, (C.1) upper pipe, (C.2) flexible bellow, (C.3) lower pipe, (C.4) ConFlat flange, (S.1) upper pipe, (S.2) welding connecting upper pipe and flexible bellow, (S.3) flexible bellow, (S.4) welding connecting lower pipe and flexible bellow, (S.5) lower pipe and (S.6) lower flange connecting service tube and He-box. A more detailed technical drawing of a chimney and service tube is shown in appendix Figure C.1 and Figure C.2.

One could see G as a geometrical heat conductivity. For a constant cross-section area A along the direction of flow with the length L, the geometrical factor G by Equation (2.8) is reduced to

$$G = \left(\int_{x_1}^{x_2} \frac{dx}{A(x)} \right)^{-1} = \frac{A}{x_2 - x_1} = \frac{A}{L}. \tag{4.31}$$

As also in the Fourier's law from Equation (2.3), $\dot{Q}_{\text{cond}} \propto A \cdot L^{-1}$.

The following calculations refer to the upper pipe as section '1', the flexible bellow as section '2' and the lower pipe as section '3' as shown in Figure 4.7. The used dimensions are shown in detail in appendix Figure C.1.

The geometry of the chimneys along the axial direction changes significantly around the flexible bellow. Cross-section area and length in section '2' vary from section '1' and '3' and require a calculation caused by the windings. The windings were divided into a straight and curved part. The length of the straight part is given with

$$L_{2,\text{straight}} = 24 \cdot 13.4 \text{ mm} + 2 \cdot 4.2 \text{ mm} = 330 \text{ mm} \tag{4.32}$$

and the length of the curved part is given with

$$L_{2,\text{curved}} = 25 \cdot \frac{\pi \cdot d_{2,\text{curved}}}{2} = 25 \cdot \frac{\pi \cdot 6 \text{ mm}}{2} \approx 234 \text{ mm}. \tag{4.33}$$

The compressed length in section '2' of 151 mm extends to $L_2 = L_{2,\text{straight}} + L_{2,\text{curved}} = 565.6$ mm outstretched length. The physical length through which the conductive heat transfer has to flow is the outstretched length.

Table 4.4. Geometrical properties of the chimneys divided into three sections.

Physical property	Section 1: upper pipe	Section 2: flexible bellow	Section3: lower pipe
A_i	1590 mm^2	421 mm^2	1590 mm^2
L_i	151 mm	566 mm	473 mm
s_i	2.5 mm	0.6 mm	2.5 mm
G_i	10.53 mm	0.7450 mm	3.362 mm
Material type	316L	316L	316L

For the determination of A_2, the wall thickness s is the most relevant factor. The upper and lower pipe have a wall thickness of both 2.5 mm, while the flexible bellow only has 0.6 mm. The cross-section area in the straight section can be obtained with

$$A_{2,\text{straight}} = \pi \cdot d_{2,\text{straight}} \cdot s_2 = \pi \cdot 224\ \text{mm} \cdot 0.6\ \text{mm} = 422\ \text{mm}^2. \tag{4.34}$$

The one of the curved sections can be determined in a more complex consideration to $A_{2,\text{curved}} \approx 421.0\ \text{mm}^2$, which finally results in

$$A_2 = \frac{L_{2,\text{straight}}}{L_2} \cdot A_{2,\text{straight}} + \frac{L_{2,\text{curved}}}{L_2} \cdot A_{2,\text{curved}} = 422\ \text{mm}^2. \tag{4.35}$$

This value is about 3.8 times smaller than $A_1 = A_3 = 1590\ \text{mm}^2$, although section ‘2’ has a larger diameter than section ‘1’ and ‘3’. As a result, the single G_i in Table 4.4 show a high value in section ‘1’ and ‘3’ (10.53 mm and 3.362 mm). In contrast, the value on the flexible bellow in section ‘2’ is much lower (0.745 mm). The bellow illustrates a lager geometrical heat resistivity. Using the single G_i of each section, the geometry factor for one entire chimney is given with

$$G_{\text{chim}} = \left(\int_0^{L_1} \frac{dx}{A_1(x)} + \int_0^{L_2} \frac{dx}{A_2(x)} + \int_0^{L_3} \frac{dx}{A_3(x)} \right)^{-1} = \left(\frac{1}{G_1} + \frac{1}{G_2} + \frac{1}{G_3} \right)^{-1} \approx 0.5765\ \text{mm}. \tag{4.36}$$

Both, the chimney pipes and the flexible bellow are made of 316L stainless steel. The thermal conductivities of 304, 304L and 316 stainless steel are almost identical in the given temperature range [21]. For all following calculations, the values of 316 stainless steel in [35] will be used as thermal conductivity integral Θ for 316L stainless steel.

The conductive heat flow through all five the chimneys can be determined by

$$\begin{aligned} \dot{Q}_{\text{cond chim}} = 5 \cdot G_{\text{chim}} \cdot (\Theta_{300\,\text{K}} - \Theta_{4\,\text{K}}) &= 5 \cdot 5.77 \cdot 10^{-4}\ \text{m} \cdot (3077 - 0.40)\ \text{W m}^{-1} \\ &\approx 5 \cdot 1.77\ \text{W} \approx 8.87\ \text{W}. \end{aligned} \tag{4.37}$$

4.3.2 Heat conduction in the service tubes

The ALPHA-g cryostat has 7 service tubes that connect the He-box to the HTS plate, additionally to the chimneys (see [2]). Three of them, are visible in Figure 4.7 and a technical drawing is shown in appendix Figure C.2. The service tubes allow various functionalities for the He-space,

Table 4.5. Geometrical properties of the service tubes divided into five sections.

Physical property	Section 1	Section 2	Section 3	Section 4	Section 5
A_i	123 mm^2	251 mm^2	38 mm^2	251 mm^2	123 mm^2
L_i	321 mm	15 mm	250 mm	15 mm	321 mm
s_i	1 mm	2 mm	0.25 mm	2 mm	1 mm
G_i	0.3822 mm	16.75 mm	0.1512 mm	16.75 mm	0.3822 mm
Material type	316L	316L	316L	316L	316L

such as sensor connections from the He-box to outside world, LHe level measuring or gas connections for burst disks. They are axial symmetric and have an upper and lower pipe linked via a flexible bellow as also the chimneys. However, instead of a CF flange, the service tubes use a flange with a groove and a Helicoflex® seal on each side (see [2]). The outer diameter of the pipes is 40 mm, with a wall thickness of only 1 mm and 0.25 mm for the bellow. For the calculation, the sections refer to the notation in Figure 4.7 (section '1' refers to the upper pipe, section '2' to the welding part between upper pipe and flexible bellow, section '3' to the flexible bellow, section '4' to the welding part between the lower pipe and the flexible bellow and finally section '5' to the lower pipe).

The outstretched length of the flexible bellow with 12 windings can be determined similar to Equation (4.32) and (4.33) to

$$L_3 = 24 \cdot \left(3.75 + \frac{\pi \cdot (4 + 0.25)}{2}\right) = 250 \text{ mm}. \tag{4.38}$$

The cross-sectional area in section '3' can be deduced using the same procedure as in Equation (4.34) and (4.35) to $A_3 = 37.84 \text{ mm}^2$. The total geometrical factor for the service tubes of

$$G_{\text{serv}} = \left(\frac{2}{G_{12}} + \frac{2}{G_{23}} + \frac{1}{G_{34}}\right)^{-1} \approx 0.08360 \text{ mm} \tag{4.39}$$

leads to the total conductive heat flow of

$$\begin{aligned}\dot{Q}_{\text{cond serv}} &= 7 \cdot G_{\text{serv}} \cdot (\Theta_{300\text{ K}} - \Theta_{4\text{ K}}) = 7 \cdot 8.36 \cdot 10^{-5} \text{ m} \cdot (3077 - 0.40) \text{ W m}^{-1} \\ &\approx 7 \cdot 0.257 \text{ W} \approx 1.80 \text{ W}.\end{aligned} \tag{4.40}$$

4.3.3 Heat conduction in the cryo-supports

Six cryo-supports bear the load of the He-box including the components attached to it (chimneys, service tubes and HTS plate). They have direct contact with the bottom of the He-box, the ambient air and OVC-enclosure at the same time (see also [2]). Therefore, they are important components in terms of thermal efficiency. Heat conduction through the cryo-supports has to be considered as 'A' heat-in flow and can cause direct vaporisation of LHe. To lower the conductive heat transfer, the cryo-supports have a material combination of stainless steel and G-10, "a thermal insulator

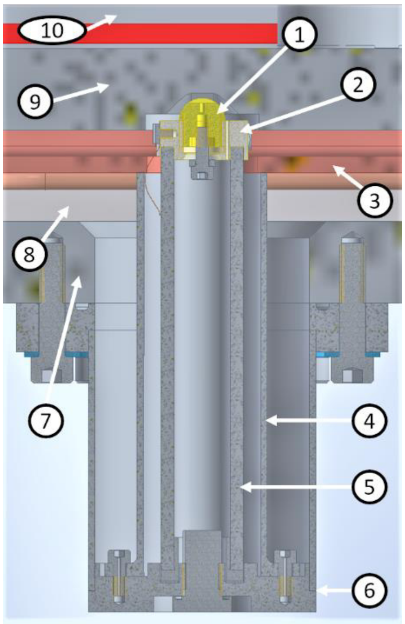

Figure 4.8. CAD Screenshot of a cryo-support assembled on the ALPHA-g cryostat. A more detailed technical drawing can be found in appendix Figure C.3. The labelled numbers indicate the following parts: (1) Levelling screw, (2) connecting piece, (3) copper shield bottom plate, (4) outer G-10 tube, (5) inner G-10 tube, (6) bottom of cryo-support cup, (7) OVC-enclosure bottom plate, (8) OVC, (9) bottom of He-box and (10) inside of He-box containing LHe.

made of epoxy resin and glass fibres" [35, p. 80]. G-10 and G-11 are often used in cryogenic applications, because "[...] their types and material composition, as well as manufacturing processes, cover a wide range of mechanical and thermal properties." [36, p. 380]. Because the material is made of fibreglass cloths, it has directional material properties. Additionally, the thermal conductivity is dependent on the direction of conductive heat transfer. Along the warp direction, k can be ~30 % higher than along the normal direction [37]. The single warps do not have perfect contact with each other and decrease the thermal conductivity. Thermal conductivity integrals of G-10 according to Caltech are given in [38]. Additionally, NIST [37] gives a function for k in warp and normal direction.

A technical drawing of the components can be found in appendix Figure C.3. The G-10 tubes inside the cryo-supports have direct contact with the bottom plate of the copper shield system. Between the He-box and the cryo-support cup is a small assembly of a levelling screw and a connecting piece. In the calculations here, the assumption of a perfect heat transfer between the components is made. The ideal contact from the cryo-support cup to the G-10 tubes, as well as the contact to the upper assembly group and to the He-box leads to equal surface temperatures of the corresponding touching components. The boundary conditions are once more two fixed temperatures. As the levelling screw is touching the He-box and the bottom of the cryo-support cup is exposed to ambient air, a temperature of 4 K resp. 300 K can be assumed. As mentioned above, the ALPHA-g cryostat contains six cryo-supports. For the following calculations it is necessary to mention that the two upstream ones are shorter than the 4 downstream ones.

For the following calculations on the downstream side, the inner G-10 tube is notated as section '1' and the outer G-10 tube as section '2' as presented in Table 4.6. For the upstream side, section '3' labels the outer G-10 tube and '4' the inner one. The 'A' heat-in flow by heat conduction through the cryo-supports into the He-box in notated with $\dot{Q}_{\mathrm{cond\ cryo-s\ ac}}$ and the 'B' heat-in flow by conduction into the copper shield bottom plate is notated with $\dot{Q}_{\mathrm{cond\ cryo-s\ ab}}$.

Table 4.6. Geometrical properties of the cryo-supports.

Physical property	Section 1	Section 2	Section 3	Section 4
A_i	269 mm^2	239 mm^2	269 mm^2	239 mm^2
L_i	120 mm	124 mm	85 mm	89 mm
s_i	4 mm	2 mm	4 mm	2 mm
G_i	2.241 mm	1.926 mm	3.164 mm	2.683 mm
Material type	G-10	G-10	G-10	G-10
Orientation to beamline	Downstream	Downstream	Upstream	Upstream

While $\dot{Q}_{\text{cond cryo-s ab}}$ only flows from the bottom of the cryo-support cup through the outer G-10 tube directly ($G_{\text{cryo-s ab}} = G_2$), $\dot{Q}_{\text{cond cryo-s ac}}$ also flows through the connecting piece and the levelling screw on top of the inner G-10 tube. However, due to the short distance of only 5 mm from the G-10 tube to the outer surface of the He-box, the effect of the thermal resistivity for these two components will be neglected ($G_{\text{cryo-s ac}} = G_1$). Using a numerical integration of $k_{\text{G-10}}$ in normal direction by NIST [37] leads to a conductive heat flow in a downstream cryo-support of

$$\begin{aligned}\dot{Q}_{\text{cond cryo-s down ac}} &= G_1 \cdot (\Theta_{300\text{ K}} - \Theta_{4\text{ K}}) = 2.241\text{ mm} \cdot (114.0 - 0)\text{ W m}^{-1} \\ &\approx 0.26\text{ W}\end{aligned} \tag{4.41}$$

and

$$\begin{aligned}\dot{Q}_{\text{cond cryo-s down ab}} &= G_2 \cdot (\Theta_{300\text{ K}} - \Theta_{50\text{ K}}) = 1.926\text{ mm} \cdot (114.0 - 8.05)\text{ W m}^{-1} \\ &\approx 0.24\text{ W.}\end{aligned} \tag{4.42}$$

For the two shorter cryo-supports on the upstream side, the corresponding heat flows can be determined to $\dot{Q}_{\text{cond cryo-s up ac}} = 0.36\text{ W}$ and $\dot{Q}_{\text{cond cryo-s up ab}} = 0.28\text{ W}$. The resulting conductive heat flow in the all cryo supports is given with

$$\dot{Q}_{\text{cond cryo-s ac}} = 4 \cdot \dot{Q}_{\text{cond cryo-s down ac}} + 2 \cdot \dot{Q}_{\text{cond cryo-s up ac}} \approx 1.74\text{ W} \tag{4.43}$$

from shell ‘a’ to ‘c’ as ‘A’ heat-in flow. From shell ‘a’ to ‘b’ the ‘B’ heat-in flow is

$$\dot{Q}_{\text{cond cryo-s ab}} = 4 \cdot \dot{Q}_{\text{cond cryo-s down ab}} + 2 \cdot \dot{Q}_{\text{cond cryo-s up ab}} \approx 1.52\text{ W.} \tag{4.44}$$

4.3.4 Heat conduction inside the tail

At the tail there are several contact points of the OVC-shell with the other shells. This can be seen in Figure 3.1 on p.16. All heat flows located from shell ‘a’ to ‘c’ penetrate directly into the LHe if an operational level of $h = 15$ cm is considered. The calculation of the heat flows could be conducted analogue to chapters 4.3.1 to 4.3.3. Only the results are presented here. The values listed in Table 4.7 were provided by Michael Booth, one of the original cryostat design engineers from RAL. They were not recalculated in this Bachelor’s thesis.

Table 4.7. Conductive heat flow in the tail section.

Physical property	$\dot{Q}_{\text{cond tail stands ab}}$	$\dot{Q}_{\text{cond tail stands ac}}$	$\dot{Q}_{\text{cond tail top ac}}$	$\dot{Q}_{\text{cond tail bottom ac}}$
Heat flow type	-	A	A	A
Value	5.36 W	0.2 W	0.45 W	0.45 W

The index 'tail stands' refers to four mechanical stands located in the upper section of the tail that bear the load of the complete tail (see Figure 3.1). They have contact points with shell 'a', 'b' and 'c'. The indexes 'tail top' and 'tail bottom' refer to the connection of the UHV chamber to the rest of the experiment. As the UHV chamber is partly located inside the LHe and partly located outside the cryostat, heat from 300 K gets conducted into the LHe. The bellows on top and bottom with a wall thickness of only 0.2 mm represent the largest thermal resistance.

4.3.5 Summary of conductive heat flows in solid components

The sum of the calculated conductive heat flows in solid components is ~20.4 W. About 13.5 W flow into He-space and ~6.9 W flow onto the radiation shields.

Table 4.8. Summary of conductive heat flows in solid components.

Physical property	$\dot{Q}_{\text{cond chim}}$	$\dot{Q}_{\text{cond serv}}$	$\dot{Q}_{\text{cond cryo-s ac}}$	$\dot{Q}_{\text{cond cryo-s ab}}$
Heat flow type	A and B	A and B	A	-
Value	8.87 W	1.80 W	1.74 W	1.52 W
Physical property	$\dot{Q}_{\text{cond tail stands ab}}$	$\dot{Q}_{\text{cond tail stands ac}}$	$\dot{Q}_{\text{cond tail top ac}}$	$\dot{Q}_{\text{cond tail bottom}}$
Heat flow type	–	A	A	A
Value	5.36 W	0.2 W	0.45 W	0.45 W

Table 4.7 presents all conductive heat flows for the independent system calculated in chapter 0. A comparison of the heat flows into the He-space shows the largest proportion in the chimneys with ~66 %. The diameter of 200 mm causes a relevant cross-sectional area despite the thin wall thickness. It is noticeable that the bellow has the smallest geometrical factor G_{bellow} due to the ratio of compressed to outstretched length and its 0.6 mm wall thickness. It is alone more than 3 times larger than $G_{\text{upper pipe}}$ and $G_{\text{lower pipe}}$ together (see Table 4.4). The service tubes and the cryo supports each have a proportion of ~13 %. The cryo-supports have a proportion of ~8 %.

A clear classification of the presented heat flows into 'A' heat in-flows or 'B' heat in-flows is difficult. Undoubtedly $\dot{Q}_{\text{cond cryo-s ac}}$ and the tail heat conduction can be evaluated as type 'A'. In contrast, $\dot{Q}_{\text{cond chim}}$ and $\dot{Q}_{\text{cond serv}}$ first hit the upper edge of the He-box. Part of these heat flows gets absorbed by the gas. This depends on the convection of the GHe directly above the liquid on the ceiling of the He-box. The remaining heat flow might be conducted into the liquid in the wall of the He-box. Stainless steel is a very poor heat conductor, especially at cryogenic temperatures. A relevant proportion could nevertheless penetrate into the liquid and vaporise it with a 25 mm wall thickness of the He-box and a large cross-sectional area.

The calculated results of the independent systems show a possible thermal weak point at the chimneys. Chapter 4.6 will investigate this in more detail considering the VCL and HTS located inside the chimneys.

4.4 Heat conduction in gaseous helium

Heat conduction in GHe has to be considered for non-moving vapour. With clear movement, convection mixes the gas, prevents density stratification and dominates heat transfer. The following chapter will discuss gas conduction in service tubes and chimneys independently of possible convection or interaction of the vapour with the vessel walls or other components. Chapter 3.6.1 on p.21 indicates that heating of vapour by the wall can generate a strong natural convective boundary layer flow up the wall with a reverse flow in the centre [22, p. 44]. Nevertheless, the model of static gas will be used for now.

While the heat conductivity of ideal gases is independent of pressure, e.g. at ambient temperature for helium, it is dependent on it for real gases at cryogenic temperatures. Figure A.1 in the appendix shows $k(T)$ from boiling temperature to 300 K at 1100 mbar. The data to acquire this plot and the following results was taken from a NIST webbook table [39]. A Microsoft Excel (MSE) polynomial fit at the order of 6 with 30 digits was used to gain a function corresponding to the NIST data, which was then integrated in the desired temperature ranges. Because $k(T)$ drops about linearly from 300 K to 100 K and even more for temperatures below, the pressure dependence of k is negligible in the pressure range relevant for the ALPHA-g cryostat:

$$\left(\frac{\int_{4.45\ \mathrm{K}}^{300\ \mathrm{K}} k_{1200\ \mathrm{mbar}}(T)\ \mathrm{d}T - \int_{4.32\ \mathrm{K}}^{300\ \mathrm{K}} k_{1100\ \mathrm{mbar}}(T)\ \mathrm{d}T}{\int_{4.45\ \mathrm{K}}^{300\ \mathrm{K}} k_{1200\ \mathrm{mbar}}(T)\ \mathrm{d}T}\right) < \ 0.01\ \% \tag{4.45}$$

A pressure of $p_{\mathrm{He-space}} = 1100$ mbar as fixed boundary condition will be used.

4.4.1 GHe heat conduction in the service tubes

Vapour in the service tubes is trapped and cannot exit on the top. To estimate heat transfer in the GHe, a first but very important assumption will be made to simplify the model. In steady state with a constant liquid level, one might argue that vapour convection in the service tubes does not occur, but density stratification. An evaluation of this assumption must also consider that there are no baffles located in the service tubes. This assumption will be reviewed in chapter 4.6.6.

The temperatures of the gas cylinder in the service tubes represent the boundary condition and can be set to 300 K on top and about 4.3 K on the bottom. A length of a gas cylinder in the service tubes of $L = 820$ mm from the ceiling of the He-box to the HTS plate and a constant diameter of $d = 38$ mm (not respecting changes in the bellow region) will be considered. The gas conduction by Equation (2.7) and (2.8) for five service tubes (two are used as recovery) is given with

$$\dot{Q}_{\mathrm{gas\ cond\ serv}} = G \cdot \Delta\theta_{4.3\ \mathrm{K} \rightarrow 300\ \mathrm{K}} = 5 \cdot \frac{\pi \cdot 38^2\ \mathrm{mm}^2}{4 \cdot 820\ \mathrm{mm}} \cdot 27.828 \frac{\mathrm{W}}{\mathrm{m}} = 0.19\ \mathrm{W}. \tag{4.46}$$

Due to the relatively low thermal conductivity of GHe at temperatures $4.2\ \mathrm{K} \leq T \leq 12\ \mathrm{K}$, the result for $T_c = 12$ K would only change about 1 mW.

4.4.2 GHe heat conduction in the chimneys

As in the service tubes, the vapour in the chimneys is trapped and cannot exit on the top. The larger diameter of the gas cylinder $d = 200$ mm (not respecting changes in the bellow region) leads to a significantly higher heat load due to gas conduction. Chapter 4.3.1 on p.46 explained the general structure of the chimneys and their purpose. As mentioned, but not specified in that section, the chimneys contain the HTS which have a relevant influence on the thermodynamic conditions. The following chapter will, as also for the solid heat conduction in chapter 4.3.1, only look at an independent consideration of a heat flow, here, the gas conduction. A more detailed consideration with mutual dependencies of systems inside the chimneys will finally be discussed in the 'weak point analysis' in chapter 4.6.

If the chimney was empty, meaning without HTS and baffles, the gas heat conduction would be

$$\dot{Q}_{\text{gas cond chim}} = G \cdot \Delta\theta_{4.3\ \mathrm{K} \to 300\ \mathrm{K}} = 5 \cdot \frac{\pi \cdot 200^2\ \mathrm{mm}^2}{4 \cdot 820\ \mathrm{mm}} \cdot 27.714 \frac{\mathrm{W}}{\mathrm{m}} = 5.31\ \mathrm{W}. \qquad (4.47)$$

The same temperatures and gas cylinder length as for the service tubes is considered.

One has to highlight that this result does clearly not represent the true conductive heat flow through the gas in the chimney. In reality, the baffles and HTS might have a strong impact on the thermodynamic conditions. $\dot{Q}_{\text{gas cond chim}}$ should one serve as information to better understand the influence of the baffles and HTS, which will be respected in chapter 4.6.

4.5 Heat loss in transfer line

As with all cryogenic components of a cryostat, the transfer line must also be included in a thermal study. According to Fradkov and Ginodman [40], the length specific heat leak for a flexible siphon between two transport vessels has a typical value of $2\ \mathrm{W\,m^{-1}}$. In contrast, Dittmar et al. [27] measure the heat leak of a flexible line, which the authors consider as "representative for the majority of transfer lines used in cryogenic laboratories today." to a value of $3.22\ (\pm 1.17)\ \mathrm{W\,m^{-1}}$ [27]. Rigid transfer lines for permanent installations can reduce the specific heat transfer down to $0.04\ \mathrm{W\,m^{-1}}$, but use shield cooling by helium return gas or liquid nitrogen and cannot be compared to common flexible transfer lines [27].

The used flexible transfer lines at ALPHA are manufactured by

AS Scientific Products Ltd. According to a technical description on their website [41], a typical heat loss for their flexible transfer lines with an outer line diameter of 56 mm and bore size of 10 mm would be $1.0\ \mathrm{W\,m^{-1}}$. This type of transfer line has a typical mass flow rate of $150\ \mathrm{kg\,h^{-1}}$.

It is important to mention that not only the transfer line, but the complete transfer system might cause relevant heat loss. The flexible transfer line is inserted into a stinger, which goes from the HTS plate into the LHe inside the He-box. Especially the upper stinger section that is exposed to ambient air might cause additional heat leaks, but also the section inside the cryostat which is covered with superheated gas could have a measurable effect. To obtain a more realistic knowledge about the actual relevance of the heat leak outside the ALPHA-g cryostat, a consideration of the full transfer system needs to be carried out. An appropriate way to estimate this heat loss is to compare the LHe consumption during a cold test in steady state and compare it with the LHe consumption during the warm up phase.

On 25th of August 2021 a cold test was carried out. After the transfer was stopped, the LHe level decreased about linearly from $50\ \%$ to $0\ \%$ between 23:13 and 2:50 (3.62 hours). The LHe consumption during the warmup can be estimated with the help of Equation (3.5) to

$$\dot{V}_{\mathrm{LHe\ warm\ up}} = \frac{50\ \%}{3.62\ \mathrm{h}} = \frac{86.0\ \mathrm{L}}{3.62\ \mathrm{h}} = 23.8\ \frac{\mathrm{L}}{\mathrm{h}}. \tag{4.48}$$

On the evening of 25th August, the LHe level was kept approx. constant between 18:30 and 22:45 (4.25 h). During the cold test, the LHe level in the Dewar decreased 216.2 L in the same time, which leads to a Dewar consumption of $\dot{V}_{\mathrm{LHe\ Dewar}} = 50.9\ \mathrm{L\ h^{-1}}$. This consumption in the Dewar can now be compared to the actual LHe consumption of the isolated cryostat during the warm up. With a difference in consumption of $\Delta\dot{V}_{\mathrm{LHe}} = \dot{V}_{\mathrm{LHe\ Dewar}} - \dot{V}_{\mathrm{LHe\ warm\ up}} = 27.1\ \mathrm{L\ h^{-1}}$, a helium enthalpy of vaporization Δh^{v} of 20.72 kJ kg^{-1} [22, p. 43] and a liquid density of $\rho_{\mathrm{liq}} = 125\ \mathrm{kg\ m^{-3}}$ [22, p. 43], the heat loss in the complete transfer system may be determined to

$$\dot{Q}_{\mathrm{transfer\ system}} = \Delta\dot{V}_{\mathrm{LHe}}\ \rho_{\mathrm{LHe}}\ \Delta h^{\mathrm{v}} = 19.5\ \mathrm{W}. \tag{4.49}$$

Considering only the flexible transfer line with a length of 2 m, the specific heat loss per length is given with $\dot{q}_{\mathrm{flex\ transfer\ line}} = 9.8\ \mathrm{W\ m^{-1}}$.

One has to mention that the result contains an inaccuracy of several watts. First, the Dewar volume is determined using a level probe inside it. Slight variations in the Dewar cross-section area can change the result. In addition, the liquid level oscillated by about $\pm 1\ \%$ in the period considered for the determination of $\dot{V}_{\mathrm{LHe\ Dewar}}$. Nevertheless, the high heat flow $\dot{Q}_{\mathrm{transfer\ system}}$ proves to be highly relevant for the thermal efficiency of the cryostat. With the determined values, no conclusions can be drawn about the ratios of the heat flow in the stingers and the flexible transfer line. However, it seems likely the flexible transfer line makes a significant contribution to the heat loss. The shortest possible line in the final construction is therefore mandatory regarding the thermal efficiency. The use of a rigid transfer line could probably also significantly reduce heat losses.

4.6 Weak point analysis: Thermal conditions inside the chimneys

Previous calculations have shown that the conductive heat load in the chimneys is 8.87 W. This has a large impact on the thermal efficiency of the cryostat. Additionally, heat conduction in gas inside in the chimneys is also relevant with 5.17 W (not considering convection and the HTS). For the given results, independent thermodynamic systems were used to estimate the influence of different components on the thermal efficiency and the LHe consumption of the ALPHA-g cryostat. A more precise analysis with mutual dependencies in between the thermodynamic systems will be carried out. This gains a general understanding of the influence and distribution of GHe within the He-space. It takes the following heat transfer systems into account:

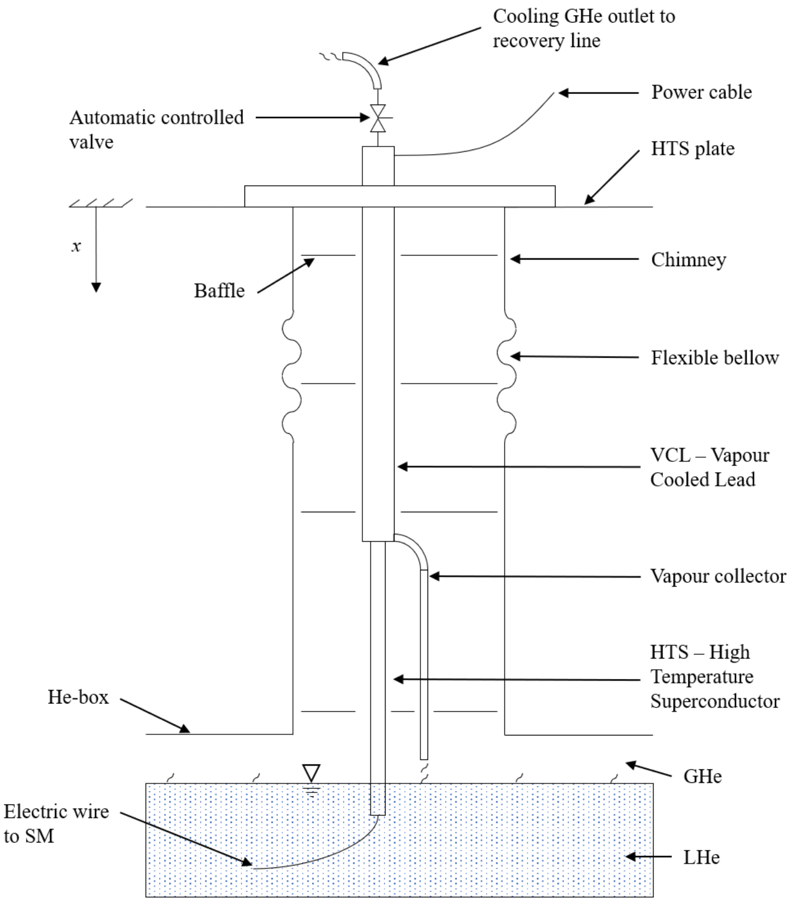

Figure 4.9. Schematic illustration of one VCL and HTS lead inside a chimney. The HTS is bathing in LHe. The VCL is surrounded by GHe. Some of the helium vapour that evaporates gets collected and guided to the VCL to cool it. It exits above the HTS plate into the recovery line through an automatic valve that controls the temperature of the VCL by adjusting the mass flow inside it. The baffles are radiation shields and prevent vapour convection by density stratification. The real model has 10 circularly arranged leads instead of the one shown.

- Solid heat conduction in the chimney walls.
- Solid heat conduction in the VCL and HTS.
- Joule heating inside the VCL caused by electric current.
- Convective heat transfer around the VCL.
- Gaseous heat conduction of the vapour located inside the chimneys.
- Possible convective heat transfer between all mentioned components.

The aim of the more precise investigation in the chimneys is to find a realistic temperature distribution and the associated heat flows in the chimney pipe, the VCL, the HTS and the vapour. This allows a discussion on adaptation or optimisation of the cryostat. The following six aspects are presented:

1. Influence of the bellow length and a possible adjustment of it to reduce heat transfer.
2. Temperature distribution at the outer chimney wall in the upper section and a possible reversal of the net direction of radiation as compared to the intended direction by design.
3. General influence of the VCL and HTS on the thermal conditions in the chimney.
4. Determination of the VCL bottom temperature.
5. Possible adjustment of the baffle separation distances.
6. Influence of radiation from the lowest baffle directly into the LHe.

4.6.1 Description of the HTS

The high-temperature superconductors provide the power for the superconducting magnets in the antihydrogen atom trap. ALPHA-g uses two different versions of HTS with a different electrical current: three modules with ten leads of 150 A each and one module with four leads of 1000 A each. The modules are placed inside the chimneys. As there are five chimneys in total but only four HTS modules; one of the chimneys is only used as a feedthrough for wires. The HTS are designed and manufactured by the company American Magnetics Inc. (AMI).

The schematic structure of the HTS is shown in Figure 4.9. A more detailed illustration can be found in the appendix in Figure C.5 on p.102.

4.6.1.1 Internal heat source inside VCL

The VCL is not a superconductor and therefore dissipates energy into the system when electric current flows through. Ohm's law $U = R \cdot I$ and the power dissipated $P = U \cdot I$ lead to a dissipation rate of $P = R \cdot I^2$. With an "estimated voltage drop along a vapour cooled lead pair of about $\Delta U = 200\ \mathrm{mV}$ or less" according to the engineering department of AMI, a conservative value for the heat source of a single VCL is given with $P_{\mathrm{VCL\,single}} = \Delta U \cdot I = 100\ \mathrm{mV} \cdot 150\ \mathrm{A} = 15\ \mathrm{W}$, or $150\ \mathrm{W}$ for 5 pairs. The volume of one VCL is $V = A \cdot L = 7.164 \cdot 10^{-5}\ \mathrm{m}^2 \cdot 0.641\ \mathrm{m} \approx 4.592 \cdot 10^{-5}\ \mathrm{m}^3$. This leads to an internal heat source density $\dot{\omega}_{\mathrm{VCL}} = P_{\mathrm{VCL\,single}} \cdot V^{-1} = 326.7\ \mathrm{kW\,m^{-3}}$.

The heat source of all VCL is given with

$$P_{\mathrm{VCL}} = 30 \cdot 0.1\ \mathrm{V} \cdot 150\ \mathrm{A} + 4 \cdot 0.1\ \mathrm{V} \cdot 1000\ \mathrm{A} = 850\ \mathrm{W} \tag{4.50}$$

4.6.1.2 Convection around VCL – Determination of α

A large amount of the internal heat source in the VCL is absorbed by cooling vapour. The lead is surrounded with an annular gap and a G-10 tube. The vapour flows between the VCL and the G-10 tube. A technical drawing in appendix Figure C.4 shows the relevant dimensions for the performed simulation. The forced convection is caused by a pressure differential $\Delta p = p_{\mathrm{He-space}} - p_{\mathrm{rec}}$. AMI gives a typical value of $\sim 3\ \mathrm{mbar}$ [42]. While p_{rec} has typical values of 40 to $50\ \mathrm{mbar}$, Δp stagnated at $50\ \mathrm{mbar}$ with $p_{\mathrm{He-space}} \approx 100\ \mathrm{mbar}$ most of the time during a cold test on 2nd July 2021. At these pressure ratios, sufficient convection generation can be assumed.

The heat transfer coefficient for concentric annular gaps may be determined with [43, p. 814]

$$\alpha = \frac{Nu \cdot k}{d_{\mathrm{h}}}. \tag{4.51}$$

It can be obtained with the Nusselt number Nu, the thermal conductivity of the vapour k and the hydraulic diameter d_{h}, which is given by

$$d_{\mathrm{h}} = d_{\mathrm{o}} - d_{\mathrm{i}} = \text{[redacted]}. \tag{4.52}$$

Here, d_o denotes the inner diameter of the outer G-10 tube and d_i the outer diameter of the VCL. First, the flow conditions have to be investigated to determine Nu. Perfect heat exchange between the vapour and the conductor, an inlet temperature of $T_\mathrm{i} \approx 50$ K and an outlet temperature of $T_\mathrm{o} \approx 300\ K$ is assumed. The required cooling mass flow per VCL is

$$\dot{m}_{\mathrm{VCL\,single}} = \frac{P_{\mathrm{VCL\,single}}}{\Delta h_{50\,\mathrm{K} \rightarrow 300\,\mathrm{K}}} = \frac{15\ \mathrm{W}}{(1563.5 - 264.99)\ \mathrm{kJ\,kg^{-1}}} = 0.01155\ \frac{\mathrm{g}}{\mathrm{s}}. \tag{4.53}$$

This mass flow leads to a mean gas velocity of

$$v_\mathrm{m} = \frac{4\,\dot{m}_{\mathrm{VCL\,single}}}{\pi\,\rho_\mathrm{m}\,({d_\mathrm{o}}^2 - {d_\mathrm{i}}^2)} = \text{[redacted]}\ \frac{\mathrm{m}}{\mathrm{s}}, \tag{4.54}$$

which results in a mean Reynolds number of [43, p. 814]

$$Re_\mathrm{m} = \frac{v_\mathrm{m}\,d_\mathrm{h}\,\rho_\mathrm{m}}{\eta} \approx \text{[redacted]} \ll Re_{\mathrm{crit}} = 2300. \tag{4.55}$$

The low value of Re clearly indicates a laminar flow. The material values of the GHe are referred to the mean fluid temperature $T_\mathrm{m} = (T_\mathrm{i} + T_\mathrm{o})/2 = 175$ K [43, p. 814] and 1100 mbar.

Knowing that the flow is in the laminar regime, Nu can now be estimated. For thermally and hydrodynamically formed laminar flow at constant wall temperature, Stephan [44] gives a mean Nusselt number of $Nu_\mathrm{m} \approx$ [redacted] with $d_\mathrm{i}/d_\mathrm{o} =$ [redacted]. This contains the assumption that the heat transfer takes place from both, the outer G-10 tube and the VCL with the same wall temperatures. With $k(T_\mathrm{m}) = 0.10769\ \mathrm{W\,m^{-1}\,K^{-1}}$ and Nu_m the mean heat transfer coefficient is $\alpha_\mathrm{m} \approx 130\ \mathrm{W\,m^{-2}\,K^{-1}}$.

4.6.2 Setup of the ANSYS workbench simulations

Several ANSYS simulations with the function 'Steady-State Thermal' were performed. The CAD models from Autodesk Inventor were exported into a .step file and imported into ANSYS. Subsequently, the thermal conductivities in 'Engineering Data' were imported from MSE files based on NIST and the provider AMI in the range from 4 K to 300 K. The set-up of the simulations included the definition of boundary conditions. These were mainly temperatures and in one simulation also convection and internal heat generation inside the VCL. The mesh was auto-generated in default settings. In the final simulation run, the mesh sizing resolution was increased from the default setting 2 up to 7, depending on the performance of the computer. It should be mentioned that even with resolution 1, the simulation was often terminated without a result output due to an overload of the computer processing power. By closing all other programs, the performance could be partially improved. Accordingly, the used hardware was not fully adequate (Intel® Core™ i5-6500 CPU @ 3.20 GHz, 16 GB RAM, Intel® HD Graphics 530).

The solution output was set to solve the temperature and three-dimensional heat flux of all bodies. The function 'Construction geometry → Path' was used to solve the temperature along desired paths. To do so, ANSYS SpaceClaim and DesignModeler were used to create new bodies and planes, split surfaces and create edges that can be chosen to define paths.

4.6.3 Simulation of heat conduction in chimney and GHe

The complexity of the simulations was increased iteratively by adding components and boundary conditions to show the influence of the individual systems on the temperatures and heat flows.

First, a chimney was considered independently with boundary conditions of 300 K at the top end of the pipe and 4 K at the bottom end of the pipe. The temperature distribution results from heat conduction, as it was also considered in chapter 4.3.1. Second, a static gas cylinder was examined independently with equal boundary conditions as also in chapter 4.4.2. Third, the chimney was then filled with static GHe using ANSYS DesignModeler. A simulation of heat conduction inside the chimney, inside the gas and in between those two systems was performed.

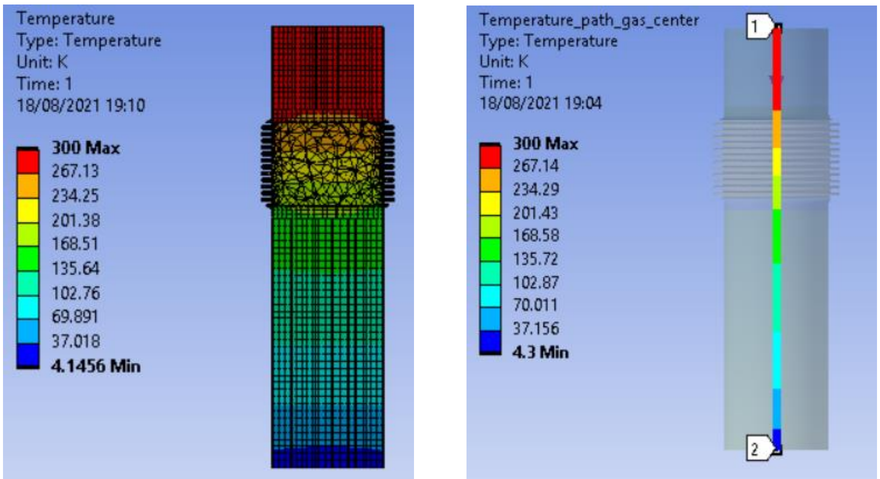

Figure 4.10. Screenshot of the 3rd ANSYS simulation. The left picture shows a half-section view of the temperature plot. The chimney is filled with static vapour. The right picture shows the temperature along a defined path in the centre of the vapour.

An example of the ANSYS results is shown in Figure 4.10. The temperature distribution of three different simulations mentioned above is presented in Figure 4.11. The length x starts with $0 = x_0$ at the top of the HTS plate as referred in Figure 4.9. Position x_1 indicates the beginning of the bellow and x_2 the end of it. Position x_3 indicates the bottom end of the chimney.

4.6.3.1 Simulation 1

For simulation 1, the temperature in the upper chimney pipe decreases from 300 K to around 288 K up to x_1, as shown in Figure 4.11. There, it drops sharply down to 100 K at x_2. In the lower pipe, the temperature decreases further to the set boundary condition of 4 K at x_3. The bellows act as a thermal resistor – causing the temperature to drop more quickly over a short vertical distance. They have an outstretched length of about 567 mm as calculated in Equation (4.32) and (4.33) on p.47 and a thin wall thickness of 0.6 mm. This causes them to be a strong thermal resistor. The significant influence of the flexible bellow might imply that a longer flexible bellow would improve the thermal performance of the ALPHA-g cryostat. The non-linear temperature decrease in the bottom section is caused by the likewise nonlinear $k_{\text{stainless steel}}$. Simulation 1 gives a homogeneous heat flow in the chimney of $\dot{Q}_{\text{chim}} = 1.76$ W. This value is close to the hand calculated value of 1.77 W in Equation (4.37).

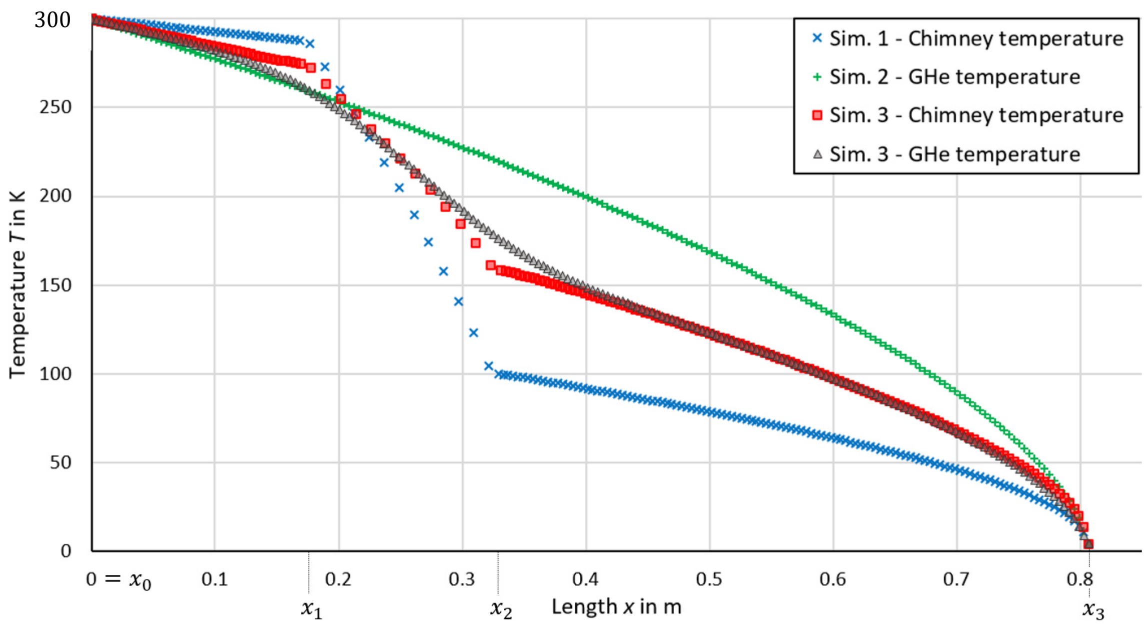

Figure 4.11. Temperature T over length x for three different ANSYS simulations. The blue × indicates the temperature plot along a path on the chimney wall in simulation 1, considering only the chimney independently. The green + indicates the temperature plot along a path in the centre of a static GHe cylinder in simulation 2, considering only the GHe cylinder independently. The red ■ indicates the temperature plot along a path on the chimney wall in simulation 3, considering a chimney filled with GHe. The grey ▲ indicates the temperature plot along a path in the centre of the static GHe in simulation 3, considering a chimney filled with GHe.

Table 4.9. Temperatures and heat flows of simulation 1, 2 and 3.

Component	Sim. #	$T(x_1)$	$T(x_2)$	$\dot{Q}_{\text{upper pipe}}$	$\dot{Q}_{\text{bellow}}$	$\dot{Q}_{\text{lower pipe}}$
Chimney	1	288 K	100 K	1.76 W	1.76 W	1.76 W
Chimney	3	275 K	158 K	3.62 W	0.67 W	3.79 W
GHe	2	261 K	219 K	1.08 W	1.08 W	1.08 W
GHe	3	263 K	175 K	0.85 W	2.34 W	0.68 W

4.6.3.2 Simulation 2

For simulation 2, the temperature in the GHe cylinder decreases continuously from 300 K to 4 K. The non-linear temperature decrease is again caused by the likewise non-linear k_{GHe}. Simulation 2 gives a heat flow in the GHe of $\dot{Q}_{\text{GHe}} = 1.08$ W. This value is close to the hand calculated value of 1.06 W in Equation (4.47).

4.6.3.3 Simulation 3

Simulation 3 now combines both independent systems of the chimney and vapour. Their temperatures converge. The result is approximately the same as the arithmetic mean value of both temperatures. This is especially visible between x_2 and x_3. The chimney temperature in x_1 decreases from 288 K to 275 K and increases in x_2 from 100 K to 158 K as compared to simulation 1 and 2. In contrast, the gas temperature takes on a more complex form.

The chimney and the vapour now exchange heat with each other. Therefore, the heat flow is not homogeneous anymore in the different sections, as it was for the independent simulations. Simulation 1 defined the heat flow for all sections to be $\dot{Q}_{\mathrm{chim}} = 1.76\ \mathrm{W}$. Simulation 3 now gives a heat flow in the chimney pipes of $\dot{Q}_{\mathrm{upper\ pipe}} = 3.62\ \mathrm{W}$ resp. $\dot{Q}_{\mathrm{lower\ pipe}} = 3.79\ \mathrm{W}$ and in the bellow of $\dot{Q}_{\mathrm{bellow}} = 0.67\ \mathrm{W}$. The value in the pipe sections is about twice as high as in simulation 1, while the value in the bellow section is about 2.5 times lower than in simulation 1. This can be explained by looking at the temperature graphs in Figure 4.11 and thermal conductivity integral of stainless steel: The differential temperature in both pipe sections increased in simulation 3, which also increased $\Delta\Theta$. Simulation 1 gave $T(x_2) = 100\ \mathrm{K}$ which corresponds to $\Delta\Theta_{4\ \mathrm{K} \to 100\ \mathrm{K}} = 527\ \mathrm{W\ m^{-1}}$ [35]. Simulation 3 gave $T(x_2) = 158\ \mathrm{K}$ which corresponds to $\Delta\Theta_{4\ \mathrm{K} \to 158\ \mathrm{K}} = 1147\ \mathrm{W\ m^{-1}}$. One can see that the higher $\Delta\Theta_{4\ \mathrm{K} \to 158\ \mathrm{K}}$ increases $\dot{Q}_{\mathrm{cond}} = G \cdot \Delta\Theta$ on the lower chimney pipe. In contrast, the differential temperature on the bellow decreased in simulation 3 which also lowered $\Delta\Theta_{100\ \mathrm{K} \to 288\ \mathrm{K}} = 2370\ \mathrm{W\ m^{-1}}$ down to $\Delta\Theta_{158\ \mathrm{K} \to 273\ \mathrm{K}} = 1529\ \mathrm{W\ m^{-1}}$. The corresponding geometrical factors G_i can be found in Table 4.4 on p.46. Heat conduction in GHe from simulation 3 is listed in Table 4.9.

From Figure 4.11 and Table 4.9 it can be deduced that the heat exchange between chimney and static vapour is clearly relevant. The influence of the bellows as thermal resistance is reduced by about 40 % when the gas is taken into account compared to the independent consideration. In summary, it is beneficial in terms of thermal efficiency if there is a large differential temperature at the bellow and a small one at the pipe sections. This is caused by the low geometric factor of the bellows.

4.6.4 Simulation of heat conduction in chimney, GHe and ten 150 A VCL

The following simulations included the VCL and HTS without baffles. As the provided CAD model from AMI is only a surface model, a new solid CAD model first had to be created which can be found in appendix Figure C.4. Dimensions for this were derived from the given model.

The gas between the baffles is considered as static. Therefore, an influence of the baffles on the simulations is only present on the heat conduction. The 1.6 and 3 mm thin plates only slightly reduce it. Subsequent to the simulations, the assumption that there is no free convection between the baffles will be checked. The simulations were carried out for the 150 A version with ten leads.

Two separate simulations were performed. Simulation 4 investigated the VCL temperature distribution due to only heat conduction. The boundary conditions of were set to 300 K on the top and 50 K on the bottom of the VCL. Simulation 5 then investigated the full system. The boundary conditions were set as in simulations 1 to 3. Simulation 5 also includes the internal heat generation $\dot{\omega}_{\mathrm{VCL}}$, the convection with α_{m} and heat conduction in the VCL, HTS and the G-10 tubes. The data for k_{VCL} was provided by AMI as conductivity integral. An MSE polynomial fit at the order of 6 with 30 digits gained a corresponding function which was then derived to obtain the thermal conductivity for ANSYS. AMI could not provide the exact HTS material composition and data for k_{HTS}. The company only mentions on their website that “the most commonly used conductor material is BiSCCO 2223 doped with a Au/Ag alloy” [42]. Experimental values for different types of $k_{\mathrm{BiSCCO\ 2223}}$ can be found in [45] and [46].

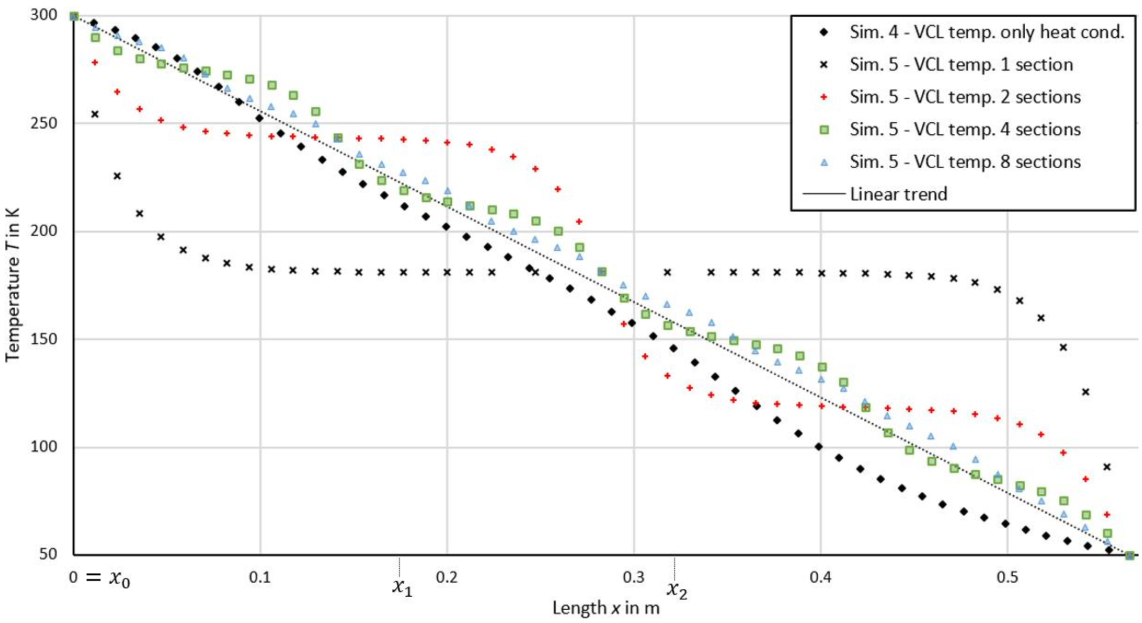

Figure 4.12. VCL temperature over length for different simulations. Simulation 4 shows the results considering an independent VCL with only heat conduction. Simulation 5 shows the results of the full model including internal heat sources, convection around the VCLs and conduction. It was performed four times with different sections along the lateral VCL surfaces with different T_{GHe}. The number of sections for each graph is indicated in the legend. The linear trend only serves as a comparison and does not represent a result.

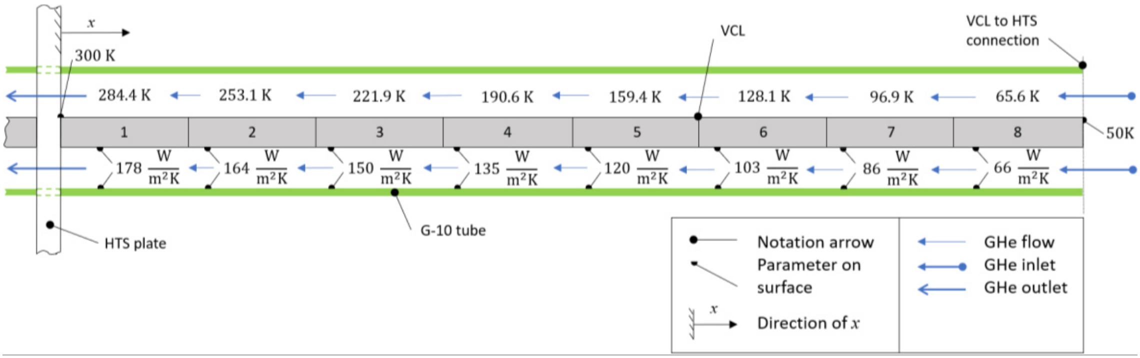

Figure 4.13. Schematic half-section view of one VCL with its surrounding G-10 tube. The view is rotated anticlockwise by 90°. The right side indicates the VCL to HTS connection and the gas inlet. The left side indicates the HTS plate and the gas outlet. The VCL is divided into 8 sections with the corresponding linear temperature distribution as considered for simulation 5. The $T_{\mathrm{GHe},i}$ and $\alpha_{\mathrm{m},i}$ of each individual section are shown. The individual $\alpha_{\mathrm{m},i}$ apply to both, the inner G-10 surface and the outer VCL surface. Dimensions are not to scale.

4.6.4.1 Simulation 4

Simulation 4 showed a roughly linear temperature distribution in the VCL which results from $k_{\mathrm{VCL}}(T)$ in this independent consideration. This is presented in Figure 4.12. The simulation determined the heat flow to be $\dot{Q}_{\mathrm{VCL\ single}} = 1.15$ W.

4.6.4.2 Simulation 5

The settings of the forced convection contain the heat transfer coefficient α_{m}. It is present at a mean gas temperature, hereafter denoted with T_{GHe}. First, the values in the simulation were set to only one uniform convection along the full length of the VCL with $T_{\mathrm{GHe}} = T_{\mathrm{m}} = 175$ K. Along most of the length, the VCL adopted $\sim T_{\mathrm{GHe}}$, as presented in Figure 4.12. This result can be seen as unrealistic. T_{m} is used as the mean fluid temperature for the material values [43, p. 814]. It does not represent an actual constant gas temperature along the surface of the convection. However, the ANSYS simulation considers T_{GHe} as constant and does not respect it as function of the vertical VCL position. In order to compensate this influence of a constant T_{GHe} and to obtain a more realistic result, the lateral surface of the VCL was split into 2, 4 and 8 sections. Each individual section was then assigned with an individual $T_{\mathrm{GHe},i}$ and their corresponding $\alpha_{\mathrm{m},i}$. The $T_{\mathrm{GHe},i}$ are based on a linear temperature trend. This is shown in Figure 4.13 for the model with 8 sections.

By Figure 4.12 the VCL temperature becomes linear as we increase the number of sections. For 8 sections, the oscillation is < 5 K. The results of simulation 5 with 1, 2 and 4 sections will be discarded due to the discussed dominance of a constant T_{GHe}. The setup can be seen as in-accurate here. All remaining paragraphs of this chapter all refer to simulation 5 with 8 sections.

By Figure 4.12 the VCL temperature becomes linear as we increase the number of sections. For 8 sections, the oscillation is < 5 K. The results of simulation 5 with 1, 2 and 4 sections will be discarded due to the discussed dominance of a constant T_{GHe}. The setup can be seen as in-accurate here. All remaining paragraphs of this chapter all refer to simulation 5 with 8 sections.

The results of simulation 5 in Figure 4.14 show the temperatures of the individual components to be nearly the same in most positions. This suggests a relevant heat conduction in the horizontal plane. The chimney temperature in simulation 3 was 275 K at x_1 (beginning of bellow) and now dropped to 241 K in simulation 5. At x_2 (end of bellow) it dropped from 158 K to 140 K. The temperature difference from x_1 to x_2 thus decreased from 34 K in simulation 5 to 18 K in simulation 3. This indicates a further reduction in the influence of the bellow as a thermal resistor, as already observed in simulation 3 compared to simulation 1. The GHe temperature in simulation 5 dropped over the entire length by $\sim$30 K compared to simulation 3. In simulation 5 the GHe temperature remains close to the VCL temperature. The VCL temperature decreases about linearly from 300 K to 50 K as it was also the case for 8 sections in Figure 4.12. The HTS temperature then continues with a nonlinear temperature decrease down to 4 K.

The heat flows generated with simulation 5 fluctuate strongly along each component. As already mentioned in simulation 3, the heat flows are no longer constant due to the mutual heat exchange of the individual components. Therefore, the heat flows in Table 4.10 are calculated with the function 'Contact probe' in ANSYS at the bottom surface of the model. This is the relevant position, since there the heat flow goes further into the He-box, the GHe or the LHe.

The vertical heat flow at this position in a single chimney is $\dot{Q}_{\mathrm{chim}} = 1.11$ W, the heat flow in the GHe located in one chimney is $\dot{Q}_{\mathrm{GHe}} = 0.06$ W, and the heat flow in ten HTS leads is $\dot{Q}_{10\ \mathrm{HTS}} = 3.13$ W. The heat flow inside the VCL depends strongly on the vertical position. The result is less important as the heat flow continues into the HTS. Using the function 'Directional heat flux along path', ANSYS determines an average heat flow of $\dot{Q}_{10\ \mathrm{VCL}} = 11.29$ W along the length of the all VCLs in simulation 5.

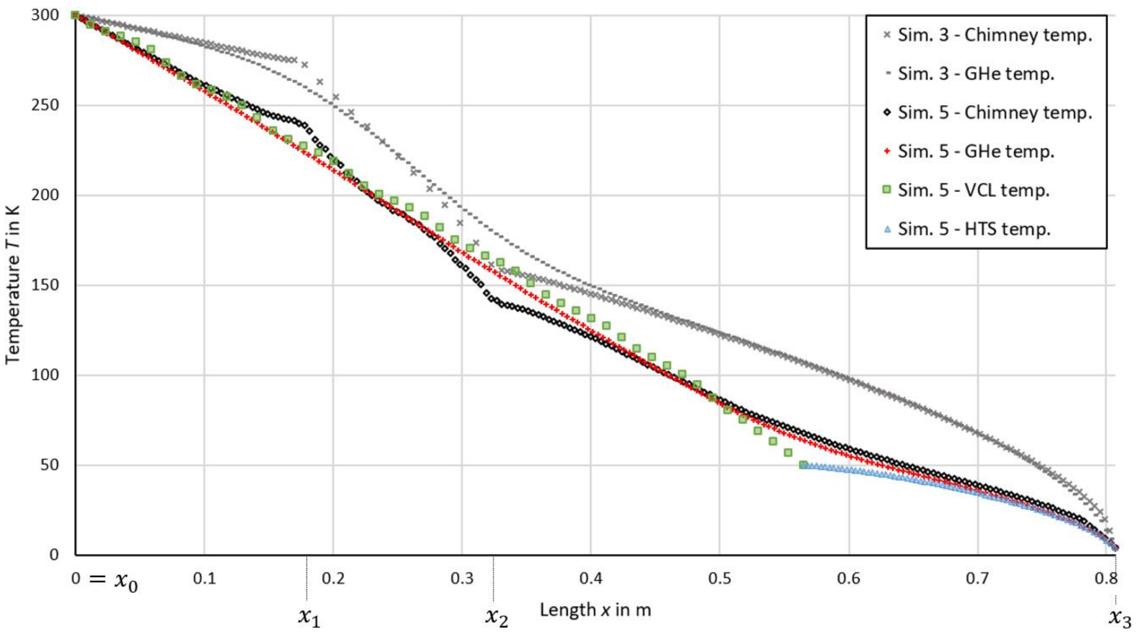

Figure 4.14. Temperature over length for simulation 5 with the ten 150 A VCL divided into 8 sections as compared to simulation 3. The simulation included internal heat sources, convection around the VCL and conduction of all components. A boundary condition of 50 K was set at the bottom surfaces of the VCL Free convection and radiation between the baffles is not modelled.

Table 4.10. Heat flows of simulation 5 for a single chimney determined with 'Contact probe' and 'Directional heat flux along path'.

$\dot{Q}_{\mathrm{GHe}}$	$\dot{Q}_{\mathrm{chim}}$	$\dot{Q}_{\mathrm{10\ HTS}}$	$\dot{Q}_{\mathrm{10\ VCL}}$
0.06 W	1.11 W	3.13 W	11.29 W

4.6.4.3 Determination of the VCL bottom temperature

The boundary condition $T_{\mathrm{VCL\ bottom\ surface}} = 50$ K is based on experiments in the cryogenic laboratory by ALPHA. Beside the presented results of the temperature distribution and heat flows in the components, an attempt was made to determine an own value for $T_{\mathrm{VCL\ bottom\ surface}}$ with simulation 5. Unfortunately, this is not possible with the simulation presented here. The simulation can run without the boundary condition of 50 K, but then the lowest of the eight sections of the VCL adopts $\sim T_{\mathrm{GHe}}$ from the boundary condition of the convection. This is because the information of the 50 K is still contained in T_{GHe} of the convection. If convection and heat generation are also removed, $T_{\mathrm{VCL\ bottom\ surface}} = 107$ K. This value, however, cannot be considered real without convection and $\dot{\omega}$. Besides, it would also be too warm for the HTS to function properly. AMI suggests to control the cooling GHe flow of the VCL by measuring the voltage drop rather than $T_{\mathrm{VCL\ bottom\ surface}}$. The engineering department estimates that $T_{\mathrm{VCL\ bottom\ surface}}$ will result in ~50 K.

4.6.5 Convection inside between chimney baffles – an approach

All performed simulations and analytic calculations assumed that the vapour in the chimneys and service tubes is static. The following sections will discuss the probability of convection inside the chimney.

The driving force of possible convection in the chimney is the temperature gradient of the walls and the density gradient of the gas. There is no pressure difference as in the case of VCL convection. Accordingly, possible convection is free convection. A determination of free convection, is usually based on empirical formulas and contains large uncertainties like it is also the case for forced convection. The relationship of α, Nu and k from Equation (4.51) applies for free convection as well [47]. Nu can be determined using the Rayleigh number

$$Ra = \frac{\beta \cdot \mathrm{g} \cdot \Delta T \cdot L^3}{\nu \cdot \kappa}, \tag{4.56}$$

where β denotes the isobaric coefficient of thermal expansion, g the gravity acceleration, L the characteristic length, ν the kinematic viscosity and κ the thermal diffusivity [47]. For the given case in the chimney of a cylinder section, L is the cylinder height and $\beta = {T_*}^{-1}$ for ideal gases [47]. $T_* = (T_1 + T_2)/2$ denotes the reference temperature which is also used for the material values ν and κ [47]. The temperatures T_1 and T_2 refer to the upper and lower circular surface of the cylinder which represent the baffle temperature. The given model assumes adiabatic walls that enclose the cylinder which would be the chimney walls [47].

Inside each chimney there are nine baffles located in total. Possible convection will be investigated between the HTS plate and the first baffle (α_{01}) and between the penultimate and last baffle (α_{89}). These are the most relevant positions. Additionally, possible convection between the third and fourth baffle (α_{34}) could be of interest, since it is located in the bellow region. The temperatures to determine α_{ij} were used from simulation 5 ("GHe temp." in Figure 4.14).

For possible convection between the HTS plate and the first baffle, $T_0 = 300$ K and $T_1 = 289$ K were used. The baffle distance is $L = 75$ mm. With the corresponding material values of GHe at 1100 mbar for T_* from [39], $Ra_{01} \approx 8585$. This indicates the laminar regime. Following the empirical correlation can be used to determine the Nusselt number [48]:

$$Nu = 0.208 \cdot Ra^{0.25}. \tag{4.57}$$

This leads to $Nu_{01} \approx 2.0$ which results in $\alpha_{01} \approx 4$ W m^{-2} K^{-1}. For possible convection between the third and fourth baffle with $T_3 = 240$ K, $T_4 = 196$ K and $L = 75$ mm, the Rayleigh number is given with $Ra_{34} \approx 1.25 \cdot 10^5$ which indicates the turbulent regime. The empirical correlation can be used [48]:

$$Nu = 0.092 \cdot Ra^{0.33}. \tag{4.58}$$

This leads to $Nu_{34} \approx 4.4$ which results in $\alpha_{34} \approx 7$ W m^{-2} K^{-1}. The last investigation will be carried out between baffle number eight and nine, with $T_8 = 74$ K, $T_9 = 16$ K and $L = 122$ mm. For a proper value of α_{89}, it would be necessary to perform a more complex consideration of the temperature dependence of the material values (since ΔT is not $\ll T_*$) [47]. The usage of Equation

(4.58) would nevertheless lead to a rough estimation of $Ra_{89} \approx 6.4 \cdot 10^8$ and $Nu_{89} \approx 74$. This could result in $\alpha_{89} \approx 27$ W m^{-2} K^{-1}.

4.6.6 Possible convection inside the service tubes

In contrast to the chimneys, the service tubes do not have baffles located inside them. This increases the characteristic length up to $L = 792$ mm. Assuming $T_1 = 300$ K and $T_2 = 4$ K, the given Rayleigh number is high with $Ra_{\mathrm{serv}} \approx 4.8 \cdot 10^9$. This leads to $\alpha_{\mathrm{serv}} \approx 145$ W m^{-2} K^{-1} by Equation (4.51) and (4.58). The value can only be used to give a rough estimation because again, ΔT is not $\ll T_*$.

Despite the inaccuracy of α_{serv} due to $\Delta T > T_*$, the value shows a possible strong convection in the service tubes compared to the chimneys. This could be suppressed by inserting baffles. To check whether baffles should also be inserted in the service tubes, a specified consideration of the temperature dependence of the material values must be carried out.

4.6.7 Radiation from the lowest baffle into LHe

The lowest baffles and service tubes radiate directly into the LHe. Simulation 5 determined the temperature at the position of the lowest baffle to $T = 16$ K. It is assumed that the LHe has a transmissivity of $\tau = 1$ and the He-box absorbs part of the heat radiation with $\varepsilon_{\mathrm{c}} = 0.24$. The emissivity of the baffle (made of G-10) is assumed with a conservative value of $\varepsilon_{\mathrm{G-10}} = 1$. This leads to the heat radiation of 5 baffles into the LHe according to Equation (2.20) with the corresponding surface area sizes of

$$\begin{aligned}\dot{Q}_{\mathrm{rad\ baffle \to LHe}} &= 5 \cdot 0.0241\ \mathrm{m}^2 \cdot \frac{(16^4 - 4^4)\ \mathrm{K}^4 \cdot 5.6704 \cdot 10^{-8}\ \mathrm{W\ m^{-2}\ K^{-4}}}{\frac{1}{1} + \left(\frac{1}{0.24} - 1\right) \cdot \frac{0.0241\ \mathrm{m}^2}{0.648\ \mathrm{m}^2}} \\ &\approx 4 \cdot 10^{-4}\ \mathrm{W} \ \approx 0.\end{aligned} \tag{4.59}$$

In comparison to the baffles, the service tubes have a much larger temperature gradient ($T_{\mathrm{a}} = 300$ K to $T_{\mathrm{c}} = 4$ K), but also a smaller surface area (0.00113 m^2). Considering emissive coefficients of $\varepsilon_{\mathrm{a}} = \varepsilon_{\mathrm{c}} = 0.24$ and $\tau = 1$ of LHe, the heat radiation for seven service tubes may be determined to

$$\begin{aligned}\dot{Q}_{\mathrm{rad\ serv \to LHe}} &= 7 \cdot 0.00113\ \mathrm{m}^2 \cdot \frac{(300^4 - 4^4)\ \mathrm{K}^4 \cdot 5.6704 \cdot 10^{-8}\ \mathrm{W\ m^{-2}\ K^{-4}}}{\frac{1}{0.24} + \left(\frac{1}{0.24} - 1\right) \cdot \frac{0.00113\ \mathrm{m}^2}{0.00113\ \mathrm{m}^2}} \\ &\approx 0.08\ \mathrm{W}.\end{aligned} \tag{4.60}$$

This takes equal radiation surface areas into account. The radiation must pass through the thin and long tube before it is absorbed at the bottom of the He-box.

4.6.8 Analysis of the performed heat simulations

The introduction in chapter 4.6 presents the objectives of the performed heat simulations. The analysis will be carried out with regard to the aspects mentioned there.

1. Influence of the bellow length and a possible adjustment of it to reduce heat transfer:

An initially independent consideration of the chimney in simulation 1 showed a large thermal resistance of the bellows. Although the height of the bellow equals only 21 % of the chimney height, 64 % of the total temperature difference (296 K) dropped there. By adding static GHe in simulation 3, this influence of the thermal resistance was already reduced. The temperature drop reduced to 40 %. Simulation 5 also took the VCL and HTS into account. The temperature drop at the bellow reduced to 34%. It can thus be concluded that a longer bellow than the one present at the cryostat would improve the thermal situation, but much less than initially assumed in simulation 1. The solid heat conduction in the chimney would be reduced by the increased total thermal resistance of the chimney. This is due to the ratio of the compressed to the outstretched length of the chimney and its thin wall thickness.

2. Temperature distribution at the outer chimney wall in the upper section and a possible reversal of the net direction of radiation as compared to the intended direction by design:

All simulations indicate a clear reversal of the net direction of radiation around the chimneys. The radiation shield at 50 K encloses most of their height. It ends at $x = 117$ mm. In comparison, the beginning of the bellows is further down at $x = 175$ mm (see also Figure 3.1 on p.16). Simulation 5 determined the position at which the chimney temperature is 50 K to $x = 643$ mm. This is also influenced by the boundary condition $T_{\mathrm{VCL\ bottom\ surface}} = 50$ K which is at $x = 559$ mm. The chimneys would be warmer than the radiation shields surrounding them in the range $117\ \mathrm{mm} \leq x < 643$ mm. Looking at the service tubes, this range even increases. A simulation performed for the service tubes equal to simulation 3 determined the 50 K level at $x = 730$ mm. It therefore below the 50 K level of the chimneys.

It can be concluded that in the current constellation, for $117\ \mathrm{mm} \leq x < 643$ mm, the shields do not radiate to the He-space as intended, but vice versa. This has two effects:

1) Increase in heat radiation onto the radiation shields: The radiation from the chimneys and service tubes onto the radiation shields increases their incoming heat load. They consume additional GHe, which would be available for cooling the VCL instead. However, it should be noted that chapter 4.2.1.1 on p.34 determined the heat radiation with 28 MLI layers from 300 K to 50 K to be only 0.348 W m^{-2}. The chimney has a temperature of > 50 K for $x > 643$ mm, especially on the top. The surface area of the shield surrounding the chimneys and service tubes above $x = 643$ mm is ~1.93 m^2. To obtain the additional radiative heat flow from the He-space to the shields one would need to integrate the chimney temperature along the height. The heat flux would certainly drop well below 0.348 W m^{-2}. The resulting increase in heat radiation onto the radiation shields might be irrelevant regarding the GHe availability.

2) Cooling of the chimneys and service tubes in the section $117\ \mathrm{mm} \leq x < 643$ mm resp. $117\ \mathrm{mm} \leq x < 730$ mm: This effect could possibly increase the thermal efficiency. The chimneys and service tubes are cooled because they radiate onto the shields in this area. As discussed above, only a relatively small amount of heat exchange takes place when using MLI. However, if

the MLI would be removed in the area $117\ \mathrm{mm} \leq x < 643\ \mathrm{mm}$, this cooling effect could be increased. Consequently, especially the upper part of the chimney would radiate heat to the shields. This would reduce the conductive heat flow in the chimney and thus increase the thermal efficiency of the cryostat.

3. General influence of the VCL and HTS on the thermal conditions in the chimney:

A comparison of simulation 2 and 3 in Figure 4.11 showed that the GHe and chimney temperature converged to approximately an arithmetic mean value of both. In simulation 5, the GHe and chimney temperatures then converged strongly to the VCL temperature. This suggests that the dominant force for the temperature distribution and the resulting heat flows in the system is the VCL. This is also the most difficult to simulate due to the internal forced convection. The model with 8 sections showed only small oscillations of the VCL temperature due to T_{GHe}. However, the linear progression that resulted in simulation 5 is most likely derived from the assumption that $T_{\mathrm{GHe},i}$ of the individual 8 sections is linear to length.

Due to the dominance of VCL convection for the temperature distribution one must always consider the results with knowledge of the boundary conditions used from chapter 4.6.1 ($\dot{\omega}_{\mathrm{VCL}}$, $\dot{m}_{\mathrm{VCL}}$, α_{m} and $T_{\mathrm{VCL\ bottom\ surface}}$).

4. Determination of the VCL bottom temperature:

A separate determination of $T_{\mathrm{VCL\ bottom\ surface}}$ was not possible with the simulation presented here. Instead, the predefined value from experiments of ALPHA and the AMI engineering department of 50 K was used.

5. Possible adjustment of the baffle separation distances and baffles inside service tubes:

The results from chapter 4.6.5 indicate that the baffle distance in the upper chimney section is sufficient with a relatively low heat transfer coefficient of $\alpha_{01} \approx 4\ \mathrm{W\,m^{-2}\,K^{-1}}$ and $\alpha_{34} \approx 7\ \mathrm{W\,m^{-2}\,K^{-1}}$. These results are valid with $\Delta T \ll T_*$. In contrast the heat transfer coefficient between the two lowest baffles might be higher with $\alpha_{89} \approx 27\ \mathrm{W\,m^{-2}\,K^{-1}}$. Although this value is unreliable (ΔT not $\ll T_*$, the temperature dependence of the material properties would have to be considered for a precise result), it can be assumed that the baffle distance here might be too large. It is with $122\ \mathrm{mm}$ about $50\ \mathrm{mm}$ larger than the distance between the upper baffles. This causes a stronger convection.

Additionally, the analysis of possible free convection in the service tubes lead to $\alpha_{\mathrm{serv}} \approx 145\ \mathrm{W\,m^{-2}\,K^{-1}}$. One must mention again the unreliability of the result due to ΔT not $\ll T_*$. However, adding baffles into the otherwise empty service tubes should eventually be considered. This would be possible for about four of the seven service tubes (assuming two are used as recovery exit and one is used for the LHe insertion through the stinger).

6. Influence of radiation from the lowest baffle directly into the LHe:

Simulation 5 showed a temperature of the lowest baffle of $T = 16$ K. Radiation at this cryogenic temperature into the LHe resp. the He-box enclosing the LHe is negligible.

4.7 Optimum temperature of the radiation shields and influence of the MLI

This chapter presents the total net heat flow of the radiation shields $\dot{Q}_{\mathrm{b\ tot\ net}}$ from all determined results and discuss an optimum radiation shield temperature T_{b}. Finally, a possible removal of the MLI between shell 'b' and 'c' will be discussed.

Table 4.11. Summary of all ingoing and outgoing heat flows of the radiation shields.

$\dot{Q}_{\mathrm{gas\ cond\ MLI\ ab}}$	$\dot{Q}_{\mathrm{gas\ cond\ MLI\ bc}}$	$\dot{Q}_{\mathrm{rad\ ab,iter}}$	$\dot{Q}_{\mathrm{rad\ bc}}$	$\dot{Q}_{\mathrm{MLI\ cond\ ab}}$	$\dot{Q}_{\mathrm{MLI\ cond\ bc}}$	$\dot{Q}_{\mathrm{cond\ cryo-s\ ab}}$	$\dot{Q}_{\mathrm{cond\ tail\ stands\ ab}}$
0.07 W	0.07 W	2.40 W	0.001 W	1.76 W	0.17 W	1.52 W	5.36 W
In	Out	In	Out	In	Out	In	In

The total net heat flow of the radiation shields $\dot{Q}_{\mathrm{b\ tot\ net}}$ is given as the sum of the ingoing and outgoing heat flows presented in Table 4.11. We consider ingoing heat flows to be positive and outgoing to be negative. This leads to $\dot{Q}_{\mathrm{b\ tot\ net}} \approx 10.9$ W.

With Equation (3.18) on p.28, the LHe volume flow that needs to evaporate to cool the radiation shields to a steady state temperature of $T_{\mathrm{b}} = 50$ K is given by

$$\dot{V}_{\mathrm{b}}^{\mathrm{liq}} = \dot{V}_{\mathrm{per\ W}}^{\mathrm{liq}} \cdot \dot{Q}_{\mathrm{b\ tot\ net}} \approx 1.28\ \mathrm{L\ h^{-1}} \tag{4.61}$$

4.7.1 Optimum radiation shield temperature

The radiation shield temperature depends on the power and mass balances presented in chapter 3.8.5. It can be increased or decreased by adjusting the cooling mass flow with the valves at the shield tube outlets. On the one hand, a very low temperature of the radiation shields reduces the radiative and conductive heat transfer through MLI from shell 'b' to 'c'. This has a positive effect on the thermal efficiency. On the other hand, there are two disadvantages: the mass flow required to cool the shields increases with less GHe availability for the VCL cooling and the total heat transfer onto the shields themselves also increases. Depending on the demand and availability of cooling gas, an optimal temperature of the shields establishes. It is balanced between an acceptable cooling mass flow and the heat flow from the radiation shields to the He-space.

The influence of the radiation shield temperature T_{b} on the heat transfer through MLI is presented in Figure 4.15 as the black solid line. Additionally, the blue dashed line shows the required LHe volume flow to cool the radiation shields per total ingoing watt on the shields $\dot{V}_{\mathrm{per\ W}}^{\mathrm{liq}}$. It is a function of the enthalpy difference $\Delta h_{4\ \mathrm{K} \rightarrow T_{\mathrm{b}}}^{\mathrm{g}}$ and proportional to ${T_{\mathrm{b}}}^{-1}$ for ideal gases. The required volume flow was determined according to Equation (3.17) on p. 28 and the NIST webbook data [39] for GHe at 1100 mbar. $\dot{V}_{\mathrm{per\ W}}^{\mathrm{liq}}$ refers to the liquid volume to show how much LHe needs to vaporise regarding a sufficient shield cooling rather the gas volume of the cooling gas. In Figure 4.15, a change in $\dot{Q}_{\mathrm{b\ tot\ net}}$ with changing T_{b} is not visible. This is because the graph presents the volume flow per ingoing watt and not per total ingoing heat flow. In Figure 4.15, the heat flux due to MLI conduction by Ross [13] considers an MLI conductance of

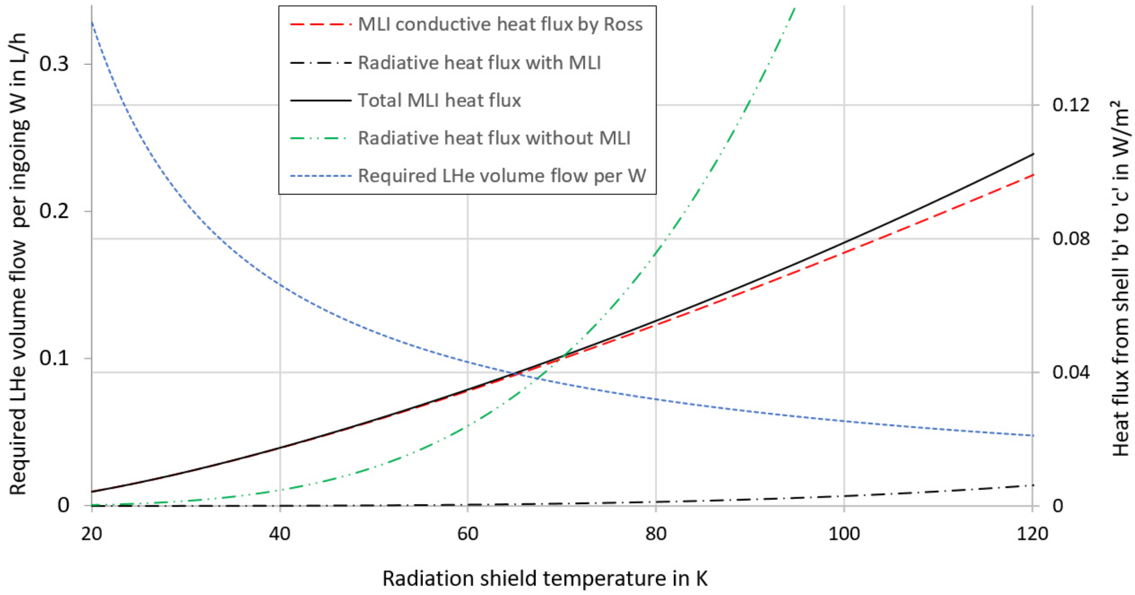

Figure 4.15. Required LHe volume flow per ingoing W in L h^{-1} for 1100 mbar and radiative heat flux from shell 'b' to 'c' in W over radiation shield temperature in K.

$$k_o \cdot \kappa(T) \approx 6.4924 \cdot \ln((T_b - 4.3\ \mathrm{K})/2) - 11.393. \tag{4.62}$$

This equation was generated with MSE by manually entering the values from Figure 2.8 on p.12 and generating a trendline. With the proportionality of $\dot{V}^{\mathrm{liq}}_{\mathrm{per\ W}}$ to $\Delta h^{\mathrm{g}}_{4\,\mathrm{K}\rightarrow T_b}{}^{-1}$ for real gases, $\dot{V}^{\mathrm{liq}}_{\mathrm{per\ W}}$ increases strongly for very low radiation shield temperatures. Figure 4.15 indicates that a decrease of T_b from 50 K to 30 K would increase $\dot{V}^{\mathrm{liq}}_{\mathrm{per\ W}}$ by a factor of about 1.8. On the other hand, an increase of T_b from 50 K to 70 K, would reduce $\dot{V}^{\mathrm{liq}}_{\mathrm{per\ W}}$ by a factor of 1.4.

Considering $\dot{Q}_{\mathrm{b\ tot\ net}} \approx 10.9$ W, it can be deduced that a radiation shield temperature of 50 K is feasible for the cryostat with $\dot{V}^{\mathrm{liq}}_{\mathrm{b}}(T_b = 50\mathrm{K}) \approx 1.28\mathrm{Lh}^{-1}$. The amount of LHe evaporating is much higher if one considers the target value of $\dot{V}^{\mathrm{liq}}_{\max} \approx 20$ L h^{-1}. However, the VCL consumes a large amount of helium. By Equation (4.51) and (4.53) it can be determined to $\dot{V}^{\mathrm{liq}}_{\mathrm{VCL}} \approx 18.9$ L h^{-1}. In case a shortage of GHe occurs during the operation of the cryostat, e.g. due to a high $\dot{V}^{\mathrm{liq}}_{\mathrm{VCL}}$, the following should be considered:

Investigations in chapter 4 have shown that heat transfer through MLI from shell 'b' to 'c' plays an exceptionally minor role at $T_b = 50$ K. The total heat transfer through MLI $\dot{Q}_{\mathrm{MLI\ tot\ bc}}$ is only 0.2 W (considering $A_{\mathrm{b\ tot}} = 7.4$ m^2, see Table 3.3 on p.25). Other heat input from shell 'b' to 'c' does not occur. It can therefore be recommended that T_b could be increased without any relevant impact on the thermal efficiency. By Figure 4.15, $\dot{Q}_{\mathrm{MLI\ tot\ bc}}$ at $T_b = 80$ K would still only be around 0.4 W (considering $A_{\mathrm{b\ tot}}$). Taking into account $A_{\mathrm{b\ tot\ LHe}} = 3.7$ m^2, the value would even decrease to ~0.2 W that evaporates LHe. At $T_b = 100$ K, $\dot{Q}_{\mathrm{MLI\ tot\ bc}} \approx 0.3$ W with $A_{\mathrm{b\ tot\ LHe}}$.

In summary it can be said that T_b should be kept as low as the availability of GHe allows. It is thermally more efficient to use available GHe for a low T_b such as 50 K instead of releasing excess gas through the recovery line. In case of GHe shortage, an increase up to 100 K is advisable.

4.7.2 Possible removal of the MLI between shell ‘b’ and ‘c’

Figure 4.15 shows that the total heat transfer through MLI from shell ‘b’ to ‘c’ $\dot{Q}_{\mathrm{MLI\ tot\ bc}}$ is mainly dependent on the MLI conduction. It increases about linearly with T_{b} (not completely linear due to $k_{\mathrm{o}} \cdot \kappa(T)$). Equation (4.8) on p.35 presents the radiative heat flow without using MLI $\dot{Q}_{\mathrm{rad\ bc\ without\ MLI}}$ to ~ 0.09 W for $T_{\mathrm{b}} = 50$ K. At this temperature, the MLI conduction by Ross [13] in Equation (4.30) on p.45 $\dot{Q}_{\mathrm{MLI\ cond\ bc}}$ is ~ 0.17 W. This leads to the conclusion that a removal of the MLI at such a low radiation shield temperature might decrease the total heat load slightly by 0.06 W. This low reduction would certainly not have a noticeable influence on the thermal efficiency of the cryostat. In comparison, the radiative heat load during the cool down and warm up would increase massively. One can see this in the strongly increasing radiative heat flux without MLI by temperature in Figure 4.15.

To sum up it can be said that the MLI does not have a positive effect on the thermal efficiency during steady state and might even increase the total heat load from shell ‘b’ to ‘c’ slightly. However, a removal is not advisable as this increase is too little and the cool down situation would have a large disadvantage. Regarding the MLI cost of 12020 € (shell 'a' to 'b' and 'b' to 'c'), it can be assumed that the share of the MLI from shell 'b' to 'c' could be around 4000 €. The cost-benefit ratio could thus be assessed as poor.

4.8 TAOs in the ALPHA-g cryostat

In cold tests on 8th of April and 2nd of June 2021, pressure oscillations in He-space with a maximum amplitude of about 25 mbar had occurred. Visible and audible vibrations of the recovery line and the gas manifold were observed as well. The following chapter will discuss the circumstances and outcomes of these events. Theoretical background about TAOs can be found in chapter 2.4 on p.13.

4.8.1 TAOs in the recovery line

The recovery line is the main risk for TAOs in the ALPHA-g cryostat. The evaporated GHe is used to cool the copper shields and the HTS. However, in some situations, e.g., when the valves for the shield tubes and the HTS are closed, the GHe might exit the cryostat at temperatures close to the boiling temperature. During the cold test on 8th of April 2021, all of the evaporated GHe went into the recovery line directly - the apparatus had run without radiation shields or HTS. As the shields had not been implemented that time, the ‘A’ heat in-flows and the $\dot{m}_{\mathrm{GHe}}$ had been larger than it will be in the final run. However, TOAs had also occurred on 2nd of June 2021 during a cold test with cold shields (but without HTS). The TAOs had been stopped by opening the manual bypass valve on the recovery manifold. The recovery line no longer had a closed end and the gas vibrations had ceased.

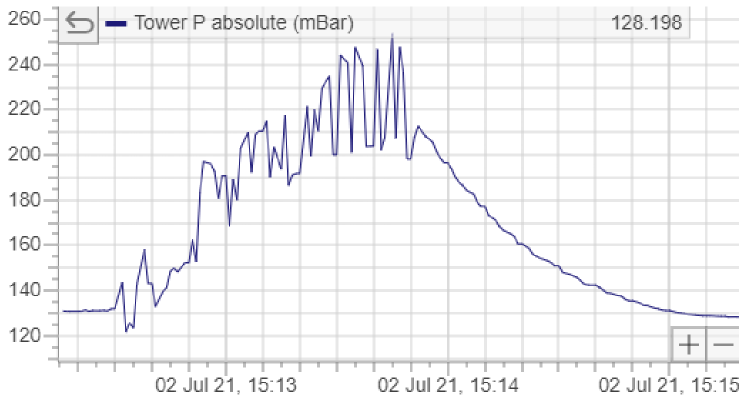

Figure 4.16. Tower pressure during the cold test on 2nd June 2021 – TAOs occurred which increased the pressure from 130 mbar to 253 mbar in 80 s.

During the cold tests, the temporary recovery line was made of flexible KF40 metal hoses with a total length from the cryostat to the manifold with safety valves of ~15 m. The TAO stability maps in Figure 2.10 on p.14 are valid for tubes of 1 m length. For longer tubes, the tube radius r has to be reduced to r' with the total tube length L in m. Using a KF radius of $r = 20$ mm, the reduced radius decreases about a factor of 4 by Equation (2.34) to $r' = 20\,\text{mm} \cdot 15^{-0.5} \approx 5.2$ mm.

One can see in Figure 2.10 that the result indicates oscillations for $\varphi > 20$ and $\xi = 1$. This could occur for a ratio of hot to cold temperature by Equation (2.32) with 200 K to 10 K and a linear temperature gradient by Equation (2.33). Following Figure 2.10, the TAO event in April 2021 would become safer for a shorter recovery line which will be the case in the final assembly. The ALPHA-g platform will be much closer to the gas manifold then.

It is necessary to mention that the "studies described above [in Figure 2.10] used a very ideal case and thus even if you are in the stable regions you may find TAOs occurring" [4, p. 41]. For additional safety measures of the ALPHA-g cryostat, an appropriate thermal insulation of the recovery line should be implemented. Secondary, closed tubes should be avoided [20]. Thirdly, an acoustic impedance, such as a Helmholtz resonator, could be added on the recovery line to damp oscillations [22, p. 76].

4.8.2 TAOs in the service tubes

The large temperature gradient in the service tubes from 300 K to near boiling temperature of helium at 4 K requires an investigation about possible thermo acoustic oscillations as well. The tubes are open at the lower end where they are connected to the He-box and closed at the upper end. General circumstances for a possible occurrence of this effect are therefore given.

The exact gas temperature at the ceiling of the He-box is uncertain, as already discussed in chapter 4.3.1. It can be estimated to $4\,\text{K} \leq T_\text{c} \leq 12\,\text{K}$ which would lead to $\varphi_\text{min} = 300\,\text{K} \cdot 12^{-1}\,\text{K}^{-1} = 25$ and $\varphi_\text{max} = 300\,\text{K} \cdot 4.2^{-1}\,\text{K}^{-1} \approx 71$. Considering a linear temperature gradient in the gas, $L_\text{h} = L_\text{c}$ and $\xi = 1$ by Equation (2.33). Furthermore, $r' = 38\,\text{mm} \cdot 0.845^{-0.5} \approx 41$ mm, which finally gives an approximation of the TAO risk inside the service tubes. The present data point is outside the range of Figure 2.10. However, if the stable and unstable zones were to be enlarged,

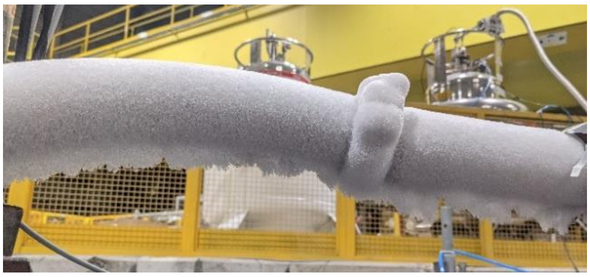

Figure 4.17. Frozen GHe recovery line during a cold test in December 2020. The desublimated ice indicates a cold GHe temperature.

a stability in the data point could be estimated. One could argue that additional baffles in the service tubes would not be necessary regarding TAOs.

4.8.3 TAOs in the shield tubes

The long and thin shield tubes are usually open at both ends to allow GHe mass flow going through and cool the shields. However, if the valve at the outlet is closed, the tube is open at the inlet but closed at the outlet - TAOs might occur. The reduced radius becomes shorter for longer tubes. The total tube length is ~ 7 to ~ 10 m (unprecise length due do manually bend tubes). The main front shield, the tail shields and the bottom plate shield could be at risk for TAOs at $r'_{\mathrm{min}} \approx 4.0\ \mathrm{mm} \cdot 10^{-0.5} \approx 1.3$ mm. Looking at one can see that up to $\varphi_{\mathrm{min}} \approx 6.5$ (with $\xi = 1$) there is no possibility of TAOs in the ideal case of the experiment used for the data. Considering $T_{\mathrm{h}} = 50$ K and $T_{\mathrm{c}} \approx 12$ K, as during the cold test on 2nd July 2021 in steady state, $\varphi \approx 4.2$ would be too low for the occurrence of TAOs. Nevertheless, if the VCL consumes much GHe, the shields could only be cooled to a higher temperature and then endanger TAOs at $\sim T_{\mathrm{h}} \geq 12\ \mathrm{K} \cdot 6.5$ $= 78$ K for a closed valve position.

4.8.4 TAOs in the chimneys

Additional possible components for TAOs might be the chimneys. Their much larger inner diameter $r' = 200\ \mathrm{mm} \cdot 0.845^{-0.5} \approx 217$ mm leads with the same φ_{min} and φ_{max} to a very stable condition by Figure 2.10. Reason is the large gas inertia that prevents the effect of TAOs [4, p. 40].

5 Summary and outlook

The thesis presented various calculations of heat flows in independent systems. Subsequently some of these individual systems were combined in simulations with ANSYS workbench. The objective was to evaluate the thermal efficiency and find thermal weak points of the cryostat. A summary of all determined heat flows is shown in Table 5.1.

5.1 Heat transfer into shell ‘c’

The determined results of the analytic calculations show a total heat load entering helium-space $\dot{Q}_{\mathrm{c\,tot}}$ of ~ 19 W. If treated as an ‘A’ heat-in flow, it would lead to a LHe consumption of $\sim 27\ \mathrm{L\,h^{-1}}$. Heat conduction in the chimneys has the largest influence with ~8 W. Simulation 3 shows an increase in $\dot{Q}_{\mathrm{c\,tot}}$ to ~ 27 W. It considers interaction of heat conduction in the chimneys and service tubes with the gas inside. Again, the heat conduction in the chimneys influences the process the most with ~ 19 W. In both cases, static gas and no convection in the chimneys or service tubes is assumed. The values were determined without taking the VCL and HTS into account. The boundary conditions were a thermal steady-state with temperatures of 300 K on the HTS plate and 4 K on the helium-box ceiling.

The ratio of $\dot{Q}_{\mathrm{c\,tot\,A}}/\dot{Q}_{\mathrm{c\,tot\,B}}$ depends on the convective conditions of the GHe inside the cryostat, especially for the helium-box ceiling. It could not be specified in this thesis due to the complex interactions of the individual subsystems. However, a comparison of the theoretically determined values with the last cold test on 25th of August 2021 (performed without HTS) allows as estimation. The average LHe consumption during the warm-up was $23.8\ \mathrm{L\,h^{-1}}$ which corresponds to $\dot{Q}_{\mathrm{c\,tot\,A}} \approx 17$ W (cf. target value of $20\ \mathrm{L\,h^{-1}}$ with $\dot{Q}_{\mathrm{c\,tot\,A\,max}} \approx 14$ W). This gives $\dot{Q}_{\mathrm{c\,tot\,A}}/\dot{Q}_{\mathrm{c\,tot\,B}} \approx 90\ \%$ with respect to the analytic calculations and 63% with respect to simulation 3. During the cold test the transfer system revealed a key thermal weakness with an additional LHe consumption of $27\ \mathrm{L\,h^{-1}}$. However, it should be noted that the current transfer system will be replaced by a new one after the installation phase is completed.

Taking the VCL and HTS into account in simulation 5 resulted in a new configuration of heat flows. Here, $\dot{Q}_{\mathrm{c\,tot}}$ could be determined to ~ 29 W. Heat conduction in the HTS dominates the heat load with ~ 14 W. The heat conduction in the chimneys is about 8 W. A comparison with results from a cold test as described above cannot be made here as none was performed with the VCL and HTS by end of August 2021. Simulation 5 also assumed static gas and no convection in the chimneys or service tubes, but respected forced convection in the VCL. The boundary conditions are based on AMI's manufacturer's specification of a voltage drop of 100 mV or less per VCL with a total internal heat generation of 850 W. To ensure a successful cooling of this large power, the total GHe mass flow $\dot{m}_{\mathrm{VCL}}$ must be $\sim 0.655\ \mathrm{g\,s^{-1}}$ (considering 50 K as gas inlet temperature and 300 K as gas outlet temperature). It corresponds to a LHe volume flow of $18.9\ \mathrm{L\,h^{-1}}$ which must evaporate and be available for the VCL cooling. The forced convection in the VCL is laminar with a mean heat transfer coefficient of $\alpha_{\mathrm{m}} \approx 130\ \mathrm{W\,m^{-2}\,K^{-1}}$. In simulation 5 one has to take into account that the material composition and k_{HTS} could not be provided by AMI. The thermal conductivity has therefore been estimated from literature values. Accordingly, the results contain inaccuracies. Regarding $\dot{Q}_{\mathrm{c\,tot}}$, heat transfer through MLI (radiation and MLI

Table 5.1. Summary of all determined heat flows.

Method of determination	$\dot{Q}_{\text{b tot net}}$	$\dot{Q}_{\text{cond tail stands ab}}$	$\dot{Q}_{\text{MLI tot ab}}$	$\dot{Q}_{\text{c tot}}$	$\dot{Q}_{\text{cond chim}}$	$\dot{Q}_{\text{cond GHE chim}}$	$\dot{Q}_{\text{cond HTS}}$	$\dot{Q}_{\text{transfer system}}$
Analytic calculations	11 W	5.4 W	4.2 W	19 W	9 W	5 W	-	19 W
Simulation 3	-	-	-	27 W	19 W	4 W	-	-
Simulation 5	-	-	-	29 W	8 W	1 W	14 W	-

conduction) and free-molecular heat transfer can be seen as negligible with a sum of only ~0.2 W at an OVC pressure of $\leq 10^{-5}$ mbar. Although the MLI conduction dominates heat flow between shell 'b' and 'c', a removal of the MLI is not recommended. It would slightly improve the thermal efficiency in steady state by 0.06 W, but downgrade the conditions during the cool down and warm up. Heat conduction in the tail and cryo supports plays a minor role with a total of around 2.8 W.

The ANSYS workbench simulations showed that a longer bellow than the one used at the chimneys would improve the thermal efficiency, but much less than initially assumed. Due to the ratio of the compressed to the outstretched length of the chimney and its thin wall thickness the bellow acts as a thermal resistance. The simulations indicated a reversal of the net direction of radiation as compared to the intended direction by design from shell 'b' to 'c' around the chimneys. In the range of $117\text{ mm} \leq x < 643\text{ mm}$ (with $x = 0$ at the HTS plate) the shields do not radiate to the helium-space as expected, but vice versa. This increases heat radiation onto the radiation shields and therefore acts as slight cooling mechanism of the chimneys and service tubes. The results are strongly dependent on the boundary conditions at the VCL. Simulation 5 showed that the VCL temperature dominates the gas and chimney temperature, despite G-10 insulation. A realistic determination of $T_{\text{VCL bottom}}$ was not possible with the performed simulations. Instead, the predefined value from experiments of ALPHA and the AMI engineering department of 50 K was used.

Further analysis of the conditions in the chimney were carried out using the results of simulation 5. This indicated that the baffle distance in the upper chimney section is sufficient ($\alpha \approx 4\text{ W m}^{-2}\text{ K}^{-1}$ between the HTS plate and the first baffle). Between the two lowest baffles α might be higher with $\sim 27\text{ W m}^{-2}\text{ K}^{-1}$. The value is unreliable with the used calculation method but gives an estimation that the baffle distance here could be too large. In the service tubes α_{serv} is $\sim 150\text{ W m}^{-2}\text{ K}^{-1}$ (value also unreliable). It could be advised to use baffles here. Further, it was evaluated that radiation from the lowest chimney baffle into the LHe is negligible.

5.2 Heat transfer into shell 'b'

In comparison to the discussed $\dot{Q}_{\text{c tot}}$, the calculated net heat load onto the radiation shields $\dot{Q}_{\text{b tot net}}$ at a temperature of $T_{\text{b}} = 50$ K was determined to be ~11 W. The main cause is heat conduction in the tail stands (~5.4 W), MLI radiation (~2.4 W) and MLI conduction (~1.8 W). To cool the radiation shields sufficiently, a cooling gas flow is required equivalent to 1.28 L h^{-1} of LHe that evaporate. The target radiation shield temperature of $T_{\text{b}} = 50$ K was evaluated as feasible regarding the availability of GHe. However, it is not necessary concerning the thermal efficiency of the cryostat. Heat transfer from shell 'b' to 'c' only occurs through MLI. It would be acceptable at $T_{\text{b}} = 100$ K with ~0.3 W as total MLI 'A' heat-in flow. An increase of T_{b} will therefore be recommended in case the available cooling gas lacks or in case the VCL consume more cooling gas than presented here.

In the iterative determination of the radiative heat flux through MLI with $\varepsilon = f(T)$, algorithm method 1 was successful. The results of method 2 are considered unreliable because the difference of the individual heat fluxes did not converge to 0. Method 1 determined the radiative heat flux from shell ‘a’ to ‘b’ to $0.305\ \mathrm{W\,m^{-2}}$. The original hand calculation resulted in a slightly higher value of $0.348\ \mathrm{W\,m^{-2}}$. The influence of $\varepsilon = f(T)$ was thus less than initially expected which might call the time required to create the script of program into question.

An analysis of TAOs in the cryostat showed a clear risk at the current (temporary) recovery line. TAOs were observed in two cold tests in April and June 2021. A shortening and appropriate thermal insulation of the recovery line can reduce the risk. In service tubes, shield tubes or chimneys a risk of TAOs is not present.

5.3 Evaluation of the thermal efficiency

As mentioned in the introduction, a quantitative evaluation with the COP is not possible for a cryostat. Optimisation possibilities were found, but no important weak points. Outside the cryostat, the temperature transfer system is a clear weak point. The VCL consume $\sim 19\ \mathrm{L\,h^{-1}}$. The radiation shiels $\sim 1.3\ \mathrm{L\,h^{-1}}$. Both cooling systems can be provided with helium without additional boil-off. The LHe consumption in the final setup is around $25\ \mathrm{L\,h^{-1}}$ in the cryostat. This considers $\dot{Q}_{\mathrm{c\,tot}} \approx 29$ W from simulation 5 and $\dot{Q}_{\mathrm{c\,tot\,A}}/\dot{Q}_{\mathrm{c\,tot\,B}} \approx 63$ % from simulation 3.

5.4 Outlook

Further investigations following this thesis are recommended after measurements of the complete cryostat have been taken in the final run. If the LHe consumption and the GHe availability are known, the radiation shield temperature can possibly be increased. If $T_{\mathrm{VCL\,bottom}}$ is measured higher than 50 K, the boundary conditions in simulation 5 should be adjusted. In addition, a more detailed analysis of the convection inside the vapour should be carried out. Free convection can have a relevant influence on the thermal efficiency and may be reduced by additional measures such as adding baffles in the service tubes.

Bibliography

[1] So, Chukman; Fajans, Joel; Bertsche, William (2020): The ALPHA-g Antihydrogen Gravity Magnet System. In: *IEEE Trans. Appl. Supercond.* 30 (4), pp. 1–5.

[2] Kuhn, Philipp (2021): Assembly of the ALPHA-g cryostat. Karlsruhe: Hochschule Karlsruhe University of Applied Sciences, Course: Entwicklungsprojekt (MABB610) under Martin Jäckle, Summersemester 2021.

[3] Arnemann, Michael (2020): Grundlagen der Wärmeübertragung: Begleitmaterial Vorlesung Sommersemester 2020. Karlsruhe: Hochschule Karlsruhe - Technik und Wirtschaft.

[4] Weisend II, J. G. (2016): Cryostat Design - Case Studies, Principles and Engineering. Cham: Springer International Publishing (International Cryogenics Monograph Series).

[5] Reiss, Harald (2019): K6 Wärmestrahlung - Superisolierungen. In: Peter Stephan, Stephan Kabelac, Matthias Kind, Dieter Mewes, Karlheinz Schaber und Thomas Wetzel (Hg.): VDI-Wärmeatlas. Berlin, Heidelberg: Springer Berlin Heidelberg (Springer Reference Technik), pp. 1269–1350.

[6] Reiss, Harald (1988): Radiative Transfer in Nontransparent, Dispersed Media. Berlin, Heidelberg: Springer Berlin Heidelberg (113).

[7] Barron, Randall F. (1999): Cryogenic heat transfer. Philadelphia, Pa: Taylor and Francis (Series in chemical and mechanical engineering).

[8] Maxwell, J. C. (1860): V. Illustrations of the dynamical theory of gases. —Part I. On the motions and collisions of perfectly elastic spheres. In: *The London, Edinburgh, and Dublin Philosophical Magazine and Journal of Science* 19 (124), pp. 19–32.

[9] Kennard, Earle H. (1938): The Kinetic Theory of Gases. With an Introduction to Statistical Mechanics. 1st ed. Pp. xiv + 483. In: *J. Chem. Technol. Biotechnol.* 57 (39), p. 901.

[10] Moisan, Michel; Pelletier, Jacques (2012): Physics of Collisional Plasmas. Dordrecht: Springer Netherlands.

[11] Jousten, Karl (2018): Handbuch Vakuumtechnik. Wiesbaden: Springer Fachmedien Wiesbaden.

[12] Lemmon, Eric W.; Jacobsen, Richard T.; Penoncello, Steven G.; Friend, Daniel G. (2000): Thermodynamic Properties of Air and Mixtures of Nitrogen, Argon, and Oxygen From 60 to 2000 K at Pressures to 2000 MPa. In: *Journal of Physical and Chemical Reference Data* 29 (3), pp. 331–385.

[13] Ross, R. G. (2015): Quantifying MLI Thermal Conduction in Cryogenic Applications from Experimental Data. In: *IOP Conf. Ser.: Mater. Sci. Eng.* 101 (1): 012017.

[14] Stephan, Peter (2019): B2 Grundlagen der Berechnungsmethoden für Wärmeleitung, konvektiven Wärmeübergang und Wärmestrahlung. In: Peter Stephan, Stephan Kabelac, Matthias Kind, Dieter Mewes, Karlheinz Schaber und Thomas Wetzel (Hg.): VDI-Wärmeatlas. Berlin, Heidelberg: Springer Berlin Heidelberg (Springer Reference Technik), pp. 23–36.

[15] Kabelac, Stephan; Vortmeyer, Dieter (2019): K1 Wärmestrahlung technischer Oberflächen. In: Peter Stephan, Stephan Kabelac, Matthias Kind, Dieter Mewes, Karlheinz Schaber und Thomas Wetzel (Hg.): VDI-Wärmeatlas. Berlin, Heidelberg: Springer Berlin Heidelberg (Springer Reference Technik), pp. 1183–1199.

[16] Hanzelka, P.; Kralik, T.; Srnka, A. (2005): Low temperature radiative properties of materials used in cryogenics. In: *Cryogenics* 45 (8), pp. 529–536.

[17] Laa, C.; Hirschl, C.; Stipsitz, J.; Weisend, J. G.; Barclay, John; Breon, Susan; Demko, Jonathan; DiPirro, Michael; Kelley, J. Patrick; Kittel, Peter; Klebaner, Arkadiy; Zeller, Al; Zagarola, Mark; van Sciver, Steven; Rowe, Andrew; Pfotenhauer, John; Peterson, Tom; Lock, Jennifer (2008): HEAT FLOW MEASUREMENT AND ANALYSIS OF THERMAL VACUUM INSULATION. In: J. G. Weisend et al. (Hg.): AIP Conference Proceedings. ADVANCES IN CRYOGENIC ENGINEERING: Transactions of the Cryogenic Engineering Conference - CEC, Vol. 52. Chattanooga (Tennessee), 16–20 July 2007: AIP, pp. 1351–1358.

[18] Lehmann, W. (2000): Superisolation (SI) – Deren Qualität und Degradierung bei Anwendungen in der Kryotechnik. In: Deutscher Kälte- und Klimatechnischer Verein e.V. (DKV): DKV-Tagungsbericht. Bremen, 27. Jahrg., Band I.

[19] Johnson, W. L.; van Dresar, N. T.; Chato, D. J.; Demers, J. R. (2017): Transmissivity testing of multilayer insulation at cryogenic temperatures. In: *Cryogenics* 86, pp. 70–79.

[20] Putselyk, S. (2020): Thermal Acoustic Oscillations: Short Review and Countermeasures. In: *IOP Conf. Ser.: Mater. Sci. Eng.* 755 (012080).

[21] Haynes, William M. (2015): CRC Handbook of Chemistry and Physics, 95th Edition. 12 Properties of Selected Materials at Cryogenic Temperatures. 95th ed. Hoboken: CRC Press.

[22] Bostock, Thomas D.; Scurlock, Ralph G. (2019): Low-Loss Storage and Handling of Cryogenic Liquids. Cham: Springer International Publishing.

[23] Kramer, David (2020): Helium shortage has ended, at least for now. In: *Phys. Today* 2020 (2), 0605a. (Accessed online 16.06.2021): https://physicstoday.scitation.org/do/10.1063/PT.6.2.20200605a/full/.

[24] Arp, Vincent D.; Mccarty, Robert D.; Friend, Daniel G. (1989): Thermophysical properties of Helium-4 from 08 to 1500 K with pressures to 2000 MPa. Washington: NIST, Technical Note 1334, U.S. GOVERNMENT PRINTING OFFICE.

[25] Singh, Vijay P.; Singh, Pratap; Haritashya, Umesh K. (2011): Encyclopedia of Snow, Ice and Glaciers. Dordrecht: Springer Netherlands.

[26] Gistau Baguer, Guy (2020): Cryogenic Helium Refrigeration for Middle and Large Powers. Cham: Springer International Publishing.

[27] Dittmar, N.; Haberstroh, Ch.; Hesse, U.; Krzyzowski, M. (2016): Characterisation and optimisation of flexible transfer lines for liquid helium. Part I: Experimental results. In: *Cryogenics* 75, pp. 6–12.

[28] Merziger, Gerhard; Mühlbach, Günter; Wille, Detlef; Wirth, Thomas (2010): Formeln + Hilfen höhere Mathematik. 6th ed. Barsinghausen: Binomi-Verlag.

[29] Çengel, Yunus A.; Boles, Michael A. (2006): Thermodynamics. An engineering approach. 5. ed. Boston, Mass.: McGraw-Hill Higher Education (McGraw-Hill series in mechanical engineering).

[30] Arnemann, Michael (2018): Thermodynamik - Begleittext zur Vorlesung MABB321 bzw. MECB441 Wintersemester 2018. Karlsruhe: Hochschule Karlsruhue - Technik und Wirtschaft.

[31] Domen, Steve R. (1991): Emissivity of aluminized mylar. In: *International Journal of Radiation Applications and Instrumentation. Part C. Radiation Physics and Chemistry* 37 (2), pp. 199–201.

[32] Brandt, Daniel (2007): CAS - CERN Accelerator School and ALBA Synchrotron Light Facility: Course on Vacuum in Accelerators. Platja d'Aro, Geneva: CERN.

[33] Huber, M.; Harvey, A (2011): Viscosity of Gases. Boulder, Colorado: NIST - Applied Chemicals and Materials Division. Accessed online (20.08.2021): https://tsapps.nist.gov/publication/get_pdf.cfm?pub_id=907539.

[34] McKeen, Laurence W. (2017): Film properties of plastics and elastomers. 6 – Polyester. Oxford: William Andrew (PDL handbook series), pp. 105-145.

[35] Duthil, P. (2014): Material Properties at Low Temperature. In: CAS – CERN Accelerator School: Superconductivity for Accelerators, Erice, Geneva: CERN. pp. 77-95.

[36] Parma, V. (2014): Material Properties at Low Temperature. In: CAS – CERN Accelerator School: Superconductivity for Accelerators, Erice, Geneva: CERN. pp. 353-399.

[37] NIST (Accessed online 14.07.2021): Material Measurement Laboratory / Applied Chemicals and Materials Division. https://trc.nist.gov/cryogenics/materials/G-10%20CR%20Fiberglass%20Epoxy/G10CRFiberglassEpoxy_rev.htm.

[38] Kooi, J. W. (Accessed online 14.07.2021): Caltech Submillimeter Observatory. 03.03.2001: http://www.submm.caltech.edu/cso/receivers/thermal/thermal_integral_g10.pdf.

[39] NIST webbook (Accessed online 29.07.2021): Thermophysical Properties of Fluid Systems. https://webbook.nist.gov/chemistry/fluid/.

[40] Fradkov, A. B.; Ginodman, V. B. (1970): Flexible siphons for transferring liquid helium. In: *Cryogenics* 10 (6), pp. 507–508.

[41] AS Scientific Products Ltd (Accessed online 15.07.2021): Flexible Insulated Vacuum Line. http://www.asscientific.com/products/flexible-insulated-vacuum-line.html.

[42] American Magnetics Inc. (Accessed online 23.08.2021): Current leads for Cryogenic Systems. http://www.americanmagnetics.com/datasheets/current_leads.pdf.

[43] Gnielinski, Volker (2019): G2 Wärmeübertragung bei erzwungener Konvektion: Konzentrischer Ringspalt und ebener Spalt. In: Peter Stephan, Stephan Kabelac, Matthias Kind, Dieter Mewes, Karlheinz Schaber und Thomas Wetzel (Hg.): VDI-Wärmeatlas. Berlin, Heidelberg: Springer Berlin Heidelberg (Springer Reference Technik), pp. 813–822.

[44] Stephan, K. (1962): Wärmeübergang bei turbulenter und bei laminarer Strömung in Ringspalten. In: *Chemie Ingenieur Technik* 34 (3), pp. 207-212.

[45] Naito, Tomoyuki; Fujishiro, Hiroyuki; Yamada, Yuichi (2018): Thermal Conductivity and Dilatation of Bi-2223/Ag (DI-BSCCO) Superconducting Wire Laminated With Various Thin Alloy Tapes. In: *IEEE Trans. Appl. Supercond.* 28 (4), pp. 1–4.

[46] Putti, M.; Ferdeghini, C.; Grasso, G.; Manca, A.; Siri, A. S.; Goldacker, W. (2000): Thermal conductivity of BSCCO(2223) tapes with different metallic sheats. In: *Physica C: Superconductivity* 341-348, pp. 2585–2586.

[47] Thess, André; Kaiser, Robert (2019): F1 Wärmeübertragung bei freier Konvektion: Grundlagen. In: Peter Stephan, Stephan Kabelac, Matthias Kind, Dieter Mewes, Karlheinz Schaber und Thomas Wetzel (Hg.): VDI-Wärmeatlas. Berlin, Heidelberg: Springer Berlin Heidelberg (Springer Reference Technik), pp. 759–762.

[48] Thess, André; Kaiser, Robert (2019): F3 Wärmeübertragung bei freier Konvektion: Innenströmungen. In: Peter Stephan, Stephan Kabelac, Matthias Kind, Dieter Mewes, Karlheinz Schaber und Thomas Wetzel (Hg.): VDI-Wärmeatlas. Berlin, Heidelberg: Springer Berlin Heidelberg (Springer Reference Technik), pp. 773–783.

List of tables

Appendix:

Table of figures

Appendix:

Appendix

A. Material properties

Table A.1. Emissive coefficient of Hutchinson MLI type IR305 PGN900601 OFRU200103.

Surface temperature (°C)	Total near-normal emissivity					
	Measured				Mean value	Uncertainty*
	Sample 1	Sample 2	Sample 3	Sample 4		
-100.0	0.014	0.031	0.032	0.031	0.027	0.048
-75.0	0.016	0.032	0.034	0.033	0.029	0.046
-50.0	0.019	0.034	0.036	0.036	0.031	0.045
-25.0	0.021	0.035	0.039	0.038	0.033	0.044
0.0	0.023	0.037	0.041	0.040	0.035	0.043
20.0	0.025	0.038	0.042	0.041	0.037	0.042
50.0	0.027	0.040	0.044	0.043	0.039	0.041
100.0	0.031	0.043	0.047	0.046	0.042	0.039
150.0	0.033	0.045	0.049	0.049	0.044	0.038
200.0	0.035	0.046	0.051	0.050	0.046	0.037
300.0	0.038	0.049	0.053	0.053	0.048	0.035
400.0	0.040	0.050	0.054	0.054	0.050	0.034

Surface temperature (°C)	Total hemispherical emissivity					
	Measured				Mean value	Uncertainty*
	Sample 1	Sample 2	Sample 3	Sample 4		
-100.0	0.017	0.036	0.038	0.037	0.032	0.055
-75.0	0.019	0.038	0.040	0.039	0.034	0.053
-50.0	0.022	0.039	0.043	0.042	0.036	0.052
-25.0	0.025	0.041	0.045	0.044	0.039	0.050
0.0	0.027	0.043	0.048	0.046	0.041	0.049
20.0	0.029	0.045	0.049	0.048	0.043	0.048
50.0	0.032	0.047	0.052	0.051	0.045	0.047
100.0	0.036	0.050	0.055	0.054	0.049	0.045
150.0	0.039	0.052	0.057	0.057	0.051	0.043
200.0	0.041	0.054	0.059	0.059	0.053	0.042
300.0	0.045	0.057	0.061	0.061	0.056	0.040
400.0	0.047	0.059	0.063	0.063	0.058	0.039

Surface temperature (°C)	Solar absorptance					
	Measured				Mean value	Uncertainty*
	Sample 1	Sample 2	Sample 3	Sample 4		
23	0.092	0.088	0.089	0.091	0.090	0.020

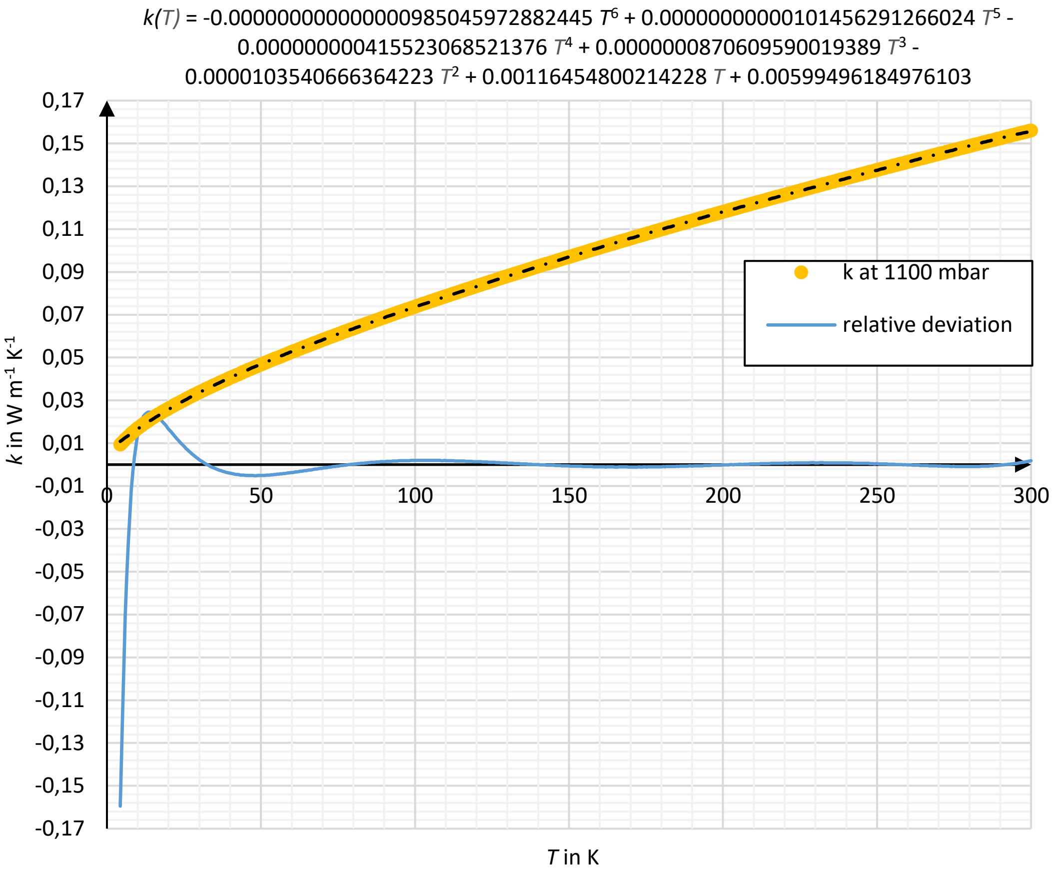

Figure A.1. Thermal conductivity of gaseous helium at 1100 mbar from boiling temperature 4.3 K to 300 K. The orange data points (601 in total) are given by NIST webbook [39]. The black dash line is a polynomial fit created with MSE at the order of 6 with 30 digits of each coefficient (vacant zeros at the end of a coefficient are not shown). Its corresponding equation is displayed on top of the chart. The blue line indicates the relative deviation of this polynomial fit with the given data points. It refers to the same y-axis values but without the written unit. The deviation is less than 1 % For $T > 23$ K, while the equation is clearly unprecise for $4.3\ \mathrm{K} \leq T \leq 8$ K.

Table A.2. Thermal conductivity integral data for the 150 A and 1000 A VCL provided by AMI.

	int(kdT) [W/m], Tref = 1K	
T [K]	150A VCCL	1000A VCCL
2	[redacted]	[redacted]
4	[redacted]	[redacted]
6	[redacted]	[redacted]
8	[redacted]	[redacted]
10	[redacted]	[redacted]
15	[redacted]	[redacted]
20	[redacted]	[redacted]
25	[redacted]	[redacted]
30	[redacted]	[redacted]
35	[redacted]	[redacted]
40	[redacted]	[redacted]
50	[redacted]	[redacted]
60	[redacted]	[redacted]
70	[redacted]	[redacted]
77	[redacted]	[redacted]
80	[redacted]	[redacted]
90	[redacted]	[redacted]
100	[redacted]	[redacted]
120	[redacted]	[redacted]
140	[redacted]	[redacted]
160	[redacted]	[redacted]
180	[redacted]	[redacted]
200	[redacted]	[redacted]
220	[redacted]	[redacted]
240	[redacted]	[redacted]
260	[redacted]	[redacted]
280	[redacted]	[redacted]
300	[redacted]	[redacted]

$$\boxed{q = \frac{A}{L}\int_{T1}^{T2} k(T)dT}$$

A is cross-sectional area of VCCL

A150 = [redacted]

A1000 = [redacted]

These are theoretical values provided by AMI as a courtesy. Actual values will vary from the theoretical. Please to not disclose to any third party.

B. Iterative determination of MLI radiation

Table B.1. Results of iterative calculation for MLI radiation from shell a to b.

n	method 1: T in K	method 1: ε	method 1: $\dot{q}_{\mathrm{rad}\ i(i+1)}$ in W m^{-2}	method 2: T in K	method 2: ε	method 2: $\dot{q}_{\mathrm{rad}\ i(i+1)}$ in W m^{-2}
a	300	4.34%	0.305224	300	4.34%	0.218631
1	297.723	4.32%	0.305224	298.376	4.33%	0.218631
2	295.382	4.30%	0.305224	296.719	4.31%	0.218631
3	292.973	4.28%	0.305224	295.028	4.30%	0.218631
4	290.49	4.26%	0.305224	293.302	4.29%	0.218631
5	287.929	4.24%	0.305224	291.538	4.27%	0.218631
6	285.283	4.22%	0.305224	289.736	4.26%	0.218631
7	282.547	4.20%	0.305224	287.892	4.24%	0.218631
8	279.712	4.17%	0.305224	286.005	4.22%	0.218631
9	276.771	4.15%	0.305224	284.073	4.21%	0.218631
10	273.713	4.12%	0.305224	282.092	4.19%	0.218631
11	270.528	4.09%	0.305224	280.06	4.17%	0.218631
12	267.202	4.06%	0.305224	277.974	4.16%	0.218631
13	263.719	4.03%	0.305224	275.83	4.14%	0.218631
14	260.063	4.00%	0.305224	273.625	4.12%	0.218631
15	256.209	3.96%	0.305224	271.355	4.10%	0.218631
16	252.133	3.92%	0.305224	269.014	4.08%	0.218631
17	247.801	3.88%	0.305224	266.597	4.06%	0.218632
18	243.171	3.83%	0.305223	264.099	4.04%	0.218632
19	238.192	3.78%	0.305223	261.513	4.01%	0.218632
20	232.797	3.72%	0.305222	258.83	3.99%	0.218632
21	226.898	3.66%	0.305222	256.043	3.96%	0.218632
22	220.376	3.59%	0.305222	253.141	3.93%	0.218633
23	213.068	3.52%	0.305222	250.111	3.90%	0.218633
24	204.737	3.44%	0.305221	246.942	3.87%	0.218634
25	195.02	3.37%	0.305221	243.615	3.83%	0.218636
26	183.286	3.29%	0.305220	240.112	3.80%	0.218638
27	168.17	3.16%	0.305217	236.41	3.76%	0.218641
28	145.921	2.97%	0.305271	232.482	3.72%	2.16718
b	50	1.99%		50	1.99%	

C++ script of program of method 1 for iterative determination of MLI radiation

```
/************************************************************************************

* Iteration of a radiative heat flux between two flat surfaces with 30 MLI layers in between

************************************************************************************/

#include <iostream>
#include<math.h>
using namespace std;

double T_formula[30];                  // Global variable.
double T[30];                          // Global variable.
double T_arithmetic = 0;               // Global variable.
double e[30];                          // Global variable.
double e_arithmetic;                   // Global variable.
double C_MLI[29];                      // Global variable (29 in total, one less than number of MLI layers).
double C;                              // Global variable.
double O = 5.670374419e-8;             // Stefan-Boltzmann constant Sigma in W/m^2/K^4.
double q_single[29];                   // Global variable, q in between each MLI layer.
double q_arithmetic;                   // Global variable. Arithmetic mean value of all q_single.
double q_single_max, q_single_min;
double q_delta_max_min;

void e_fct()                           // Function to calculate emissive coefficient of each layer.
{
        for (int i = 0; i < 30; i++)
        {
                if (T[i] > 173.15)              // Emissive coefficient e as function of T with Hutchinson measurement
data
                {e[i] = -0.000000000000014377252114228600 * pow(T[i], 6) + 0.000000000021664913557032800000 *
pow(T[i], 5) - 0.000000013474828048810800000000 * pow(T[i], 4) + 0.000004423845146434720000000000 * pow(T[i], 3) -
0.000807880213568900000000000000 * pow(T[i], 2) + 0.077845889331174600000000000000 * T[i] -
3.063562427245700000000000000000;}
else
{e[i] = 6.8e-4 * pow(T[i], 0.67) + 0.0105092296;   // Emissive coefficient e as function of T according to Lockheed in NASA paper.
        };
        };
};

void e_arithmetic_fct()                         // Calculate and arithmetic mean value of all emissive coefficients.
{
        e_arithmetic = 0;                       // Reset e_arithmetic.
        for (int i = 0; i < 30; i++)
        {
                e_arithmetic += e[i];
        };
        e_arithmetic = e_arithmetic / 30;
};

void PRINT_T_and_e_fct()                        // Function to print table of T and corresponding e.
{
        for (int i = 0; i < 30; i++)
        {
                cout << "T" << i << ": " << T[i] << " K   with   e[" << i << "]: " << e[i] << "\n";
        };
};

void C_fct()
{
        for (int i = 0; i < 29; i++)            // Function to adjust C with new e.
        {
                C_MLI[i] = O / ((1 / e[i]) + (1 / e[i + 1]) - 1);
        };
};

void T_for_e_const()                            //  Function for T[i] with e = constant.
{
```

```
		cout << "T[0] = " << T[0] << " K\n";
		double a = 0, b = 0;
		for (int i = 1; i < 29; i++)
		{
			a = pow(T[0], 4) * (29 - i);
			b = pow(T[29], 4) * i;
			T[i] = pow((a + b) / 29, 0.25);
			cout << "T[" << i << "] = " << T[i] << " K\n";
		};
		cout << "T[29] = " << T[29] << " K\n";
};

void T_fct()						//  Function for T[i] with e =/= constant.
{
		double a = 29, b = 0, v = 0, w = 0;
		for (int i = 1; i < 29; i++)
		{
			a -= (C / C_MLI[i-1]);
			b += C / C_MLI[i-1];
			v = pow(T[0], 4) * a;
			w = pow(T[29], 4) * b;
			T[i] = pow((v + w) / 29, 0.25);
		};
};

void T_arithmetic_fct()
{
		for (int i = 1; i < 29; i++)
		{
			T_arithmetic += T[i];
		};
		T_arithmetic = T_arithmetic / 28;

};

void q_single_fct()			// Function to calculate all new q_single.
{					// They should all be the same in a steady state. Indicates mistakes.
		for (int i = 0; i < 29; i++)
		{
			q_single[i] = C_MLI[i] * (pow(T[i], 4) - pow(T[i + 1], 4));
			cout << "q[" << i << "] = " << q_single[i] << " W/m^2\n";
		};
		cout << "\n";
};

void q_arithmetic_fct()				// Calculate arithmetic mean value of all single q.
{
		q_arithmetic = 0;			// Reset q_arithmetic.
		for (int i = 0; i < 29; i++)

		{
			q_arithmetic += q_single[i];
		};
		q_arithmetic = q_arithmetic / 29;
		cout << "Arithmetic mean value of q: q_arithmetic = " << q_arithmetic << " W/m^2\n";
};

void q_single_max_min_fct()
{
		q_single_max = 0;
		q_single_min = 100000;
		for (int i = 0; i < 28; i++)
		{
			if (q_single[i] > q_single[i + 1] && q_single[i] > q_single_max)
			{
				q_single_max = q_single[i];
			}
			else {};
			if (i == 27)
			{
				if (q_single[i + 1] > q_single_max)
				{
```

```
                        q_single_max = q_single[i + 1];
                    }
                }
                else {};
        };      cout << "q_single_max = " << q_single_max << " W/m^2\n";
                for (int i = 0; i < 28; i++)
        {
                if (q_single[i] < q_single[i + 1] && q_single[i] < q_single_min)
                {
                    q_single_min = q_single[i];
                }
                else {};
                if (i == 27)
                {
                    if (q_single[i + 1] < q_single_min)
                    {
                        q_single_min = q_single[i + 1];
                    }
                }
                else {};
        };      cout << "q_single_min = " << q_single_min << " W/m^2\n";
        q_delta_max_min = q_single_max - q_single_min;
        cout << "delta q_single_max_min = " << q_delta_max_min << " W/m^2\n";
};

void main()
{
        double q;
        double E;
        cout << "Constants: \n";
        cout << "Stefan-Boltzmann constant Sigma: " << O << " W/m^2/K^4\n\n";
        cout << "Input values: \n";
        cout << "Temperature TW1 in K on hot wall side: ";     // Initialisation wall temperatures.
        cin >> T[0];
                // Boundary condition #1.
        if (T[0] < 0)
        {
                cout << "Negative value of TW1 not allowed. Type new positive value for temperature TW1 in K on hot wall
side: ";
                cin >> T[0];
        }
        else {};
        cout << "Temperature TW2 in K on cold wall side: ";
        cin >> T[29];
                // Boundary condition #2.
        if (T[29] < 0)
        {
                cout << "Negative value of TW2 not allowed. Type new positive value for temperature TW2 in K on hot wall
side: ";        cin >> T[29];
        }
        else {};
        cout << "Type in value for the average emissive coefficient e: ";          // Initialisation mean value of E.
        cin >> E;
        if (E < 0 or E > 1)
        {
                cout << "This value for e is not allowed. Type in a value for 0 < e < 1: ";
                cin >> E;
        }
        else {};
        C = O / ((2 / E) - 1);
        cout << "\nResult without iteration: \n";
        cout << "Heat exchange coefficient C for constant emissive coefficient: " << C << " W/m^2/K^4\n";
        q = C / 29 * (pow(T[0], 4) - pow(T[29], 4));          // Calculating q.
        cout << "Radiative heat flux q from hot to cold wall according to q = C / (n+1) * (TW1^4 - TW2^4) with n = 28: " << q
<< " W/m^2\n";

        for (int i = 0; i < 30; i++)                 // Initialisation of e.
        {
                e[i] = E;
        };
```

```
C_fct();                                    // Initialisation of C.
cout << "Temperature of each MLI layer for a constant emissive coefficient e: \n";
T_fct();
PRINT_T_and_e_fct();
cout << "\nCorresponding heat flux in between each two MLI layers (must be const. for steady state and true tempera-
tures):\n";
q_single_fct();

// Iteration:
double q_it[1000];                          // Maximum iteration steps: 1000.
int k = 0;                                  // k = number of iterations.
q_it[0] = q;                                // Initialisation of q_it[0] with known value q.
double T_top[30];                           // T_top indicates the temperature of each layer iterated by starting on the
hot wall side (from hot to cold).
double T_bottom[30];                // T_bottom indicates the temperature of each layer iterated by starting on the cold wall
side (from cold to hot).
T_top[0] = T[0];                            // Initialisation of T_top & T_bottom with the given values of the hot wall
side TW1 and the cold wall side TW2.
T_top[29] = T[29];
T_bottom[0] = T[0];
T_bottom[29] = T[29];
cout << "\n\nStart of iteration: \n___________________\n" << "e is now a function of temperature: e = f(T) => e[i] =/=
e[i+1]\n";
do
{
        cout << "\nIteration step #" << k+1 << ":\n-------------------\n";
        for (int i = 1; i < 15; i++)        // Calculating temp of MLI layers from hot to cold side up to the central
foil.
        {
                double b = pow(T_top[i - 1], 4);
                T_top[i] = pow(b - (q_it[k] / C_MLI[i - 1]), 0.25);
                // cout << "T_top[" << i << "]: " << T_top[i] << "\n";
        };
        for (int i = 28; i >= 15; i--)      // Calculating temp of MLI layers from cold to hot side up to the central
foil.
        {
                double b = pow(T_bottom[i + 1], 4);
                T_bottom[i] = pow(b + (q_it[k] / C_MLI[i]), 0.25);
                // cout << "T_bottom[" << i << "]: " << T_bottom[i] << "\n";
        };

        for (int i = 1; i < 15; i++)        // Give the values from T_top to the general array T.
        {
                T[i] = T_top[i];
        };
        for (int i = 28; i >= 15; i--)      // Give the values from T_bottom to the general array T.
        {
                T[i] = T_bottom[i];
        };
        e_fct();                            // Calculate new e[30] with new T[30] with function of e.
        e_arithmetic_fct();
        C_fct();                            // Adjustment of C with new e =/= constant.
        PRINT_T_and_e_fct();
        cout << "\n";
        q_single_fct();                     // Calculate & print all q.
        cout << "Arithmetic mean value of e: e_arithmetic = " << e_arithmetic << "\n";          // Print arithmetic
mean value of emissive coefficient.
        C = O / ((2 / e_arithmetic) - 1);           // Calculate new C from hot to cold wall with new arithmetic
mean value of emissive coefficient.
        q_arithmetic_fct();
        q_it[k + 1] = q_arithmetic;
        // q_it[k + 1] = C / 29 * (pow(T[0], 4) - pow(T[29], 4)); // Calculate radiative heat flux from hot to cold wall.
This value is the iteration result and gets returned in the do while loop.
        cout << "Iteration #" << k + 1 << " returns q_it = " << q_it[k + 1] << " W/m^2\n";
        q_single_max_min_fct();
        cout << "End of iteration step #" << k + 1 << "\n\n";
        k++;                                        // Increase number of iteration step by +1 to count.
} while (::std::fabs(q_it[k] - q_it[k - 1]) > 0.00001);      // Condition to stop do while loop:
                // If iterative value of q in the current iteration step is almost the same as before, the loop ends
```

```
	cout << "________________\n\n\n\nAdjustment:\n________________\n";
	int L = 0;
						// Number of iteration steps for adjustment loop
	for (int i = 0; i < 29; i++)
	{
		if (q_arithmetic - ::std::fabs(q_single[i]) > 0.05)		// Iteration ended before. However, one single q var-
ies from the rest. Therefore, a last "adjustment" is necessary.
		{
						// To do so, every single q is being compared to the arithmetic mean value. For differ-
ences above 50 mW/m^2.
			cout << "Adjustment finds wrong temperature from last iteration step #" << k;
			cout << ". The temperatures " << "T[" << i << "] = " << T[i] << " K & T[" << i + 1 << "] = " <<
T[i + 1] << " K are wrong\n";
		}
		else {};
	};

	do
	{
		L++;
		for (int x = 0; x < 29; x++)			// Write q_arithmetic into all q_single
		{
			q_single[x] = q_arithmetic;
		};
		for (int x = 1; x < 29; x++)			// Calculate and print new T from top to bottom with q_arithme-
tic = q_single.
		{
						// Therefore, the wrong T become adjusted. Before, all T[x]-T[x+1] were a big too big
and q_single were too big.
			double b = pow(T[x - 1], 4);		// Now, all T values are "squashed" (gequetscht) into each other.
			T[x] = pow(b - (q_arithmetic / C_MLI[x - 1]), 0.25);
		};

		// Same procedure as before for T: I should calculate it from bottom and top and again "spread" the mistake.
There is still one wrong T, but more accurate now.
		cout << "\nIteration step #" << k+L << ":\n-------------------\n";
		e_fct();
		e_arithmetic_fct();
		C_fct();
		PRINT_T_and_e_fct();			// Print table of T and e
		cout << "\n";
		q_single_fct();
		q_arithmetic_fct();
		cout << "Arithmetic mean value of e: e_arithmetic = " << e_arithmetic << "\n";		// Print arithmetic
mean value of emissive coefficient.
		C = O / ((2 / e_arithmetic) - 1);		// Calculate new C from hot to cold wall with new arithmetic
mean value of emissive coefficient.
		q_it[999] = C / 29 * (pow(T[0], 4) - pow(T[29], 4));	// Calculate radiative heat flux from hot to cold wall.
This value is the iteration result and gets returned in the do while loop.
		cout << "Adjustment returns q_it = " << q_it[999] << " W/m^2\n";
		q_single_max_min_fct();
		cout << "End of iteration step #" << k + L << "\n\n";

	} while(q_single_min < 0 && q_single_max + q_single_min > 0.0001 or q_single_min > 0 && q_single_max - q_sin-
gle_min > 0.0001);
	T_arithmetic_fct();
	cout << "\n\n\n__________________________________________________________________\n\n\n";
	cout << "\nIteration finished. Number of total iteration steps: " << k+L << "\n";		// Step number k not k + 1 as in
the do while loop, because of k++ at the end of the loop.
	cout << "\nFinal Results:\nArithmetic mean value of heat flux from hot to cold wall: q_arithmetic = " << q_arithmetic
<< " W/m^2\n";
	cout << "with q_max = " << q_single_max << " W/m^2 and q_min = " << q_single_min << " W/m^2";
	cout << "\nArithmetic mean value of e: e_arithmetic = " << e_arithmetic;
	cout << "\nArithmetic mean value of all MLI layer temperatures: T_arithmetic = " << T_arithmetic << "\n\n";
	cout << "\nThe improvement of the iterative resultcompared to the result with e=const. is: " << (q - q_arithmetic) / q *
100 << " %\n\n";

	system("PAUSE");
};
```

```
Constants:
Stefan-Boltzmann constant Sigma: 5.67037e-08 W/m^2/K^4

Input values:
Temperature TW1 in K on hot wall side: 300
Temperature TW2 in K on cold wall side: 50
Type in value for the average emissive coefficient e: 0.043

Result without iteration:
Heat exchange coefficient C for constant emissive coefficient: 1.24592e-09 W/m^2/K^4
Radiative heat flux q from hot to cold wall according to q = C / (n+1) * (TW1^4 - TW2^4) with n = 28: 0.347729 W/m^2
Temperature of each MLI layer for a constant emissive coefficient e:
T0: 300 K   with   e[0]: 0.043
T1: 297.382 K   with   e[1]: 0.043
T2: 294.692 K   with   e[2]: 0.043
T3: 291.927 K   with   e[3]: 0.043
T4: 289.081 K   with   e[4]: 0.043
T5: 286.149 K   with   e[5]: 0.043
T6: 283.123 K   with   e[6]: 0.043
T7: 279.997 K   with   e[7]: 0.043
T8: 276.763 K   with   e[8]: 0.043
T9: 273.412 K   with   e[9]: 0.043
T10: 269.932 K   with   e[10]: 0.043
T11: 266.312 K   with   e[11]: 0.043
T12: 262.539 K   with   e[12]: 0.043
T13: 258.595 K   with   e[13]: 0.043
T14: 254.462 K   with   e[14]: 0.043
T15: 250.117 K   with   e[15]: 0.043
T16: 245.533 K   with   e[16]: 0.043
T17: 240.678 K   with   e[17]: 0.043
T18: 235.509 K   with   e[18]: 0.043
T19: 229.975 K   with   e[19]: 0.043
T20: 224.011 K   with   e[20]: 0.043
T21: 217.527 K   with   e[21]: 0.043
T22: 210.407 K   with   e[22]: 0.043
T23: 202.479 K   with   e[23]: 0.043
T24: 193.493 K   with   e[24]: 0.043
T25: 183.046 K   with   e[25]: 0.043
T26: 170.422 K   with   e[26]: 0.043
T27: 154.136 K   with   e[27]: 0.043
T28: 129.97 K   with   e[28]: 0.043
T29: 50 K   with   e[29]: 0.043
```

Figure B.1. Screenshot 1 of iterative C++ script of program output. The boundary conditions are 300 K as hot temperature and 50 K as cold temperature. The emissive coefficient to start the iteration is 0.043.

```
q[0] = 0.305224 W/m^2
q[1] = 0.305224 W/m^2
q[2] = 0.305224 W/m^2
q[3] = 0.305224 W/m^2
q[4] = 0.305224 W/m^2
q[5] = 0.305224 W/m^2
q[6] = 0.305224 W/m^2
q[7] = 0.305224 W/m^2
q[8] = 0.305224 W/m^2
q[9] = 0.305224 W/m^2
q[10] = 0.305224 W/m^2
q[11] = 0.305224 W/m^2
q[12] = 0.305224 W/m^2
q[13] = 0.305224 W/m^2
q[14] = 0.305224 W/m^2
q[15] = 0.305224 W/m^2
q[16] = 0.305224 W/m^2
q[17] = 0.305224 W/m^2
q[18] = 0.305223 W/m^2
q[19] = 0.305223 W/m^2
q[20] = 0.305222 W/m^2
q[21] = 0.305222 W/m^2
q[22] = 0.305222 W/m^2
q[23] = 0.305222 W/m^2
q[24] = 0.305221 W/m^2
q[25] = 0.305221 W/m^2
q[26] = 0.30522 W/m^2
q[27] = 0.305217 W/m^2
q[28] = 0.305271 W/m^2

Arithmetic mean value of q: q_arithmetic = 0.305225 W/m^2
Arithmetic mean value of e: e_arithmetic = 0.0382867
Adjustment returns q_it = 0.30887 W/m^2
q_single_max = 0.305271 W/m^2
q_single_min = 0.305217 W/m^2
delta q_single_max_min = 5.36273e-05 W/m^2
End of iteration step #6

________________________________________________________________________________

Iteration finished. Number of total iteration steps: 6

Final Results:
Arithmetic mean value of heat flux from hot to cold wall: q_arithmetic = 0.305225 W/m^2
with q_max = 0.305271 W/m^2 and q_min = 0.305217 W/m^2
Arithmetic mean value of e: e_arithmetic = 0.0382867
Arithmetic mean value of all MLI layer temperatures: T_arithmetic = 248.279


The improvement of the iterative resultcompared to the result with e=const. is: 12.2234 %
```

Figure B.2. Screenshot 2 of iterative C++ script of program output. The boundary conditions are 300 K as hot temperature and 50 K as cold temperature. The emissive coefficient to start the iteration is 0.043.

C. Technical drawings

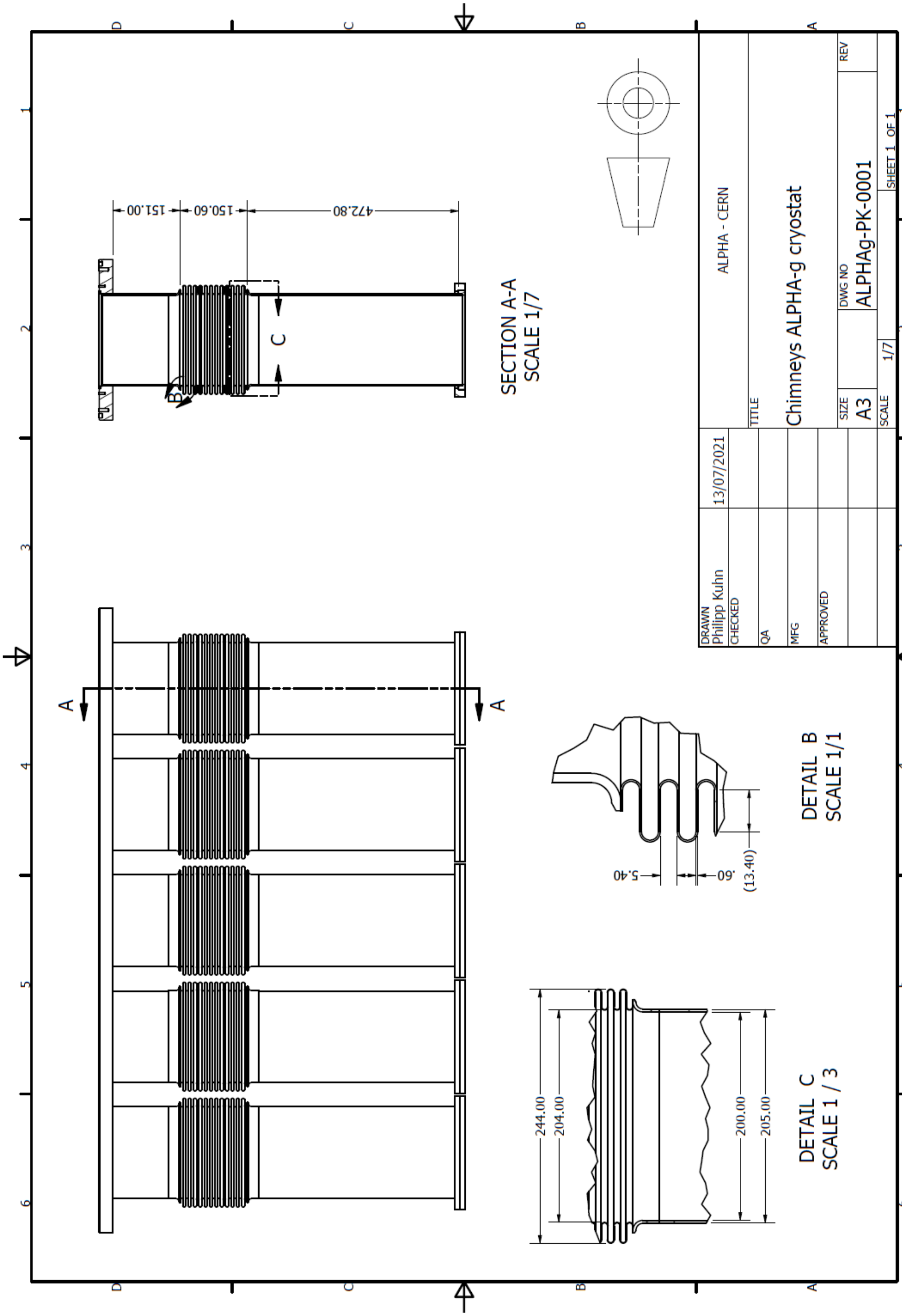

Figure C.1. Technical drawing of a chimney in half section view with detail on the flexible bellow. Only the dimensions that are relevant for the calculation in this document are shown. The scale refers to the original sheet size of DIN-A3.

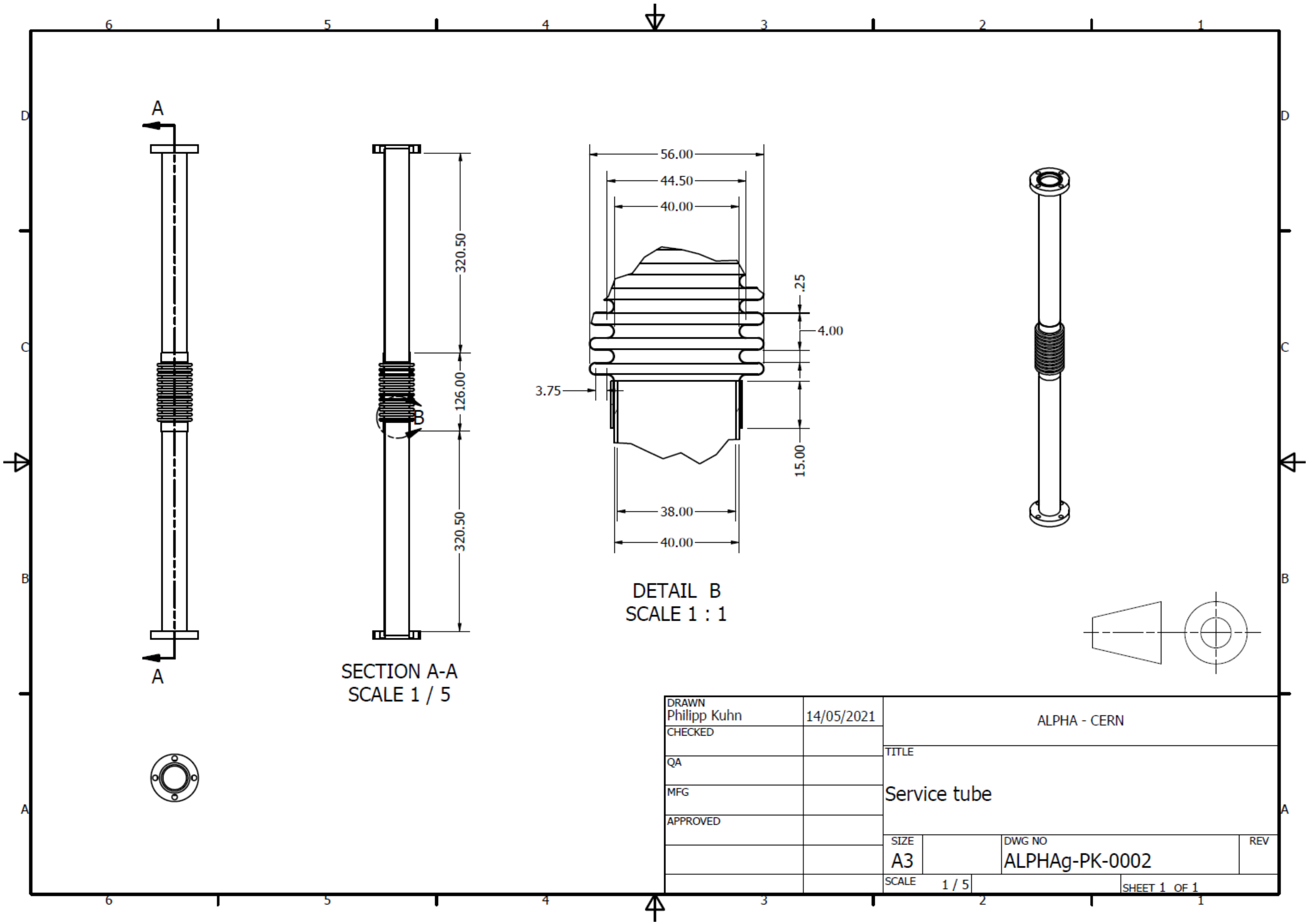

Figure C.2. Technical drawing of a service tube in half section view with detail on the flexible bellow. Only the dimensions that are relevant for the calculation in this document are shown. The scale refers to the original sheet size of DIN-A3.

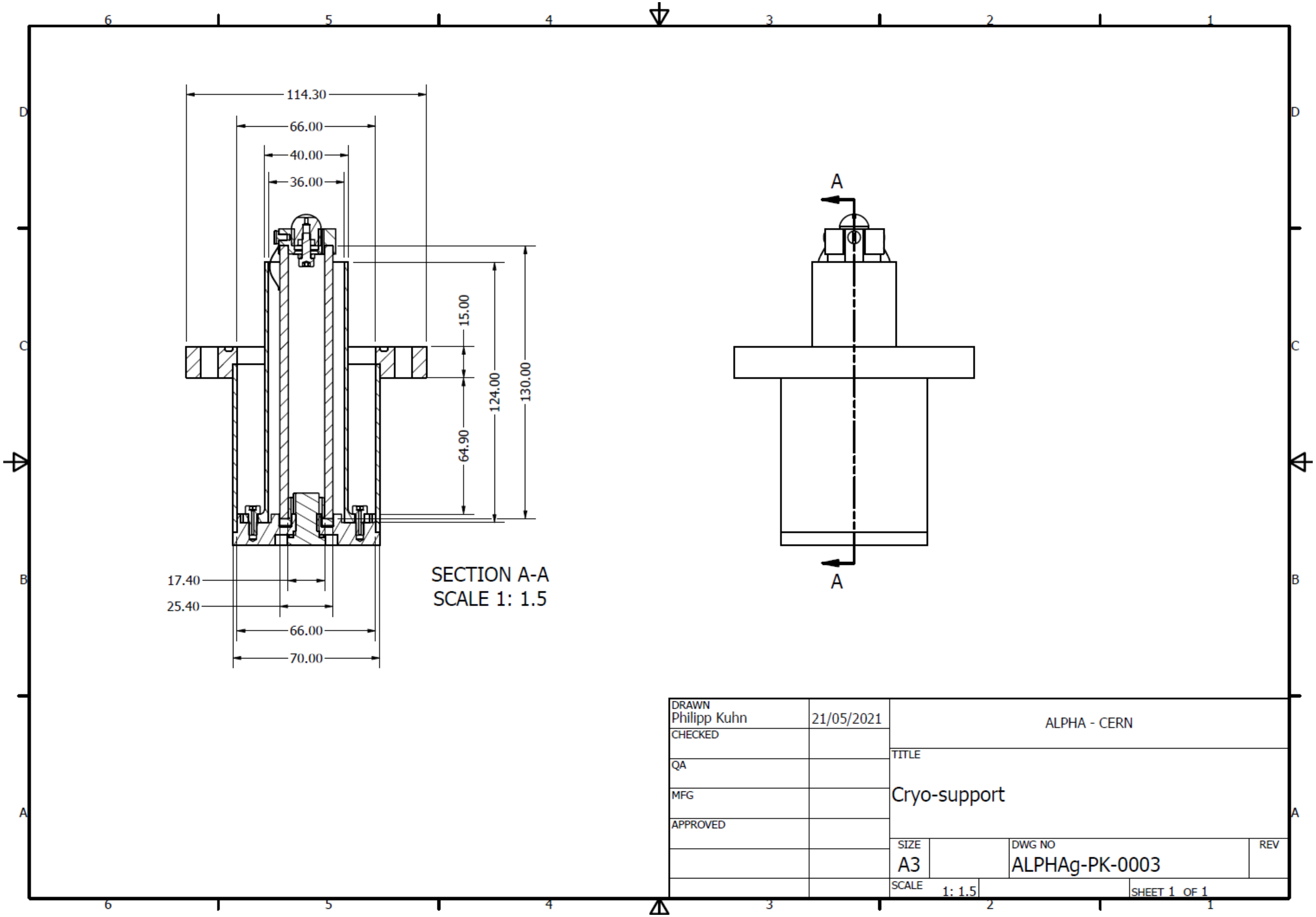

Figure C.3. Technical drawing of a cryo support for the He-box in half section view. Only the dimensions that are relevant for the calculation in this document are shown. The scale refers to the original sheet size of DIN-A3.

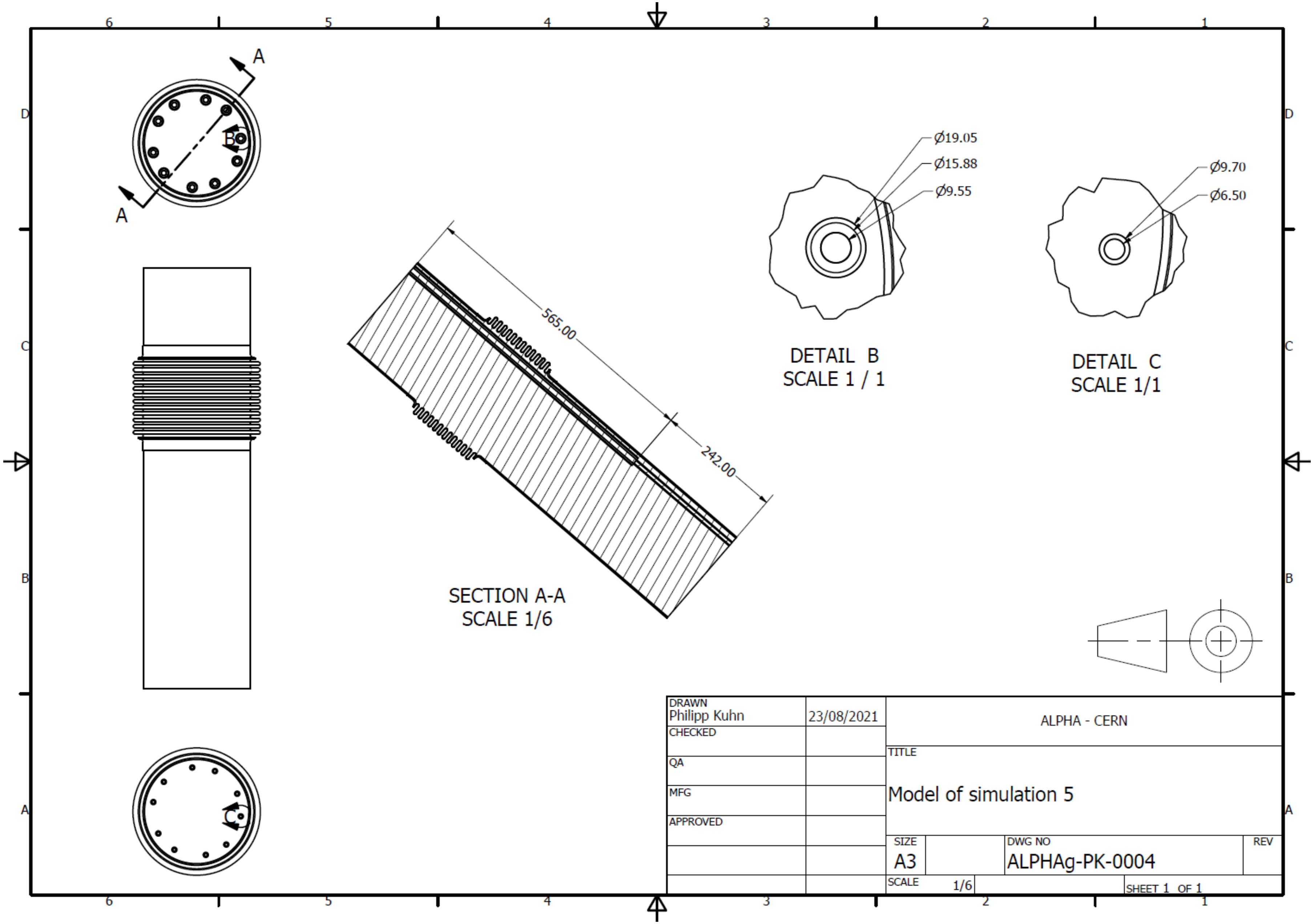

Figure C.4. Technical drawing of the CAD model used for the ANSYS simulation in chapter 4.6.4. Only dimensions of the VCL, HTS and their G10 tubes are shown relevant for the simulation. Baffles are not included in the simulation. The scale refers to the original sheet size of DIN-A3.

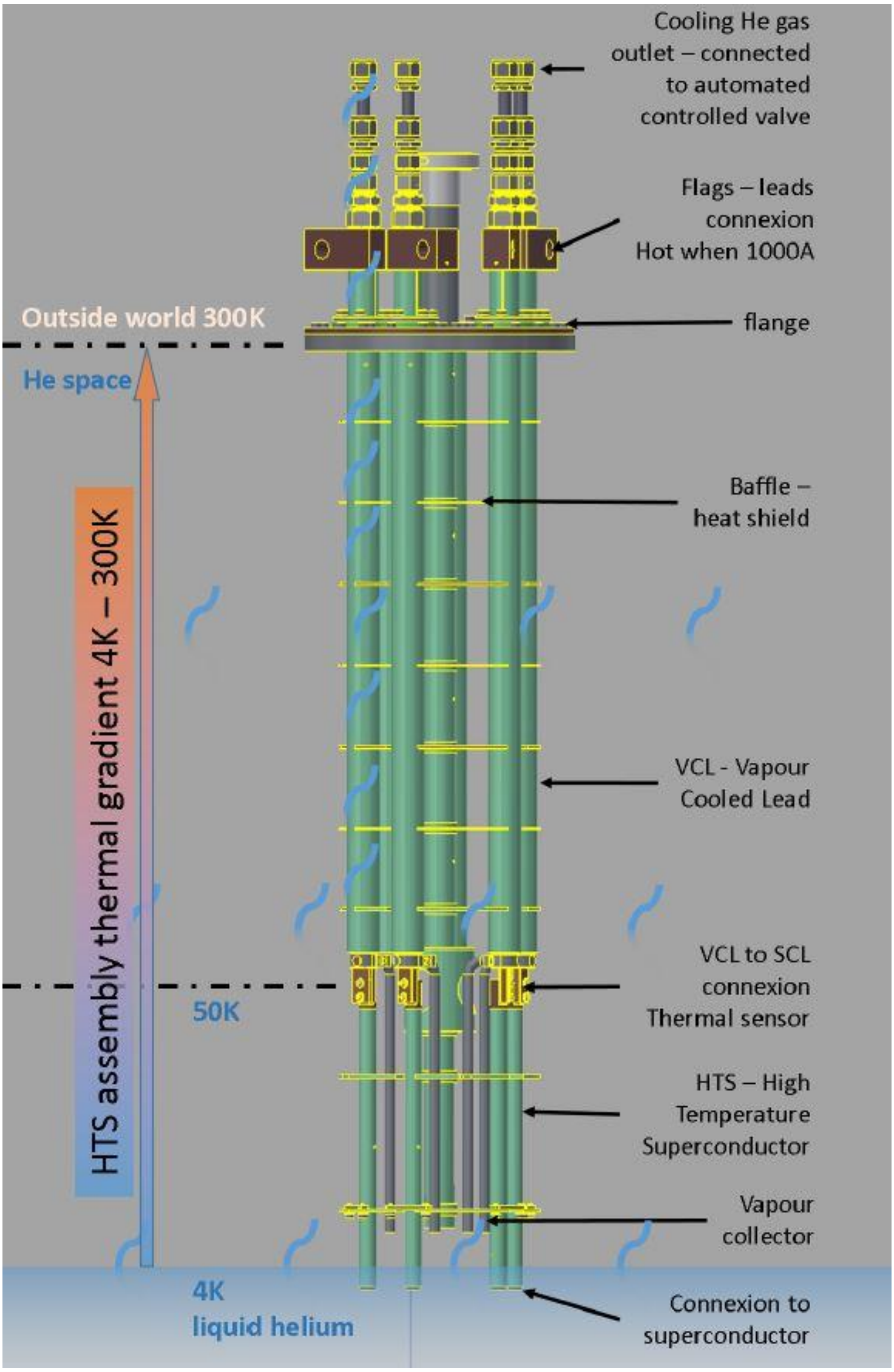

Figure C.5. Schematic illustration of the VCL surrounded by GHe. The HTS is bathing in LHe. A description is shown of thermally relevant components [Pierre Grandemange, ALPHA, CERN].